

Isadora Limas Coimbra

**INVESTIGATION OF A COASTAL WIND FARM AT
NORTHEAST BRAZIL USING THE WRF MODEL**

Dissertação submetida ao Programa de
Pós-Graduação em Engenharia Mecânica
da Universidade Federal de Santa
Catarina para a obtenção do Grau de
Mestre em Engenharia Mecânica.

Orientador: Prof. Dr. Júlio César Passos

Coorientador: Prof. Dr. Reinaldo Haas

Florianópolis
2018

Ficha de identificação da obra elaborada pelo autor,
através do Programa de Geração Automática da Biblioteca Universitária
da UFSC.

Coimbra, Isadora Limas
Investigation of a coastal wind farm at
Northeast Brazil using the WRF model / Isadora
Limas Coimbra ; orientador, Júlio César Passos,
coorientador, Reinaldo Haas, 2018.
142 p.

Dissertação (mestrado) - Universidade Federal de
Santa Catarina, Centro Tecnológico, Programa de Pós
Graduação em Engenharia Mecânica, Florianópolis, 2018.

Inclui referências.


1. Engenharia Mecânica. 2. Energia eólica. 3.
Simulação do vento. 4. Previsão de geração eólica. 5.
Modelo WRF. I. Passos, Júlio César. II. Haas,
Reinaldo. III. Universidade Federal de Santa
Catarina. Programa de Pós-Graduação em Engenharia
Mecânica. IV. Título.

Isadora Limas Coimbra

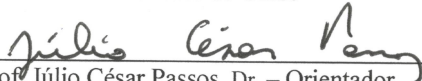
**INVESTIGATION OF A COASTAL WIND FARM AT
NORTHEAST BRAZIL USING THE WRF MODEL**

Esta Dissertação foi julgada adequada para obtenção do Título de “Mestre em Engenharia Mecânica”, e aprovada em sua forma final pelo Programa de Pós-Graduação em Engenharia Mecânica.


Florianópolis, 13 de Agosto de 2018.



Prof. Jonny Carlos da Silva, Dr. Eng.
Coordenador do Curso

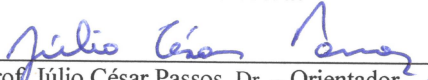


Prof. Júlio César Passos, Dr. – Orientador
Universidade Federal de Santa Catarina

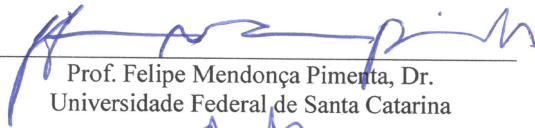


Prof. Reinaldo Haas, Dr. – Coorientador
Universidade Federal de Santa Catarina

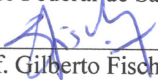
Banca Examinadora:



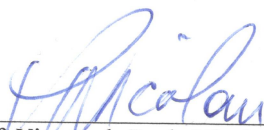
Prof. Júlio César Passos, Dr. – Orientador
Universidade Federal de Santa Catarina



Prof. Felipe Mendonça Pimenta, Dr.
Universidade Federal de Santa Catarina



Prof. Gilberto Fisch, Dr.
Instituto de Aeronáutica e Espaço

A handwritten signature in blue ink, appearing to read 'P. Nicolau', is positioned above a horizontal line.

Prof. Vicente de Paulo Nicolau, Dr.
Universidade Federal de Santa Catarina

To my family.

AGRADECIMENTOS

À minha mãe, por sempre acreditar em mim, apoiar minhas decisões e me ensinar a correr atrás dos meus objetivos dando o melhor de mim. Ao meu pai (*in memoriam*), que mesmo não mais presente, me mostrou que a educação é a base de tudo e que a partir dela tudo pode se transformar. Ao meu irmão, que mesmo sem saber, me faz ser uma pessoa melhor. Portanto família, muito obrigada pelo apoio incondicional.

Ao Professor Júlio César Passos, por sua orientação e por acreditar, a quatro anos atrás, que eu poderia me tornar uma pesquisadora. Ao Professor Reinaldo Haas, que me tornou ainda mais apaixonada pela ciência. Ao Pedro Alvim e Yoshiaki Sakagami que, desde o início, me ensinaram sobre a arte da eólica e seus ensinamentos foram fundamentais para a elaboração deste trabalho. A esses quatro mentores, muito obrigada, esta dissertação e minha paixão pelo vento não seria possível sem vocês.

Aos meus amigos do LEPTEN/Boiling que colocaram mais cores aos meus dias e fizeram do Laboratório minha casa. Muito obrigada pelos momentos compartilhados e por se tornarem minha família acadêmica.

Aos meus amigos da Faculdade, de Laguna, de Floripa, da vida, obrigada por estarem presentes. Em especial à Mônica Nassar Machuca, Rafael Passarella, Patrícia Nunes Medeiros, Camilla Borges Rampinelli, André Loch Gesing e Felipe Sempertegui Maldonado Pires.

À ENGIE Brasil e Atlantic Energias Renováveis S.A., por acreditarem na parceria com a Universidade e financiarem dois projetos de Pesquisa e Desenvolvimento na área eólica dos quais participei. Ao POSMEC, CAPES e UFSC, pelo apoio financeiro e suporte acadêmico.

Ainda, muito obrigada a todos que de alguma forma fizeram parte e/ou contribuíram para este trabalho.

ACKNOWLEDGEMENTS

To my mother, for always believing in me, supporting my decisions and teaching me to go after my goals giving the best of me. To my father (*in memoriam*), who even no longer present, showed me that education is the basis of everything and that from it everything can be transformed. To my brother, who even without knowing it, makes me a better person. So, family, thank you very much for the unconditional support.

To Professor Júlio César Passos, for his guidance and for believing, four years ago, that I could become a researcher. To Professor Reinaldo Haas, who made me even more passionate about science. To Pedro Alvim and Yoshiaki Sakagami who, from the beginning, taught me about the art of wind power and their teachings were fundamental to this work. To these four mentors, thank you very much, this dissertation and my passion for the wind would not be possible without you.

To my friends from LEPTEN/Boiling who added more colors to my days and made the Lab my home. Thank you for the time we shared and for becoming my academic family.

To my friends from the University, from Laguna, from Floripa, from life, thank you for being present. In particular, Mônica Nassar Machuca, Rafael Passarella, Patrícia Nunes Medeiros, Camilla Borges Rampinelli, André Loch Gesing and Felipe Sempertegui Maldonado Pires.

To ENGIE Brasil and Atlantic Energias Renováveis S.A., for believing in the partnership with the University and financing two Research and Development projects in the wind area in which I participated. To POSMEC, CAPES and UFSC, for financial and academic support.

Also, thank you very much to all who have somehow participated and/or contributed to this work.

*“Run, rabbit run
Dig that hole, forget the sun
And when at last the work is done
Don't sit down, it's time to dig another one”.*
(Breathe – Pink Floyd)

RESUMO

Dentre as fontes de energias renováveis, a eólica possui o maior crescimento no mundo, tornando-se uma importante fonte de energia mundial. Devido à sua natureza intermitente, os operadores do sistema elétrico normalmente utilizam modelos numéricos de previsão do tempo, e suas simulações do vento, para garantir o suprimento de energia e balanceamento de carga no sistema interligado nacional. Com o objetivo de contribuir para o crescimento da energia eólica no Brasil, este estudo avaliou e otimizou simulações do vento obtidas pelo modelo WRF na Usina Eólica de Pedra do Sal, assim como investigou previsões de energia eólica obtidas pela combinação do WRF e de redes neurais artificiais. A usina eólica de 18 MW está localizada na costa do Nordeste brasileiro, o que, devido a diferentes características na temperatura, rugosidade e superfície da terra/mar, introduz desafios adicionais na simulação do vento por modelos numéricos. Desta forma, o estudo englobou três resultados principais. Primeiro, uma análise de sensibilidade do modelo de camada limite planetária foi realizada nas simulações do WRF com um domínio, de 15 km de resolução de grade, para o mês de setembro de 2013. Os menores erros na simulação do vento foram obtidos utilizando a parametrização MYNN2 (RMSE de 2,12 m/s e Bias de -1,37 m/s). Segundo, os resultados do WRF foram interpolados em locais *onshore* e *offshore*, procedimento nomeado de abordagem de interpolação. Devido ao vento local ser influenciado pela proximidade do mar, os dados interpolados na localização *offshore* OFF-2 exibiram a melhor performance, resultando em RMSE de 1,69 m/s e Bias de -0,10 m/s. Isso representa uma redução de 20,2% do RMSE e 92,7% do Bias, quando comparado aos resultados obtidos no local usual de interpolação, a posição da torre anemométrica (ON-T). Terceiro, a abordagem de interpolação foi investigada na previsão de geração eólica com redes neurais, de setembro a dezembro de 2013. Dados das posições ON-T e OFF-2 serviram de entrada para duas redes neurais *feedforward* de três camadas. Para uma mesma arquitetura de 80 neurônios, as previsões de geração eólica de NN-OFF-2 resultaram em menores valores de RMSE e Bias, 7,7% e 7,4%, respectivamente, que as previsões de NN-ON-T. Em conclusão, a interpolação *offshore* dos resultados do WRF provou ser uma abordagem viável a ser implementada em previsões de vento e de geração eólica na Usina Eólica de Pedra do Sal, pois utiliza menor tempo de processamento, resulta em maior performance e menores valores de erros de previsão quando comparada a outras simulações.

Palavras-chave: áreas costeiras, simulação do vento, previsão de geração eólica, modelo WRF, redes neurais artificiais.

RESUMO EXPANDIDO

Introdução

As fontes renováveis de energia vêm aumentando suas contribuições para a matriz energética mundial nos últimos anos. Dentre essas fontes, a energia eólica apresentou o crescimento mais rápido do mundo (Figura 1) e se tornou uma importante fonte de energia. Ao final de 2017, o Brasil estava na 8ª posição mundial entre os países com maior capacidade eólica instalada, com 12.76 GW (GWEC, 2018).

No entanto, como a velocidade do vento tem uma alta variabilidade temporal, a energia eólica é intermitente e sua produção aumenta ou diminui de acordo com a velocidade do vento, o que pode gerar flutuações inesperadas de energia na rede. Portanto, os operadores do sistema elétrico utilizam previsões numéricas do tempo, e suas simulações de vento, a fim de garantir um equilíbrio entre a oferta e a demanda de energia (ROSGAARD, 2015), o que as tornam fundamentais para uma melhor exploração dessa energia.

Modelos numéricos de previsão do tempo são ferramentas computacionais que simulam o vento, seu regime local e seu comportamento futuro. No entanto, por estes apresentarem diversas configurações físicas, ajustar um modelo atmosférico de acordo com as características da região de estudo é uma tarefa desafiadora (CARVALHO et al., 2012).

Objetivos

O objetivo deste trabalho é melhorar as simulações atmosféricas do modelo Weather Research and Forecasting (WRF), avaliando suas parametrizações físicas e investigando as interpolações *onshore* e *offshore* de seus resultados sobre a Usina Eólica de Pedra do Sal (PSWF). Além disso, uma avaliação do desempenho desta abordagem de interpolação será realizada para a previsão de energia eólica, através da aplicação de redes neurais artificiais (ANN).

Para atingir o objetivo principal deste trabalho, alguns objetivos específicos foram estabelecidos: (i) verificar o modelo de camada limite planetária do WRF mais adequado para simulações de vento na PSWF durante os meses secos; (ii) avaliar a diferença que as interpolações espaciais podem resultar nas simulações atmosféricas do WRF na PSWF; (iii) investigar uma abordagem alternativa para melhorar a simulação do vento em uma área costeira; (iv) avaliar as simulações de vento do WRF nas condições atmosféricas da costa do Nordeste brasileiro e (v) investigar o uso combinado do modelo WRF e ANN para a previsão de energia eólica na PSWF.

Metodologia

Este estudo de caso avaliou a área da usina eólica de Pedra do Sal, que apresenta 18 MW de potência instalada, 20 aerogeradores (44 m de diâmetro de rotor e 55 m de altura de rotor) e uma torre anemométrica de 100 m. Localizada no Nordeste do Brasil (Figura 17), em um terreno plano a cerca de 400 m de distância do Oceano Atlântico, PSWF apresenta um regime de ventos influenciado pelos ventos alísios e pela proximidade do mar.

Áreas costeiras introduzem dificuldades adicionais aos modelos de previsão do tempo na simulação das características do vento, devido a particularidades na circulação atmosférica local. Com o objetivo de melhorar a simulação do vento costeiro na PSWF, obtida pelo modelo WRF, três análises foram conduzidas neste estudo. Primeiro, através de uma análise de sensibilidade, foi determinado o modelo de camada limite planetária que melhor simulou as características do vento no local de estudo. Segundo, foi testada uma abordagem de interpolação horizontal dos dados de saída do modelo WRF, com o objetivo de reduzir os erros de simulação do vento. Terceiro, esta abordagem de interpolação foi analisada também na previsão de produção de energia eólica, usando ANN. Dessa forma, três bases de dados foram utilizadas: dados experimentais anemométricos e da produção de energia eólica, dados de simulação atmosférica do modelo WRF e dados de previsão da geração eólica da ANN.

A base de dados medidos englobou medições da velocidade do vento, por um anemômetro de copo instalado a 98 m na torre anemométrica, dados de direção do vento, por uma *wind vane* a 96 m, dados de temperatura do ar, por um termohigrômetro a 98 m, e dados de produção de energia eólica de cada turbina, obtidos através do software SCADA.

A base de dados de simulação atmosférica foi obtida através da utilização do modelo de mesoescala WRF (v. 3.6.1). As simulações englobaram a área da PSWF com dois domínios aninhados (Figura 20), com 15 km e 5 km de espaçamento de grade. Com o objetivo de permitir comparações entre os dados medidos e simulados, os resultados do WRF foram interpolados verticalmente na mesma altura das medições e horizontalmente em diferentes pontos (*onshore* e *offshore*) da grade de simulação. Tal abordagem, nomeada abordagem de interpolação, foi aplicada com o objetivo de analisar as influências que a variação no local de interpolação pode causar nos dados simulados.

Os dados do WRF, obtidos com as simulações de um domínio de 15 km de resolução horizontal, foram linearmente interpolados em diferentes locais ao longo da direção norte-sul, cruzando a linha da costa e da usina eólica (Figura 21 e Tabela 9). O estudo analisou quatro pontos

offshore (OFF-1, OFF-2, OFF-3 e OFF-4), a posição da torre anemométrica (ON-T) e mais dois pontos *onshore* (ON-1 e ON-2). As simulações cobriram os meses de setembro a dezembro de 2013, com horizonte de previsão de 5 dias (120 horas) em intervalos de 10 min. Posteriormente, as simulações foram reduzidas em médias de 30 minutos, para atender as exigências requeridas pelo Operador Nacional do Sistema (ONS, 2017).

Por fim, a base de dados de previsão da geração eólica foi obtida através da aplicação de ANN, utilizando como dados de entrada as previsões atmosféricas do modelo WRF (Figura 22). Uma rede neural (NN) *feedforward* de 3 camadas foi aplicada neste trabalho, com uma camada de entrada, uma camada escondida e uma camada de saída. Nove neurônios foram utilizados na camada de entrada, um neurônio na camada de saída e diferentes números de neurônios foram testados na camada escondida, através de uma análise de sensibilidade. No total, foram realizados 25 ciclos de trinta dias de treinamento e cinco dias de previsão, em intervalos de 30 minutos (Tabela 10).

Resultados e Discussão

Para a análise de sensibilidade, seis simulações (S-1 a S-6) foram realizadas usando diferentes configurações físicas para a camada limite planetária, camada superficial e superfície da terra no modelo WRF (Tabela 11). Esses resultados foram obtidos com as simulações de um domínio no WRF para o mês de setembro de 2013.

Durante o período analisado, todas as configurações testadas subestimaram a velocidade do vento medida a 98 m e exibiram um atraso na representação da velocidade mínima do dia, de cerca de 2 horas. No entanto, S-4 (MYNN2-MYNN-Noah) foi a configuração que apresentou os menores erros de simulação da velocidade (RMSE de 2,12 m/s e Bias de -1,37 m/s) e da direção do vento (RMSE de 12,21° e Bias de -3,04°) na PSWF, além de mostrar a distribuição de Weibull mais próxima da função medida. Assim, as parametrizações do WRF aplicadas nas análises seguintes foram: MYNN2 na camada limite planetária, MYNN na camada superficial e Unificado Noah na superfície terrestre.

Para a análise da abordagem de interpolação horizontal dos dados de saída do modelo WRF, foram utilizadas as simulações com um e dois domínios. A análise de um domínio avaliou sete locais de interpolação (*onshore* e *offshore*); enquanto os dados do domínio aninhado foram interpolados apenas na posição da torre anemométrica (ON-T-2D) e utilizados para investigar o desempenho da abordagem de interpolação.

Quanto mais *onshore* a localização do ponto de interpolação, maior foi a subestimação e o atraso entre as velocidades do vento observadas e

simuladas pelo WRF. Devido ao vento local ser influenciado pela proximidade do mar, as interpolações *offshore* apresentaram melhores resultados que as interpolações *onshore*. Os dados interpolados em OFF-2 obtiveram os menores erros de simulação da velocidade do vento (RMSE de 1,69 m/s e Bias de -0,1 m/s). Isso representa uma redução de 20,2% do RMSE e 92,7% do Bias quando comparado aos resultados obtidos no local usual de interpolação, a posição da torre anemométrica.

Os dados obtidos na simulação com domínio aninhado, interpolados na posição da torre, mostraram resultados de velocidade do vento um pouco mais precisos do que os obtidos na simulação ON-T (redução de 7,7% do RMSE e 13,3% do Bias). No entanto, esses não foram melhores do que os obtidos com a simulação de domínio único interpolada *offshore* (OFF-2).

Para a previsão da produção de energia eólica usando ANN, foram utilizados dados das simulações ON-T e OFF-2 como entrada para duas redes neurais *feedforward* de três camadas. Primeiramente, uma análise de sensibilidade das previsões em relação à quantidade de neurônios na camada oculta foi realizada. Esta mostrou que, para ambos os dados de entrada, as NN com 80 neurônios exibiram os melhores resultados.

Para uma mesma arquitetura de 80 neurônios, NN-OFF-2 apresentou menores valores de RMSE e Bias que as previsões de NN-ON-T, 7,7% e 7,4%, respectivamente. Ainda, observou-se que as previsões feitas a partir dos dados interpolados *offshore* apresentaram menores erros sistemáticos (28,6% menores em média para todos os testes). Concluiu-se também que com o aumento do número de neurônios, maior a capacidade da rede em prever flutuações na geração de energia eólica.

Considerações Finais

As regiões costeiras têm características específicas que são importantes para uma boa previsão atmosférica e, ao mesmo tempo, são difíceis de incorporar em um modelo de previsão. Para fornecer previsões de vento, os modelos numéricos dividem um domínio especificado com células de grade, onde dentro de cada uma dessas células, os cálculos são feitos usando as propriedades médias. Portanto, em uma região costeira onde parte da célula de grade é água e parte é terra, os parâmetros médios calculados não são adequados para uma representação precisa dos recursos costeiros.

Com a atual penetração da energia eólica na matriz energética brasileira, bem como com a perspectiva de crescimento dessa energia, é evidente a importância do desenvolvimento da previsão da velocidade do vento e da energia eólica. Portanto, simulações atmosféricas do modelo

WRF foram avaliadas neste estudo, onde vários testes foram conduzidos com o objetivo de aumentar o desempenho de suas simulações e, assim, reduzir os erros de previsão do vento.

De acordo com os resultados apresentados, a interpolação *offshore*, das simulações atmosféricas obtidas pelo modelo WRF, provou ser uma abordagem viável a ser implementada nas previsões da velocidade do vento e da produção de energia na usina eólica de Pedra do Sal. Esta abordagem utiliza menos tempo computacional, alcança maior desempenho e menores erros de previsão quando comparada à simulações com domínios aninhados.

Palavras-chave: áreas costeiras, simulação do vento, previsão de geração eólica, modelo WRF, redes neurais artificiais.

ABSTRACT

Among the renewable energy sources, wind energy has the fastest growth in the world and became an important source of energy worldwide. Due to its intermittent nature, energy system operators normally rely on numerical weather predictions, and their wind simulations, in order to ensure energy supply and load balancing in the system. Aiming to contribute to the wind energy growth in Brazil, this study evaluated and optimized wind simulations obtained by the WRF model in Pedra do Sal wind farm, as well as assessed wind power predictions obtained by the combination of WRF and artificial neural networks. The 18 MW wind farm is located on the northeast coast of Brazil, which, due to different thermal, roughness and surface features of land/sea, introduces additional challenges in the wind simulation by numerical models. The study covered three main results. First, a sensitivity analysis of the planetary boundary layer scheme was performed in one-domain WRF simulations, with 15 km of grid resolution, for September 2013. The lowest wind simulation errors were obtained using MYNN2 parameterization (RMSE of 2.12 m/s and Bias of -1.37 m/s). Second, the WRF results were interpolated in onshore and offshore locations, named as interpolation approach. Since the local wind is influenced by the proximity to the sea, the data interpolated at the offshore location OFF-2 displayed the best performance, showing a RMSE of 1.69 m/s and Bias of -0.10 m/s. This represents a reduction of 20.2% of the RMSE and 92.7% of the Bias when compared to results obtained at the usual interpolation location, the met mast position (ON-T). Third, the interpolation approach was investigated on the wind power prediction with neural networks, from September to December of 2013. ON-T and OFF-2 data were employed as input of two three-layers feedforward networks. For the same 80-neurons architecture, the wind power predictions of NN-OFF-2 showed lower RMSE and Bias, 7.7% and 7.4% respectively, than the NN-ON-T forecasts. In conclusion, the offshore interpolation of the WRF results proved to be a feasible approach to be implemented in wind speed and power predictions at the coastal Pedra do Sal wind farm, since it uses less computational time, achieves higher performance and lower prediction errors when compared to other simulations.

Keywords: coastal areas, wind simulation, wind power prediction, WRF model, artificial neural networks

LIST OF FIGURES

Figure 1 – Renewable energy generation from 2007 to 2015.	35
Figure 2 – Wind energy forecast from 2017 to 2021.	36
Figure 3 – Space and time scales of atmospheric systems.	41
Figure 4 – The troposphere structure.	42
Figure 5 – Idealized ABL structure over land.	43
Figure 6 – Wind speed profile under different static stabilities (where VBL is the boundary layer mean wind speed).	48
Figure 7 – Global atmospheric motions (arrows indicate the wind direction; closed circulations, the vertical flow of the air).	51
Figure 8 – Sea breeze during the day.	52
Figure 9 – Land breeze during the night.	53
Figure 10 – Control volume at the wind turbine rotor.	55
Figure 11 – Vertical coordinate η	58
Figure 12 – WRF-ARW horizontal grid Arakawa-C.	60
Figure 13 – Interactions between parametrizations.	64
Figure 14 – Model of a neuron.	67
Figure 15 – Single-layer feedforward network (a), multilayer feedforward network (b) and recurrent network (c).	68
Figure 16 – Schematic representation of nearest grid point and interpolated wind speeds near the coast.	79
Figure 17 – Location and terrain elevation of PSWF.	86
Figure 18 – Photo of PSWF.	86
Figure 19 – Pedra do Sal wind rose.	87
Figure 20 – PSWF anemometric tower.	88
Figure 21 – Simulation domains.	90
Figure 22 - Interpolation points (circles) and distances.	91
Figure 23 – Wind power prediction flowchart.	94
Figure 24 – Wind speed time series at 98 m for observed and simulated data with different boundary layer schemes.	100
Figure 25 – Wind speed diurnal cycle at 98 m for observed and simulated data with different boundary layer schemes.	101
Figure 26 – Weibull probability density function for observed and simulated data with different boundary layer schemes.	102
Figure 27 – Wind direction time series for observed and simulated data with different boundary layer schemes.	103
Figure 28 – Wind speed diurnal cycle at 98 m for WRF simulation (ON-T), observed data and RMSE.	105
Figure 29 – Wind speed diurnal cycle at 98 m for the observed data and WRF results in different interpolation points.	107
Figure 30 – Diurnal wind speed cycle at 98 m for observed data and WRF results in offshore interpolation with one domain (OFF-2) and onshore interpolation with a nested domain (ON-T-2D).	109

Figure 31 - Weibull probability density function for one domain simulations (ON-T and OFF-2) and for nested domain simulation (ON-T-2D)..... 110

Figure 32 – Diurnal temperature cycle for observed data and WRF results in offshore interpolation with one domain (OFF-2) and onshore interpolation with one domain (ON-T) and a nested domain (ON-T-2D). 111

Figure 33 – Wind direction time series for observed, nested and one domain simulations..... 112

Figure 34 – Wind roses of (a) observed data, (b) WRF interpolation OFF-2 data, (c) ON-T data and (d) ON-T-2D data. 113

Figure 35 – RMSE of wind power predictions obtained with ANN with different neurons numbers..... 119

Figure 36 - Bias of wind power predictions obtained with ANN with different neurons numbers..... 119

Figure 37 - Person’s coefficient of wind power predictions obtained with ANN with different neurons numbers 119

Figure 38 – Correlation between predicted and measured wind power for NN simulations with (a) ON-T data and 1 hidden neuron, (b) OFF-2 data and 1 hidden neuron (c) ON-T data and 13 hidden neurons, (d) OFF-2 data and 20 hidden neurons (e) ON-T data and 20 hidden neurons and (f) OFF-2 data and 80 hidden neurons. 120

Figure 39 - Wind power time series for measured and simulation data with one, twenty and eighty neurons in the hidden layer using OFF-2 WRF results. 121

Figure 40 - Wind power time series for measured and simulation data with one, twenty and eighty neurons in the hidden layer using ON-T WRF results. 121

Figure 41 – Wind power diurnal cycle for measured and predicted data with 1 neuron..... 122

Figure 42 – Wind power diurnal cycle for measured and predicted data with 10 neurons. 122

Figure 43 - Wind power diurnal cycle for measured and predicted data with 80 neurons. 123

LIST OF TABLES

Table 1 – Parameterizations of the WRF-ARW model v. 3.6.1.....	61
Table 2 - Closure type of some planetary boundary layer schemes of the WRF model.	65
Table 3 – Characteristics and annual mean errors of the wind speed prediction of ten surface weather stations located in Greece.	71
Table 4 – WRF wind speed prediction and improved WRF output by Kalman filter for the Lingyang wind farm.	72
Table 5 – Main WRF parameterizations used by Carvalho et al. (2014b).	74
Table 6 – Main WRF parameterizations used by Sile et al. (2014).	78
Table 7 – Summary of main parameterizations applied in studies with WRF simulations.	80
Table 8 – Information of the equipment installed in PSWF met mast.	88
Table 9 – Geographical coordinates of the interpolation locations.	91
Table 10 – Wind power forecasting cycles.	95
Table 11 – Boundary layer physical parameterizations of the simulations.	99
Table 12 – Statistical metrics for the wind speed simulations (RMSE and Bias) and predicted average wind velocities (Vel.)	100
Table 13 – Weibull parameters and most probable wind speed for simulated and observed Weibull PDFs.	102
Table 14 - Statistical metrics for the wind direction simulations.	103
Table 15 – Wind speed statistical metrics for the onshore and offshore interpolations.	107
Table 16 – Wind speed statistical metrics for one domain simulations (ON-T and OFF-2) and for the nested domain simulation (ON-T-2D).	109
Table 17 – Weibull parameters and most probable wind speed for simulated and observed Weibull PDFs.	110
Table 18 - Wind direction statistical metrics for one domain simulations (ON-T and OFF-2) and for the nested domain simulation (ON-T-2D).	112
Table 19 - Statistical metrics of wind power prediction with onshore and offshore interpolations.	117

ACRONYMS AND ABBREVIATIONS

a.g.l.	Above ground level
a.s.l.	Above sea level
ABL	Atmospheric boundary layer
ACM2	Asymmetric convective model
ANEEL	Agência Nacional de Energia Elétrica
ANN	Artificial neural network
ARW	Advanced Research WRF
AVHRR	Advanced Very High-Resolution Radiometer
BMJ	Betts-Miller-Janjic
Boulac	Bougeault–Lacarrère
BWF	Beberibe wind farm
CCEE	Câmara de Comercialização de Energia Elétrica
CI	Capping inversion
COAMPS	Coupled Ocean Atmosphere Mesoscale Prediction System
COP21	21st Conference of the Parties
CU	Cumulus
ECMWF	European Centre for Medium-Range Weather Forecasts
EIA	Energy Information Administration
EPE	Empresa de Pesquisa Energética
ERA-Interim	ECMWF Re-Analysis Interim
EZ	Entrainment zone
FDDA	Four-Dimensional Data Assimilation
FLG	Fu-Liou-Gu
G3	Grell-3
GBM	Grenier-Bretherton-McCaa
GD	Grell-Devenyl
GF	Grell-Freitas
GFS	Global Forecasting System
GWEC	Global Wind Energy Council
HUJI	Hebrew University of Jerusalem
IBL	Internal boundary layer
IRENA	International Renewable Energy Agency
ITCZ	Intertropical Convergence Zone
KF	Kain-Fritsch
LS	Land surface

LT	Local time
LWR	Longwave radiation
MAE	Mean absolute error
ME	Mean error
ML	Mixed layer
MP	Microphysics
MRF	Medium Range Forecast
MYJ	Mellor-Yamada-Janjic
MYNN2	Mellor-Yamada Nakanishi Niino level 2.5
MYNN3	Mellor-Yamada Nakanishi Niino level 3.1
MERRA	Modern Era Retrospective-analysis for Research and Applications
NASA	National Aeronautics and Space Administration
NBIAS	Normalized Bias
NCEP	National Centers for Environmental Prediction
NCEP-CFSR	NCEP Climate Forecast System Reanalysis
NCEP-FNL	NCEP Final Operational Global Analysis
NCEP-R2	NCEP Reanalysis 2
NMM	Nonhydrostatic Mesoscale Model
NN	Neural network
NOAA	National Oceanic and Atmospheric Administration
NRMSE	Normalized Root Mean Square Error
NSAS	New Simplified Arakawa-Schubert
NWP	Numerical Weather Prediction
OISST	Optimum Interpolation Sea Surface Temperature
ONS	Operador Nacional do Sistema
OSAS	Old Simplified Arakawa-Schubert
PBL	Planetary boundary layer
PDF	Probability density function
PROINFA	Programa de Incentivo às Fontes Alternativas de Energia Elétrica
PSWF	Pedra do Sal wind farm
PX	Pleim-Xiu
QNSE	Quasi-Normal scale elimination
RL	Residual layer
RMSE	Root Mean Square Error

SBL	Stable boundary layer
SBU-YLin	Stony-Brook University Lin
SL	Surface layer
SST	Sea Surface Temperature
STD	Standard deviation
STDE	Standard Deviation of the Error
SWR	Shortwave radiation
TEMF	Total Energy – Mass Flux
UCAR	University Corporation for Atmospheric Research
USGS	United States Geological Survey
UTC	Coordinated Universal Time
UW	University of Washington
WDM5	WRF Double-Moment 5-class
WDM6	WRF Double-Moment 6-class
WEC	World Energy Council
WPS	WRF Pre-processing System
WRF	Weather Research and Forecasting
WRF-DA	WRF Data Assimilation
WSM3	WRF Single-Moment 3-class
WSM5	WRF Single-Moment 5-class
WSM6	WRF Single-Moment 6-class
YSU	Yonsei University

LIST OF SYMBOLS

Latin alphabet:

a	[-]	Power law exponent
A	[m ²]	Transversal area
C	[kg/m ³]	Concentration of a scalar
c_p	[J/(kg K)]	Specific heat at constant pressure for dry air
E	[kg/(m ³ s)]	Phase change rate
E_c	[J]	Kinetic energy
F	[N]	Force
f_c	[s ⁻¹]	Coriolis parameter
g	[m/s ²]	Gravity acceleration
k	[-]	von Kármán constant
H_0	[W/(m ² K)]	Kinematic heat flux
L	[m]	Obukhov length
L_v	[J/kg]	Latent heat of water
m	[kg]	Mass
p	[Pa]	Pressure
p_h	[Pa]	Hydrostatic component of the pressure in each vertical level
P_v	[W]	Available power in the wind
P	[W]	Power
Q_j^*	[W/m ²]	Component of net radiation
q_T	[-]	Total specific humidity of air
r	[-]	Pearson's correlation coefficient
S_C	[kg/(m ³ s)]	Sum of other(s) body source/sink term(s)
S_{qT}	[kg/(m ³ s)]	Sum of other(s) moisture source/sink term(s)
t	[s]	Time
T_0	[K]	Surface temperature
T_v	[K]	Virtual temperature
$u(z)$	[m/s]	Horizontal wind speed as a function of z
u^*	[m/s]	Friction velocity
v	[m/s]	Speed
U_i	[m/s]	Wind speed components
x_i	[-]	Cartesian coordinates
z	[m]	Vertical height
z_0	[m]	Roughness length

Greek alphabet:

δ_{ij}	[-]	Kronecker delta
\mathcal{E}_{ijk}	[-]	Unit tensor
ζ	[-]	Buoyancy parameter
η	[-]	Vertical coordinate system in hydrostatic pressure
θ	[K]	Potential temperature
θ'_i	[-]	Forecast error at an instant i
θ_i^p	[-]	Predicted value at an instant i
θ_i^{obs}	[-]	Observed value at an instant i
μ	[Pa]	Hydrostatic pressure difference between surface and top of the model
ν	[m ² /s]	Air kinematic viscosity
ν_C	[m ² /s]	Molecular diffusivity of C
ν_q	[kg/(m ³ s)]	Molecular diffusivity for water vapor in the air
ν_θ	[m ² /s]	Thermal diffusivity
ρ	[kg/m ³]	Moist air density
σ_{θ^p}	[]	Standard deviation of the predicted dataset
$\sigma_{\theta^{obs}}$	[]	Standard deviation of the observed dataset
$\Psi(\zeta)$	[-]	Universal function
\mathcal{R}	[J/(kg K)]	Gas constant for dry air

SUMMARY

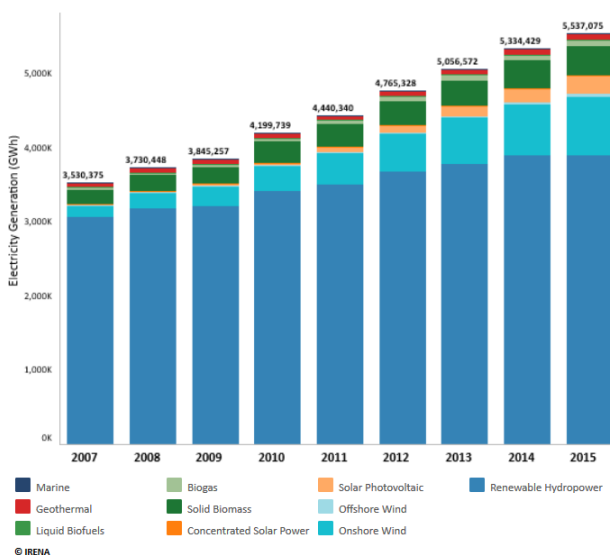
1	INTRODUCTION	35
1.1	Objectives	37
1.2	Relevance and contributions.....	38
1.3	Outline	39
2	THEORETICAL BACKGROUND	41
2.1	The atmosphere.....	41
2.1.1	Atmospheric boundary layer.....	41
2.1.1.1	Turbulence.....	43
2.1.1.2	Basic governing equations.....	44
2.1.1.3	Vertical structure of the wind	47
2.1.1.3.1	Logarithmic law.....	48
2.1.1.3.2	Power law	49
2.1.2	Global winds.....	50
2.1.3	Local winds.....	52
2.1.3.1	Sea and land breezes.....	52
2.1.4	Coastal meteorology	53
2.1.5	Wind energy production	54
2.2	Numerical weather prediction	56
2.2.1	Global models.....	57
2.2.2	Limited-area models	57
2.2.2.1	The Weather Research and Forecasting model.....	57
2.2.2.1.1	Vertical coordinate	58
2.2.2.1.2	Spatial discretization of the equations	59
2.2.2.1.3	Physical parameterizations	60
2.2.2.1.4	PBL Parameterization.....	64
2.2.2.1.5	Nesting.....	65
2.2.3	Wind Power Prediction.....	65
2.2.3.1	Artificial Neural Network.....	66
2.2.3.1.1	Artificial neuron model.....	67
2.2.3.1.2	Network architectures.....	67
3	LITERATURE REVIEW	69
3.1	Wind prediction in coastal areas	69
3.2	Wind predictions with the WRF model	73
3.3	Application of ANN	82
4	MATERIALS AND METHODS	85
4.1	Pedra do Sal Wind Farm	85
4.2	Experimental Data.....	87
4.3	Simulated data	89
4.3.1	Atmospheric simulation.....	89

4.3.2	Wind power simulation	93
4.4	Forecast Verification	95
5	RESULTS.....	98
5.1	Sensitivity test	98
5.1.1	Boundary layer schemes.....	98
5.1.2	Wind speed simulations.....	99
5.1.3	Weibull simulations.....	101
5.1.4	Wind direction simulations.....	102
5.1.5	Conclusions	103
5.2	Horizontal interpolation approach	104
5.2.1	WRF wind speed simulation	105
5.2.2	WRF interpolations with one domain.....	106
5.2.3	WRF interpolation with one domain and nested simulations	108
5.2.3.1	Wind speed.....	108
5.2.3.2	Weibull Probability Density Function.....	109
5.2.3.3	Temperature	110
5.2.3.4	Wind direction.....	112
5.2.3.5	Wind roses.....	113
5.2.4	Conclusions	114
5.3	Horizontal interpolation approach applied in the wind power prediction.....	116
5.3.1	Conclusions	123
6	FINAL CONSIDERATIONS	125
6.1	FURTHER STUDIES	127

1 INTRODUCTION

Renewable energy sources have been increasing their contributions to the world energy matrix in the last years. Some of the factors driving this growth were sustainable policies, aiming to attenuate the climate changes, a greater efficiency in the conversion of these energies and an increase in cost competitiveness (IRENA, 2017). Among these renewable energy sources, wind energy has the fastest growth in the world, as can be seen in Figure 1, even surpassing the solar energy development (EIA, 2017). Between 2010 and 2016, the worldwide installed wind capacity increased by 146%, from 197.9 GW to 486.7 GW (GWEC, 2017). Additionally, in 2015, wind energy was the leader technology in new power generation (GWEC, 2016a), with 63 GW of new installed wind projects worldwide (GWEC, 2016b).

Figure 1 – Renewable energy generation from 2007 to 2015.



Source: IRENA, 2018.

In the coming years, wind energy will continue to grow, although at a lower rate than in the last years. Forecasts show a 68% increase of the installed capacity in 2021 compared to 2016, as well as a cumulative capacity growth rate of 10.4% in 2021 (GWEC, 2017), as shown in Figure 2. The arguments that support the expansion and exploitation of the wind

power source are its renewable characteristic, abundant availability, perennially, zero cost of the fuel (the wind) and zero CO₂ emissions.

Figure 2 – Wind energy forecast from 2017 to 2021.



Source: GWEC, 2017.

Furthermore, the consolidation of wind as a viable source of energy led to a reduction in the costs of wind turbines, in machinery installation and in wind energy contracting. The price of the wind turbine has fallen by about a third since 2009 (IRENA, 2017), while the expenses of installing onshore wind farms, on a global average, decreased by two-thirds between 1983 and 2014 (IRENA, 2016). Also, the reduction in the contracting costs made possible for the wind energy to show the lowest electricity tariff among renewable energy sources in 2016 (WEC, 2016), enabling the wind energy to compete economically with other energy sources and to leverage its development.

This consolidation and growth of the wind energy industry is also seen in Brazil, along with the reduction in the contracting cost, as showed in the last energy auctions (DAMAS, 2013; CCEE, 2018). By the end of 2017, Brazil was among the ten countries with the highest wind installed capacity, at the eighth position, with 12.76 GW (GWEC, 2018). And, until April, 2018, 207 new wind projects were bestowed by ANEEL, totaling 4.59 GW of power (ANEEL, 2018). In terms of energy matrix, wind energy accounted for 5.4% of all consumed energy in Brazil in 2016. Therefore, the wind became the fourth most exploited energy source in the Country, behind hydro, natural gas and biomass (EPE, 2017).

The development of the wind energy in Brazil began with the creation of the Incentive Program for Alternative Sources of Electricity (Pro-

grama de Incentivo às Fontes Alternativas de Energia Elétrica – PROINFA) in 2004, a program founded with the aim to increase the participation of wind, biomass, and small-scale hydropower plants in the Brazilian energy matrix (MELO, 2013). Additionally, in 2015, during COP21 Conference (21st Conference of the Parties), Brazil ensured to reduce greenhouse gas emissions in 43% by 2030, compared to emission levels of 2005. In order to achieve this goal, a target of 23% increase in the renewable energy shares, except hydro, was firmed by 2030 (EPE, 2016), a fact that reinforces the wind energy growth in the Country.

Wind energy is an important source of renewable energy in Brazil and worldwide, that will be even further explored in the near future. However, since the wind velocity has a high temporal variability, the wind energy is intermittent and its production increases or decreases according to the wind speed, which can generate unexpected fluctuations of power in the grid. Therefore, energy system operators rely on numerical weather predictions, and their wind simulations, in order to ensure a balance between supply and demand (ROSGAARD, 2015), making accurate wind forecasts fundamental towards a better exploitation of this energy.

Numerical weather prediction models (NWP) are useful computational tools to simulate the wind, study its local regime and predict its future behavior. However, as these present several configurations, adjusting an atmospheric model according to the characteristics of the study region is a challenging task (CARVALHO et al., 2012).

1.1 Objectives

The aim of this study is to improve the atmospheric simulations of the Weather Research and Forecasting (WRF) model, assessing its physical parameterizations and investigating the onshore and offshore interpolations of its results over Pedra do Sal Wind Farm (PSWF). In addition, a performance evaluation of this suggested interpolation approach will be carried out in the wind power prediction with the use of an Artificial Neural Network (ANN).

In order to achieve the main objective of this work, some specific goals were established:

- Verify the most adequate planetary boundary layer scheme in the WRF model for wind simulations at PSWF during dry months.
- Evaluate the difference that grid point interpolations may result in the WRF atmospheric simulations at PSWF.

- Investigate an alternative approach to improve the wind simulation on a coastal area.
- Assess WRF wind simulations in the atmospheric conditions of Brazil's northeast coast.
- Investigate the combined use of the WRF model and ANN for wind power prediction at PSWF.

1.2 Relevance and contributions

Due to the intermittent nature of the wind, its generation is uncontrolled, a fact that hinders the penetration of this energy into the electrical system. In order to reduce the negative effects of this integration, several strategies of wind and power forecasting have been developed in recent years. Moreover, with a greater insertion of this source in the energy matrix, the improvement of forecasting tools is directly related to energy security. In an energy matrix in which wind actively participates, accurate wind and power prediction models are needed to avoid the lack or restriction of available power in the grid and the unnecessary burn of fossil fuels (WARNER, 2011).

Thus, wind and power forecasting are vital information for the wind energy sector. These predictions are necessary for prospecting and designing new wind farms; financing wind farms, to prove the return of the investment; to help the commercialization of energy; to assist the maintenance and safety of the park, as it informs extreme wind conditions that could damage the equipment; also improves the technical and economical integration of the wind power in the electrical system. Regarding the wind energy integration into the grid, since in practice the energy supply system already exists and it was not designed for load fluctuations, the wind power predictions provide the expected amount of wind energy throughout the day and for the next few days. Therefore, with a good wind power forecasting, the variation of the energy production is known, which reduces the randomness attributed to wind energy (FOCKEN; LANGE, 2006).

With the increased penetration of the wind power into the grid, transmission system operators require wind power generation forecasts, with the aim to guarantee the energy supply and load balance into the system (WEC, 2016). In Brazil, the National Electrical System Operator (Operador Nacional do Sistema - ONS) demands wind power generation agents to provide forecasts of the wind energy production up to 120 hours

ahead in 30 min averages, to optimize the country's energy resources (ONS, 2016).

The relevance of accurate wind and wind power predictions are evident for the consolidation of this energy, forecast improvements are directly related to the reduction of energy costs, facilitating the energy commercialization and its integration into the system (DRAXL, 2012). Therefore, this study aims to contribute to the strengthening of the wind energy in Brazil through the evaluation and optimization of wind simulations obtained by the WRF model at Pedra do Sal wind farm, as well as through the analysis of wind power predictions obtained by the combination of NWP and ANN models. The WRF is a widely used mesoscale numerical model that contains numerous physical options that combine with each other in a non-linear and complex way (GIANNAROS et al., 2017). Also, artificial neural networks have been successfully applied in several areas of wind energy, including wind power forecasting (ATA, 2015).

The studied wind farm is located on a coastal area of Northeast Brazil, in a flat terrain, with a 100 m meteorological mast installed at 400 m away from the Atlantic Ocean. The accurate simulation of the wind in the tropics is a challenge for weather forecasting models, since this region is predominantly dominated by local and mesoscale circulations and susceptible to rapid changes due to convection and sea breeze (SURUSSAVADEE, 2017). In addition, as in coastal areas there are abrupt thermal, roughness and surface changes, between sea and land, these areas also introduce additional challenges in the wind and in atmospheric simulations by numerical models (BARTHELMIE et al., 2007).

Brazil has one of the largest coastlines in the world and most of its wind farms are located near the coast and in the tropical zone. These facts, allied to a few studies that suggest improvements in the wind simulation over coastal regions, foster the importance of this work, which can also assist the Brazilian wind industry to better predict the wind resources of the country. Furthermore, in coastal areas, the wind from sea sectors presents similar features to offshore winds, therefore, a better understanding and forecast of coastal winds can help the future development of the offshore wind energy in Brazil (COELINGH et al., 1998).

1.3 Outline

This thesis is structured as follows: Chapter 2 presents the theoretical background of the atmosphere, englobing the atmospheric boundary layer, global and local wind and coastal meteorology, as well as numerical

weather prediction principles and models. Chapter 3 is dedicated to the literature review of the state-of-the-art on wind prediction in coastal areas, wind forecast with WRF models and artificial neural network applications in wind forecasting. The materials and methods employed in this study are described in Chapter 4, while in Chapter 5 the results are presented in three parts: planetary boundary layer WRF sensitivity test, horizontal interpolation approach of the WRF output data and artificial neural network application for wind power prediction. Lastly, the Chapter 6 concludes the work with final considerations and further studies.

2 THEORETICAL BACKGROUND

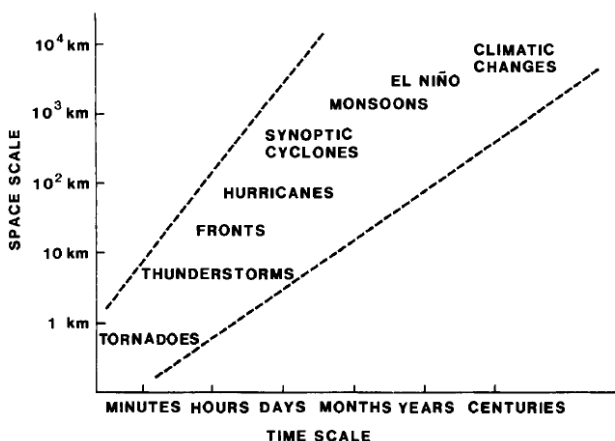
2.1 The atmosphere

2.1.1 Atmospheric boundary layer

The atmosphere is a thin film formed by a mixture of gases that surrounds the Earth's surface under the action of the gravitational force (FOX et al., 2014). This is a complex system that generates chaotic movements due to the interaction of different physical processes, popularly called climate (STULL, 2015). These atmospheric movements happen at different scales of time and space, as depicted in Figure 3, which can be divided into three major categories: micro, meso and macro scale.

The first group of atmospheric circulations is the microscale, where phenomena happen less than a kilometer from the surface and have a duration of seconds or minutes, e.g. tornadoes. The second is called mesoscale, which includes circulations at a height between 1 to 100 km, lasting from hours up to days, as thunderstorms, fronts and hurricanes. The third is the macroscale and represents the large circulations above 100 km, which can be further separated into synoptic (100-5000 km from days to months) and planetary (>5000 km from months to years), such as synoptic cyclones, monsoons, El Niño and climatic changes (NELSON, 2009).

Figure 3 – Space and time scales of atmospheric systems.



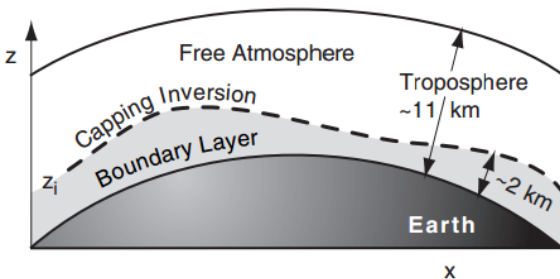
Source: Hsu, 1988.

The horizontal range of the atmosphere is equal to the surface's area of the Earth; while its vertical range extends from the soil surface, without a distinct upper limit. Vertically, the atmosphere can be divided into layers regarding its different features, mainly in terms of temperature (AGUADO; BURT, 2015). The closest layer to the ground is the troposphere, where most climatic events occur. In mid-latitudes, it extends from the surface to approximately 11 km above ground level (a.g.l.), while reaching an altitude of 16 km at the equator and 8 km over the polar regions (PIDWIRNY, 2014). Additionally, the troposphere can be divided into sublayers, as shown in Figure 4 (STULL, 1988).

The lower part of the troposphere, is the atmospheric boundary layer (ABL), also called planetary boundary layer (PBL), which is a region of variable thickness, fluctuating from a few meters to a few kilometers, that is directly influenced by the interactions between the Earth's surface and the atmosphere (STULL, 1988). Such surface/atmosphere interactions occur through the exchange of momentum, heat and scalars (as water vapor), which may be affected by turbulence (TAMPIERI, 2017).

In fact, turbulence is one of the characteristics that causes this separation in the troposphere. In the ABL there is a high occurrence of turbulence near the ground, while outside this region, in the free atmosphere, the turbulence is found mainly in convective clouds and in jet streams (STULL, 1988). Between these two layers, there is a capping inversion (Figure 4, dashed line) that separates the turbulent mixing in the boundary layer from the unmixed atmosphere of the free atmosphere region (STULL, 2015).

Figure 4 – The troposphere structure.

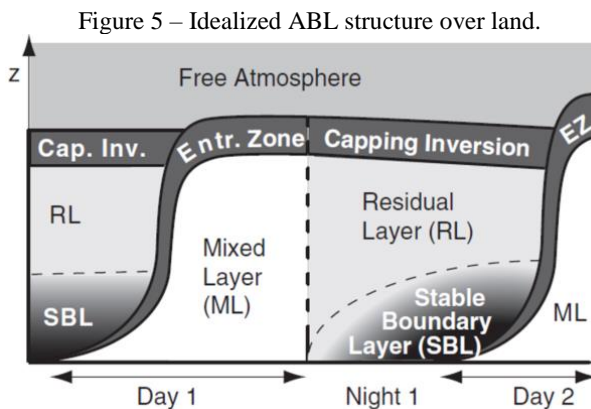


Source: Stull, 2015.

In addition, at the first 10% of the ABL, around 20 to 200 m, there is the surface layer, where a significant change in wind speed, temperature and humidity occurs with height; due mainly to evaporation of the surface

water, heat exchange and drag. This lowest layer is also known as a constant flux layer, because there is no considerable difference in the turbulence flux with height (ARYA, 2011; STULL, 2005).

Thus, under fair-weather (moderate weather with no extreme conditions), the atmospheric boundary layer over land can be divided into an idealized mean structure along the day. The regions of different features are shown in Figure 5; where stable, unstable and neutral stabilities are represented in dark grey, white and light grey, respectively. At daytime, the boundary layer is characterized by an unstable mixed layer (ML); whereas at night, there is the development of a stable boundary layer (SBL) under a neutral residual layer (RL). Additionally, there is an entrainment zone (EZ) between the free atmosphere and the mixed layer, which is a region of non-continuous turbulence. However, at night, when the turbulence stops at EZ, the transition layer is named capping inversion (CI). Both EZ and CI layers have a strong atmospheric stability (STULL, 2005).



Source: Stull, 2005.

2.1.1.1 Turbulence

One of the atmospheric motions of the microscale is turbulence, which can be defined, in a simplified manner, as chaotic and very irregular motions of air volume, known as turbulent elements or turbulent eddies. These disordered and heterogeneous movements are generated due to instabilities in the air flow, with the aim to reduce them (WALLACE; HOBBS, 2006).

There are several ways that turbulence may be induced. The mechanical turbulence, or forced convection, is generated by a dragging

force or obstacles (wake turbulence). The thermal (convective) turbulence, or free convection, happens because of the opposite motion of the cold and warm air, driven by the buoyancy force. And, lastly, by inertial energy, where large eddies can create smaller ones, a phenomenon named turbulent cascade (WALLACE; HOBBS, 2006).

Overall, turbulence has the following features: irregularity/randomness, rotationality and three dimensions, diffusivity, dissipativeness, and multiplicity of motion scales. The first characteristic makes these movements difficult to predict. The second represents that both the velocity and the vorticity fields are three-dimensional, as well as the flow is rotational. The third means that the turbulent movements are efficient in the mixture of properties, as momentum, heat and mass. The fourth express that there is a continuous dissipation of the kinetic energy of turbulent motion by viscosity. The last describes that the turbulence flow has different sizes, in which large eddies are responsible for the energy transfer between the average flow and the turbulence, and the small eddies for the viscous dissipation (ARYA, 2001). Moreover, the size of the turbulent eddies increases with the distance to the ground surface, where near the ground are found the smallest elements, that also have the highest frequency. Thus, all these features make turbulence one of the most effective exchange process between the atmosphere and the surface (FOKEN, 2008).

2.1.1.2 Basic governing equations

According to Stull (1988), there are some basic equations that govern the boundary layer meteorology, which are based on the fluid mechanics equations that describe the dynamics and thermodynamics of atmospheric gases. These equations are the equation of state, the conservation equations for mass, momentum, moisture and heat, as well as the conservation equation for a scalar quantity, such as other gases or aerosols. After splitting the variables into mean (denoted by $\overline{(\)}$) and turbulent (denoted by $(\)'$) parts and applying some simplifications, approximations and scaling analysis (such as assuming incompressibility, Reynolds averaging, Newtonian fluid, Boussinesq approximation), the basic equations can be expressed by:

- The equation of state:

$$\bar{p} = \bar{\rho} \mathcal{R} \bar{T}_v. \quad (2.1)$$

- Conservation of mass:

$$\frac{\partial \overline{U}_j}{\partial x_j} = 0. \quad (2.2)$$

- Conservation of momentum:

$$\frac{\partial \overline{U}_i}{\partial t} + \overline{U}_j \frac{\partial \overline{U}_i}{\partial x_j} = -\delta_{i3}g + f_c \mathcal{E}_{ij3} U_j - \frac{1}{\rho} \frac{\partial p}{\partial x_i} + \nu \frac{\partial^2 \overline{U}_i}{\partial x_j^2} - \frac{\partial(\overline{u'_i u'_j})}{\partial x_j} \quad (2.3)$$

I II III IV V VI VII

where the terms represent: I - the storage of mean momentum (inertia), II - the advection of mean momentum by the mean wind, III - the gravity action (that acts only in the vertical direction), IV - the Coriolis effects (influence of earth's rotation), V - the pressure gradient forces, VI - the viscous stress, VII - the Reynolds' stress on the mean motion (or the divergence of turbulent momentum flux).

- The conservation of moisture:

$$\frac{\partial \overline{q}_T}{\partial t} + \overline{U}_j \frac{\partial \overline{q}_T}{\partial x_j} = \nu_q \frac{\partial^2 \overline{q}}{\partial x_j^2} + \frac{S_{qT}}{\rho} - \frac{\partial(\overline{u'_i q'_T})}{\partial x_j} \quad (2.4)$$

I II VI VIII VII

where the terms represent: I - the storage of the total mean moisture, II - the advection of mean total moisture by the mean wind, VI - the mean molecular diffusion of water vapor, VIII - the mean net body source term for additional moisture processes, VII - the divergence of turbulent moisture flux.

- The conservation of heat:

$$\frac{\partial \overline{\theta}}{\partial t} + \overline{U}_j \frac{\partial \overline{\theta}}{\partial x_j} = \nu_\theta \frac{\partial^2 \overline{\theta}}{\partial x_j^2} - \frac{1}{\overline{\rho} c_p} \frac{\partial \overline{Q}_j}{\partial x_j} - \frac{L_v E}{\overline{\rho} c_p} - \frac{\partial(\overline{u'_j \theta'})}{\partial x_j} \quad (2.5)$$

I II VI VIII IX VII

where the terms represent: I - the mean storage of heat, II - the advection of heat by the mean wind, VI - the mean molecular diffusion of heat conduction, VIII - the mean net body source associated with radiation divergence, IX - the body source term

associated with latent heat release, VII - the divergence of turbulent heat flux.

- The conservation of a scalar quantity (assuming C as its concentration):

$$\frac{\partial \bar{C}}{\partial t} + \overline{U_j} \frac{\partial \bar{C}}{\partial x_j} = \nu_c \frac{\partial^2 \bar{C}}{\partial x_j^2} + S_c - \frac{\partial(\overline{u_j'c'})}{\partial x_j} \quad (2.6)$$

I II VI VIII VII

where the terms represent: I - the mean storage of C, II - the advection of C by the mean wind, VI - the mean molecular diffusion of C, VIII – the mean net body source term for additional C processes, VII - the divergence of turbulent flux of C.

In the equations above, p is the pressure, ρ the moist air density, T_v the virtual temperature, \mathcal{R} the gas constant for dry air ($\mathcal{R} = 287 \text{ J}/(\text{kg K})$), U_i represents the wind speed components ((u, v, w) for $i = (1, 2, 3)$), x_i represents the cartesian coordinates ((x, y, z) for $i = (1, 2, 3)$), t is time, δ_{ij} is the Kronecker delta, g the gravity, f_c Coriolis parameter, \mathcal{E}_{ijk} is the unit tensor, ν is the air kinematic viscosity, q_T is the total specific humidity of air, ν_q is the molecular diffusivity for the water vapor in the air, S_{qT} is a sum of other(s) moisture source/sink term(s), θ is the potential temperature, ν_θ is the thermal diffusivity, Q_j^* component of the net radiation, L_v latent heat of water, E the phase change rate, c_p specific heat at constant pressure for dry air, ν_c is the molecular diffusivity of C, S_c is a sum of other(s) body source/sink term(s) (STULL, 1988).

It is noticeable that the last four equations contain nonlinear terms that model turbulence, the double correlations (or second moment), which are an important consequence of the Reynolds averaging (STULL, 1988; ARYA, 2001). However, despite the simplifications made, the system of differential equations that model the atmospheric boundary layer have more unknowns than number of equations, which turns them analytically unsolvable (unclosed), a problem also known as the closure problem of turbulence, since it is associated with the nonlinearity of turbulence (ARYA, 2001; STULL, 1988). Therefore, in order to solve the equations, some assumptions, called closure techniques, need to be made, where the closure order is named according to the highest order of the parameters that are explicitly calculated by the prognostic equations (FOKEN, 2008).

In first-order closure the mean variables (e.g.: \bar{U}_i) are solved, whereas the Reynolds stress and fluxes (e.g.: $\overline{u'_i u'_j}$) are parameterized. In second-order closure, mean variables and double correlations (e.g.: \bar{U}_i and $\overline{u'_i u'_j}$) are solved, while triple correlations (e.g.: $\overline{u'_i u'_j u'_k}$) are approximated (STULL, 1988). Thus, the greater the order of the closing technique, the more extensive is the calculation (FOKEN, 2008). In addition, there are closure techniques that use only part of the equations available within each category; as the 1.5 order closure, where some double correlations are solved, but not all contained in the equation (STULL, 1988).

The closure techniques can also be defined as local and nonlocal. For local closure, the parameterization of an unknown variable is made from the value of a known variable at the same point in space; whereas for nonlocal closure, the parameterization is made from variables located in different points in space (STULL, 1988).

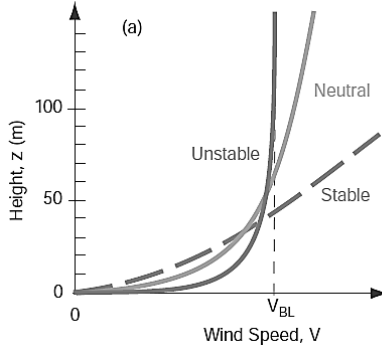
2.1.1.3 Vertical structure of the wind

The vertical structure of the wind, which is the horizontal wind speed variation with height, depends on various meteorological parameters, such as the vertical distribution of temperature and humidity, which determines the atmospheric stability (HAU, 2013). When temperature and humidity in the ABL vary with height, density stratification will occur, leading to vertical movements of air volumes that aim to balance these gradients, named the turbulent eddies (ARYA, 2001).

These air volumes under the action of buoyancy forces can be accelerated or decelerated. If these volumes are accelerated and, therefore, its vertical movement is enhanced, it is said that the atmosphere is statically unstable; whereas if these volumes are decelerated, the atmosphere will be stable (or stably stratified); and, finally, when there is no temperature/humidity gradient in the ABL, the atmosphere is considered neutral (ARYA, 2001). Hence, the stability of the atmospheric boundary layer may be characterized as the tendency to withstand vertical movements and suppress turbulence (MANWELL et al., 2009).

The wind speed profiles for unstable, neutral and stable atmospheric stabilities are depicted in Figure 6. Under unstable conditions, the wind speed increases more rapidly with height than under stable conditions, mainly due to stronger turbulence. Furthermore, under neutral conditions wind speed decreases from a value where it is no longer influenced by the characteristics of the terrain (geostrophic wind) to zero near the land surface.

Figure 6 – Wind speed profile under different static stabilities (where V_{BL} is the boundary layer mean wind speed).



Source: Wallace and Hobbs, 2006.

2.1.1.3.1 Logarithmic law

In general, under static neutral conditions, the wind flow over land in the boundary layer assumes a nearly logarithmic wind speed profile, defined as:

$$u(z) = \frac{u^*}{k} \ln\left(\frac{z}{z_0}\right), \quad (2.7)$$

where $u(z)$ is the horizontal wind speed as a function of the vertical height z , u^* is the friction velocity, k is the von Kármán constant and z_0 is the roughness length. The von Kármán constant is equal to 0.4 and the roughness length is defined as the vertical height from the land surface, where the wind has zero velocity (STULL, 1988). Thus, different types of terrain have different roughness lengths.

However, when the atmospheric boundary layer does not have near-neutral conditions, it is necessary to correct the stability in the profile equation, in order to properly ascertain the velocity of near-surface winds at a determined height (BARTHELMIE, 1999). In this context, the Monin-Obukhov similarity theory is the most acceptable framework to correct the logarithmic relation in the atmospheric surface layer (ARYA, 2001).

Initially proposed by Monin and Obukhov in 1954, the similarity theory uses a dimensionless stability parameter, called buoyancy parameter (ζ), to characterize the mean flow and turbulence in the horizontally homogeneous surface layer (ARYA, 2001). This buoyancy parameter is a function of the vertical height z by the Obukhov length L :

$$\zeta = \frac{z}{L}, \quad (2.8)$$

$$L = -u_*^3 / [k(g/T_0)(H_0/\rho c_p)], \quad (2.9)$$

where u^* is the friction velocity, g/T_0 is the buoyancy variable (g is the gravity acceleration and T_0 is the surface temperature), $H_0/\rho c_p$ is the surface kinematic sensible heat flux (H_0 is the kinematic heat flux, ρ is the air density and c_p is the specific heat) and k is the von Kármán constant.

To extend the logarithmic law to non-neutral atmospheric conditions, the Obukhov length is incorporated in the Equation (2.7) using a universal function $\Psi(\zeta)$:

$$u(z) = \frac{u^*}{k} \left[\ln \left(\frac{z}{z_0} \right) - \Psi(\zeta) \right]. \quad (2.10)$$

There are different representations for the universal function, in which several experiments were conducted in order to determine the stability correction. However, the most used one was created by Businger et al. (1971) and modified by Höögström (1988) (FOKEN, 2008). For unstable atmospheric stratification, the Obukhov length and, consequently, the stability parameter assume negative values, since the heat flux is directed from the ground to the atmosphere (negative). On the other hand, for stable atmospheric conditions, the heat flux is from the atmosphere to the ground (positive) and the stability parameter assumes positive values (EMEIS, 2013). Thus, the universal function for different atmospheric stabilities can be described by the following expressions:

$$\Psi = \begin{cases} -5 \frac{z}{L}, & \text{for } \frac{z}{L} > 0 \text{ (stable)} \\ 0, & \text{for } \frac{z}{L} = 0 \text{ (neutral)} \\ \ln \left[\left(\frac{1+x^2}{2} \right) \left(\frac{1+x}{2} \right)^2 \right] - 2 \tan^{-1} x + \frac{\pi}{2}, & \text{for } \frac{z}{L} < 0 \text{ (unstable)} \\ x = \left(1 - 16 \frac{z}{L} \right)^{\frac{1}{4}}. & \end{cases} \quad (2.11)$$

2.1.1.3.2 Power law

Unlike the logarithmic law that was physically derived, the power law is an empirical equation (EMEIS, 2013) that describes the wind velocity change over height according to:

$$u(z) = u_r \left(\frac{z}{z_r} \right)^a, \quad (2.12)$$

where u_r [m/s] is the velocity at the reference height z_r [m], z [m] is the vertical coordinate, u [m/s] is the horizontal wind speed and a is the power law exponent. The value of such exponent depends on the surface roughness and the thermal stability.

2.1.2 Global winds

Global winds are planetary scale atmospheric motions lead by the non-uniform heating of the Earth's surface, where the poles receive less energy per unit of area from the sun than areas located near the equator. Hence, in the equatorial zone, the air temperature is higher, which reduces its density and causes it to rise, generating a pressure drop (low-pressure region). When the air reaches the tropopause, it has already lost much of its thermal energy and begins to spread to the north and south (YORKE, 2010). While the cold air of the poles, of greater density, descends and goes to the low-pressure region. Thus, a global movement of the air masses is generated with the aim to transport the excess of thermal energy from the equator to the poles (LANDBERG, 2016).

Besides the non-uniform solar incidence, the Earth's rotation also strongly influences the global movements of air. The rotation introduces the Coriolis force, also known as the Coriolis effect, that acts perpendicular to the air movement and causes a direction change in the wind. In the northern hemisphere, the Coriolis effect forces the wind to turn right; while in the southern hemisphere, to turn left. In addition, this force is directly related to the latitude, starting from zero in the equator and reaching its maximum at the poles (AGUADO; BURT, 2015).

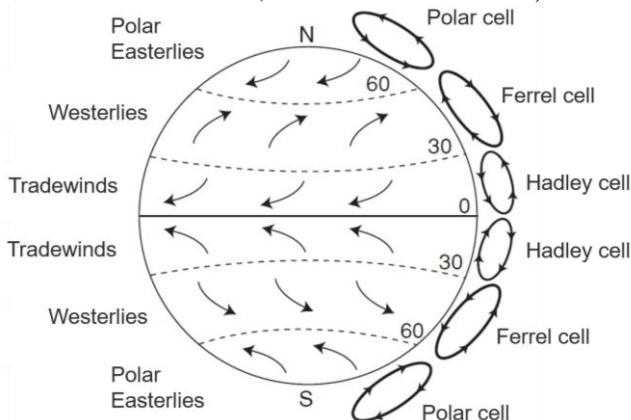
A simplified and idealized model of such atmospheric movements can be seen in Figure 7, which is called the three-cell model. This model represents the main directions of the surface winds and idealizes the circulation of each hemisphere in three cells: Hadley, Ferrel and Polar cells (LUTGENS; TARBUCK, 2012). Between approximately 0° and 30° of latitude to the North and the South, there is the Hadley cell. Close to the equator, due to the solar heating, the warm air rises and moves toward the poles until $\pm 20^\circ$ to $\pm 30^\circ$ latitude, forming a low-pressure zone at the equator, called the equatorial low or the intertropical convergence zone (ITCZ). On the other hand, a high-pressure zone is formed near the subtropics, named the subtropical highs. As there is a pressure gradient in the

lower atmosphere, the surface air is forced to move from the high (subtropical highs) to the low-pressure (ITCZ) zone and, due to the Coriolis force, the air suffers a small deflection to the right direction in the Northern Hemisphere and to the left in the Southern Hemisphere, which creates the northeast and the southeast trade winds (AGUADO; BURT, 2015).

Just above/below the Hadley cell, there is the Ferrel cell, around $\pm 30^\circ$ to $\pm 60^\circ$ latitude. This cell is responsible for the air circulation between the subtropical highs and the subpolar lows, in which the Coriolis force deflects the surface winds to the right in the Northern Hemisphere and to the left in the Southern Hemisphere, forming the winds named westerlies (AGUADO; BURT, 2015).

Lastly, there is the Polar cell above $\pm 60^\circ$ latitude, driven by the thermal gradient, as well as the Hadley cell. In this cell, the surface winds from the polar highs (very cold conditions) move towards the subpolar lows (slightly warmer conditions) and together with the deflection caused by Coriolis force the polar easterly winds are formed (AGUADO; BURT, 2015).

Figure 7 – Global atmospheric motions (arrows indicate the wind direction; closed circulations, the vertical flow of the air).



Source: Jain (modified), 2010.

Additionally, the ITCZ, the convergence zone between the northeast and the southeast trade winds, is considered the most relevant system that causes rain in the equatorial region of the Atlantic, Pacific and Indian Oceans and in the continental areas nearby. However, ITCZ's location is not fixed, presenting seasonal movements. This zone migrates to its northernmost position between August and September, whereas in March and

April its location is more southern in normal (not rainy) years. Therefore, ITCZ is a global meteorological phenomenon that directly affects the climate, and consequently the wind, in the north of the Northeast region of Brazil (CAVALCANTI et al., 2009).

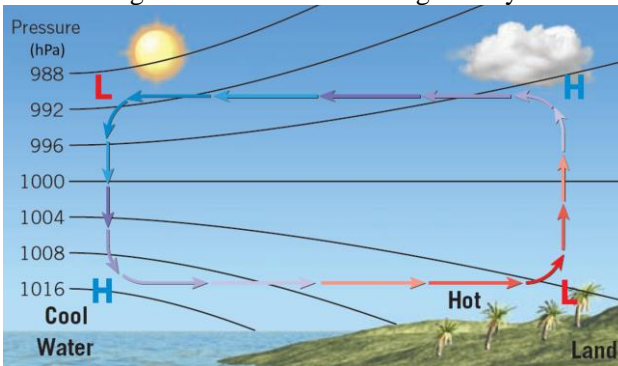
2.1.3 Local winds

In addition to the global wind circulation, there are atmospheric motions in lower levels, near the surface, that are influenced by the characteristics of the soil surface. Thus, each site has distinct features in the wind near the ground, due to interactions with the local orography, which models the wind flow (STULL, 2015). The variation of the energy balance during the day generates thermally induced mesoscale air circulations that, consequently, interact with global circulations. Therefore, the wind in a certain region is the result of the local and global wind interaction (BARRETO; ARAGÃO; BRAGA, 2002).

2.1.3.1 Sea and land breezes

Considering that there is a difference in the specific heat of land and water, a temperature gradient is generated in coastal regions, which induces a mesoscale atmospheric motion. This circulation is responsible for the wind direction change between the day and the night. During the day, with the incident solar radiation, the land becomes warmer than the water nearby, which creates a low-pressure center near the land surface and a high-pressure center aloft, making the wind move from the sea to the land as a sea breeze, according to Figure 8.

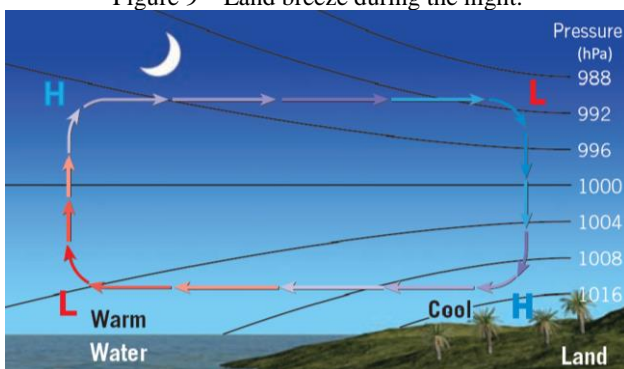
Figure 8 – Sea breeze during the day.



Source: Lutgens and Tarbuck (modified), 2010.

While at night the opposite happens, the ocean loses heat more slowly than the land, becoming warmer; consequently, a low-pressure center is formed near the sea surface and a high-pressure center above it, which induces the wind to circulate from the land to the ocean as a land breeze (Figure 9) (EMEIS, 2013).

Figure 9 – Land breeze during the night.



Source: Lutgens and Tarbuck (modified), 2010.

2.1.4 Coastal meteorology

Coastal meteorology is the area of meteorology that deals with phenomena that occur from the coastline to about 100 km inland and 100 km offshore. These are characterized by the interaction between ocean, land and atmosphere and its heterogeneities, which are related to land/sea differences in surface roughness, temperature, humidity and momentum transfers (ROTUNNO et al., 1992. ROGERS, 1995). Therefore, it is important to understand how the lowest region of the atmosphere, the atmospheric boundary layer, is affected by the sea, the land and this sudden discontinuity between them.

As the ABL is directly affected by the surface characteristics, when there is an abrupt change in surface roughness, e.g. between the sea/land in a coastal area, the wind flow is modified. Therefore, in this zone, the air that blows from the ocean to the land develops an internal boundary layer (IBL) close to the land surface (HSU, 1988). This causes the near-surface wind speed to change and adjust to the different roughness, whereas the aloft wind speed is kept unchanged. The IBL amplitude, in terms of height, depends mainly on three variables: the surfaces roughness, the atmospheric stability and the distance to the surface discontinuity. In addition, the turbulence directly affects the speed at which the layer

will develop; with a high turbulence, the greater will be the mixing and the faster will be the IBL formation (BARTHELMIE, 1996).

2.1.5 Wind energy production

The wind energy production is the conversion of the kinetic energy of the air into electric power, which is typically done by a wind turbine. The air in motion has kinetic energy E_c that is proportional to its mass m and squared speed v^2 , as follows:

$$E_c = \frac{1}{2}mv^2. \quad (2.13)$$

The wind power P_v can be obtained by the derivation in time of Eq. 2.13, taking constant the velocity v ,

$$P_v = \frac{dE_c}{dt} = \frac{1}{2} \left(\frac{dm}{dt} \right) v^2. \quad (2.14)$$

As the mass flow rate of air is obtained by:

$$\frac{dm}{dt} = \dot{m} = \rho A \frac{dx}{dt} = \rho Av, \quad (2.15)$$

where ρ is the air density and A is the transversal area of the wind turbine rotor, the wind power can then be defined as:

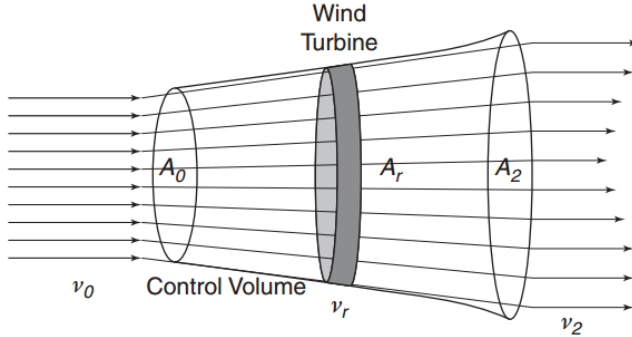
$$P_v = \frac{1}{2} \rho Av^3. \quad (2.16)$$

The air in motion makes the wind turbine blades turn, converting the kinetic energy of the air into rotational mechanical energy in the machine. Posteriorly, with the use of an electric generator, this rotational energy is converted in electric energy, which is then transmitted to the electric system. As the wind passes through the rotor, its speed is gradually reduced and, consequently, the control volume of air expands, as shown in Figure 10. Thus, to calculate the quantity of kinetic energy that a wind turbine can convert into rotational energy, it is necessary to consider the air conditions in the front and behind the rotor (HAU, 2013).

Therefore, the quantity of energy that the wind turbine can extract P is equal to the difference between the input and output air power at the control volume (HAU, 2013). It is considered that the air that enters has velocity v_0 and its control volume has an area A_0 , while the air that goes out has a velocity v_2 and its control volume has an area A_2 , as follows:

$$P = \frac{1}{2}\rho(A_0v_0^3 - A_2v_2^3). \quad (2.17)$$

Figure 10 – Control volume at the wind turbine rotor.



Source: Jain, 2011.

Since the continuity equation requires that the air mass flow rate \dot{m} that enters the control volume must be equal to the air mass flow that leaves the control volume, the Equation 2.17 can be rewritten as:

$$P = \frac{1}{2}\dot{m}(v_0^2 - v_2^2). \quad (2.18)$$

Also, according to the law of conservation of momentum, the force F that the wind does over the turbine rotor is a function of the air mass flow rate \dot{m} and the input and output velocities at the control volume, v_0 and v_2 :

$$F = \dot{m}(v_0 - v_2). \quad (2.19)$$

As the wind applies this force on the rotor, the turbine exerts an opposite force of the same magnitude on the air. Thus, the power required by the turbine is proportional to the force F and the wind speed v_r at the rotor:

$$P = Fv_r = \dot{m}(v_0 - v_2)v_r. \quad (2.20)$$

Equating the two power expressions, Equations (2.18) and (2.20), a relationship for the air wind speed at the rotor can be obtained:

$$\begin{aligned}\dot{m}(v_0 - v_2)v_r &= \frac{1}{2} \dot{m}(v_0^2 - v_2^2), \\ (v_0 - v_2)v_r &= \frac{1}{2}(v_0 - v_2)(v_0 + v_2), \\ v_r &= \frac{1}{2}(v_0 + v_2).\end{aligned}\tag{2.21}$$

Thus, retaking the last power equation (Eq. 2.20) and replacing the expression for the velocity at the rotor (Eq. 2.21), a representation of the mechanical power output converted by the wind turbine is obtained, as a function of its rotor area A_r , air density ρ and input and output velocities at the control volume, v_0 and v_2 :

$$P = \frac{1}{4} \rho A_r (v_0^2 - v_2^2)(v_0 + v_2).\tag{2.22}$$

However, it can be shown that there is a maximum value for the conversion of this power by the turbine, that it is known as Betz limit, which is equal to 59.3% (JAIN, 2010). Additionally, it is important to emphasize that by analyzing the Equation (2.22), it is noticed that an inefficiency in the wind prediction may lead to a big error in the power forecast, since the power is proportional to the wind velocity to the cube.

2.2 Numerical weather prediction

Numerical weather prediction consists of computational tools that mathematically describe the atmospheric behavior in the future, using meteorological observation as initial conditions. This prediction is obtained through the implementation of nonlinear equations, that govern the behavior of nonviscous fluids, and through the assumption that the atmosphere is a thin layer, which results in a system of nonhydrostatic equations known as primitive equations. The equations that establish the atmospheric behavior are the continuity equation, the momentum equation, the energy conservation equation, the water vapor equation and the equation of state (COIFFIER, 2011).

The development of NWP models is directly related to computational evolution and to the advances on meteorological theories (LYNCH, 2008). These models are able to generate forecasts for short and long terms, with a forecast horizon of a few days up to months. Also, they have

the versatility to cover large or small areas. In general, there are two types of models according to the spatial extension of its calculations: the global models and the limited-area (regional) models (WARNER, 2011).

2.2.1 Global models

Global models of numerical weather forecasting cover large areas in their predictions and are concerned with atmospheric phenomena that occur on the global/planetary scale. They use meteorological observations, obtained by satellites and stations, combined with a numerical model for forecasting the future state of the Earth's atmosphere (BURTON et al., 2011). In addition, their output data are generally used as initial and boundary conditions in regional weather forecast models (MONTEIRO et al., 2009).

One of the most widely used global models is the Global Forecasting System (GFS), created by the National Centers for Environmental Prediction (NCEP). GFS is a coupled model composed of four different cores, the atmosphere, ocean, soil and sea ice, which provides information on temperature, winds, ozone concentration, other atmospheric variables, soil moisture and sea data. The model performs forecasts for the entire globe with a base horizontal resolution of 28 km for up to 16 days in the future (NOAA, 2016).

2.2.2 Limited-area models

Limited-area models of numerical weather forecasting evaluate smaller areas than global models. They are concerned with equating and solving atmospheric phenomena that occur at the micro and mesoscale. Additionally, these models can numerically reproduce the processes that happen in the atmospheric boundary layer (ROSGAARD, 2015).

Generally, regional models use as input the forecasted data provided by a global model and obtain forecasts of smaller regions as output data, employing downscaling techniques and incorporating roughness and local orography (ALLAMILLOS et al., 2013). These regional forecasts provide meteorological information of high spatial and temporal resolution, which can, in turn, be used to feed wind power forecasting models (GIEBEL et al., 2011).

2.2.2.1 The Weather Research and Forecasting model

Developed by the joint effort of national agencies and universities, the Weather Research and Forecasting model is a public-domain,

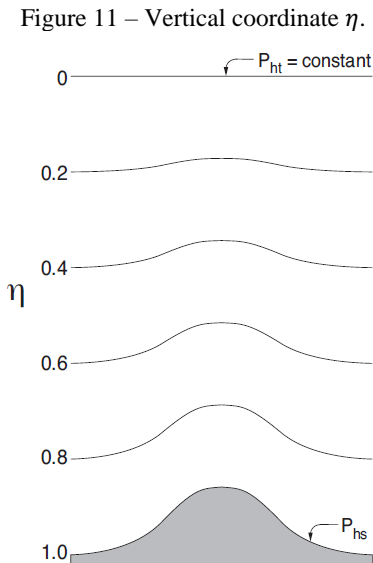
mesoscale numerical weather prediction system applied to the atmosphere. The model has numerous applications, including meteorological studies, numerical weather forecasts, data assimilation, idealized and real simulations, as well as can be coupled with other systems (UCAR, 2016).

The WRF model has two solvers: the Nonhydrostatic Mesoscale Model (NMM) and the Advanced Research WRF (ARW), being the WRF-ARW the one used in this study. The WRF-ARW is a nonhydrostatic solver based on Euler's equations (COIFFIER, 2011) and contains four main programs: WRF Pre-processing System (WPS), WRF Data Assimilation (WRF-DA), WRF Advanced Research (WRF-ARW) and Post-processing and Visualization tools (SKAMAROCK et al., 2008). The architecture of its system is presented in Figure A.1 of Annex A.

The WRF-ARW performs simulations in three spatial dimensions (x, y, z) with a horizontal grid that follows the Arakawa C-grid staggering scheme and terrain following hydrostatic pressure vertical coordinates, called η . In addition, the time-split integration uses third order Runge-Kutta scheme (SKAMAROCK et al., 2008).

2.2.2.1.1 Vertical coordinate

The WRF model uses a vertical coordinate system η in hydrostatic pressure, that accompanies the contour of the terrain (Figure 11).



Source: Skamarock et al., 2008.

This coordinate system is also known as mass vertical coordinate and it is defined by:

$$\eta = \frac{p_h - p_{ht}}{\mu}, \quad (2.23)$$

$$\mu = p_{hs} - p_{ht}, \quad (2.24)$$

where p_h is the hydrostatic component of the pressure in each vertical level, p_{ht} is the pressure value at the top of the atmosphere, and p_{hs} is the pressure value at the surface. Since η varies from 1 to 0, the highest value is on the surface and the smallest, on the top of the atmosphere. Additionally, the vertically performed calculations are not done on each η level, but through a mean between two adjacent levels (SKAMAROCK et al., 2008).

2.2.2.1.2 Spatial discretization of the equations

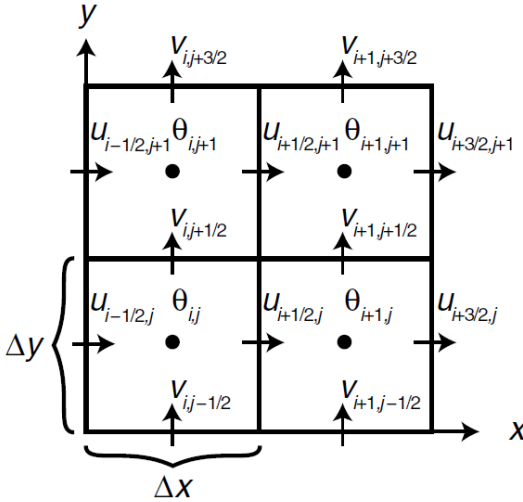
The partial differential equations in the WRF model, governing the atmospheric behavior (compressible, nonhydrostatic Euler equations), cannot be solved by analytical methods; these require numerical methods in which the equations are discretized and solved in a grid (PIELKE, 2013). There are several discretization techniques available, including finite differences, finite volumes and finite elements; and the WRF model uses finite difference as its solution technique. This method evaluates the partial derivatives of a function at a specific point from the differences between the values of this function in the adjacent points of the grid (COIFFEUR, 2012).

The WRF model subdivides the simulation domain, established by the model's user, with a quasi-regular spatial grid, composed of an array of cells, where the model's equations are solved at specific points in the grid. Thus, the discretization of the governing equations is limited by the model resolution and the size of the chosen grid (KALNAY, 2003). As the numerical weather prediction models involve numerous variables in their equations, there are different ways of positioning these models' variables in the grid. One of the possibilities is to evaluate them at different positions in the grid cells, which is called a staggered grid.

The WRF-ARW model uses an Arakawa staggered C-grid for the spatial discretization, which places the horizontal velocities components (u and v) perpendicular to the faces of the grid cell and at a half-cell dis-

tance of the mass, thermodynamic, scalar and chemistry variables (θ), located in the center of the cell grid (Figure 12) (SKAMAROCK et al., 2008). Furthermore, it is possible to include additional grids within a parent domain, with different resolutions, known as nesting. In this way, a better refinement can be obtained for the simulation of the studied area.

Figure 12 – WRF-ARW horizontal grid Arakawa-C.



2.2.2.1.3 Physical parameterizations

The WRF-ARW model presents great versatility, especially with respect to the parameterization of physical processes, which allows sensitivity studies regarding the set of parameterizations that best represent the weather in a place of study. Parameterization in NWP models is the process of representing important physical processes and phenomena without solving them numerically (STENSRUD, 2009), that is, implicitly including them in the model. The physical parameterizations make it possible to correctly simulate the hydrological and energy cycles of the atmosphere, as well as allows the evaluation of the surface fluxes. These are fundamental processes that allow the determination of important weather elements, such as temperature, humidity, near-surface wind, rain-fall and snowfall (COIFFIER, 2012).

In general, there are three main reasons that explain the need to parameterize a physical process. First, there is not enough knowledge of how a process works, thus making it difficult to explicitly represent it

through an equation. Second, a process occurs on a smaller scale than the model's ability to solve the equation, requiring a high computational time. Third, the process has high complexity and a large equation that represents it, which would require an unattainable amount of computational resources to solve it (WARNER, 2011).

The WRF-ARW model has available parameterizations for: microphysics (MP), cumulus (CU), land surface (LS), surface layer (SL), planetary boundary layer (PBL), longwave radiation (LWR) and shortwave radiation (SWR); where the parameterization models of each of these variables are summarized in Table 1, as well as its main features. These multiple parameterization schemes available in the WRF model interact directly and indirectly with each other (DUDHIA, 2014). In a schematic manner, the direct interactions between the schemes of cumulus, microphysics, radiation, surface and PBL are depicted in Figure 13, where SW is shortwave radiation, LW is longwave radiation, SH is sensible heat flux, LH is latent heat flux, T is temperature and Qv is the mixing ratio for water vapor.

Table 1 – Parameterizations of the WRF-ARW model v. 3.6.1.

Microphysics	
Features	Parameterization responsible for the inclusion of the cloud, water vapor and precipitation processes in the model.
Available models	Kessler, Lin et al. (Purdue), WRF Single-Moment 3-class (WSM3), WRF Single-Moment 5-class (WSM5), Eta (Ferrier), WRF Single-Moment 6-class (WSM6), Goddard, Thompson, Milibrandt-Yau double-moment 7-class, Morrison double-moment, CAM 5.1 2-moment 5-class, Stony-Brook University Lin (SBU-YLin), WRF Double-Moment 5-class (WDM5), WRF Double-Moment 6-class (WDM6), NSSL 2-moment, NSSL 1-moment, Thompson aerosol-aware, HUJI (Hebrew University of Jerusalem, Israel).

Cumulus	
Features	Cumulus parameterization handles the effects of convective and/or shallow clouds in the sub-grid scale.
Available models	Kain-Fritsch (KF), Betts-Miller-Janjic (BMJ), Grell-Freitas (GF), Old Simplified Arakawa-Schubert (OSAS), Grell-3 (G3), Tiedtke, Zhang-McFarlane, New Simplified Arakawa-Schubert (NSAS), Grell-Devenyl (GD), Old Kain-Fritsch (old KF).
Land surface	
Features	Parameterization that uses information from other schemes to determine heat and moisture fluxes over land.
Available models	Slab soil (5-layer thermal diffusion), Noah, RUC, Pleim-Xiu (PX), Noah-MP (multi-physics), SSiB, Fractional sea-ice, CLM4.
Planetary boundary layer	
Features	Parameterization that handles the vertical sub-grid scale fluxes caused by the eddy transport in the atmosphere.
Available models	Yonsei University (YSU), Mellor-Yamada-Janjic (MYJ), NCEP Global Forecast System (GFS), Quasi-Normal scale elimination (QNSE), Mellor-Yamada Nakanishi Niino level 2.5 (MYNN2), Mellor-Yamada Nakanishi Niino level 3.1 (MYNN3), Asymmetric Convective Model (ACM2), Bougeault-Lacarre (BouLac), University of Washington (UW), Total Energy – Mass Flux (TEMF), Grenier-Bretherton-McCaa (GBM),

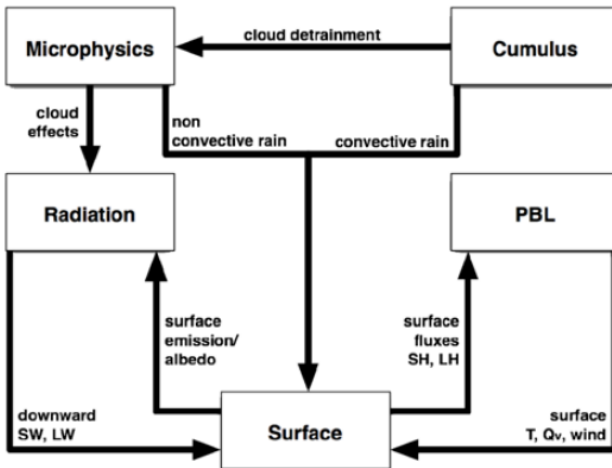
	Medium Range Forecast (MRF).
Surface layer	
Features	Parameterization responsible for the calculation of friction velocities and exchange coefficients.
Available models	MM5 similarity, Eta or MYJ, Pleim-Xiu, QNSE, MYNN, TEMF, Revised MM5.
Longwave radiation	
Features	Parameterization responsible for the inclusion of the longwave radiative fluxes (infrared radiation), which is absorbed and emitted by gases and surfaces.
Available models	RRTM, CAM, RRTMG, New Goddard, Fu-Liou-Gu (FLG), Held-Suarez, GDFL.
Shortwave radiation	
Features	Parameterization responsible for the inclusion of the shortwave radiative fluxes (visible and ultraviolet radiation).
Available models	Dudhia, Goddard, CAM, RRTMG, New Goddard, Fu-Liou-Gu (FLG), GDFL.

Sources: Data from NCAR (2015) and Skamarock (2008).

It is noted that there are several parameterizations for the processes that occur in the boundary layer, which encompass the configurations of surface layer, planetary boundary layer and land surface. The model treats these three parameterizations separately; however, as mentioned, there is

a strong interaction among them, a fact that makes their adjustment process difficult. Additionally, there are some fixed combinations between the planetary boundary layer and the surface layer imposed by the model. The MRF, YSU and ACM2 PBL models are connected to the MM5 SL model; while the MYJ and UW PBL schemes are associated with Eta SL. In contrast, Boulac PBL model is flexible in the choice of the surface layer parameterization (SHIN; HONG, 2011). In front of a wide variety of physical options, multiple authors have been performing sensitivity tests to verify the best choice of WRF parameterization according to the study to be performed and to the characteristics of the analyzed area.

Figure 13 – Interactions between parametrizations.



Source: Dudhia, 2014.

2.2.2.1.4 PBL Parameterization

The parameterization of the planetary boundary layer is responsible for expressing the impact of subgrid-scale turbulent motions on grid-scale variables in the atmospheric column, which can considerably change the representation of turbulent mixing and, consequently, the prediction of the atmospheric state (SHING; HONG, 2011). In this way, numerous studies have raised the importance of PBL schemes in weather prediction by atmospheric numerical models and affirmed that they are a great source of inaccuracies in the simulations (PLEIM, 2007a; SHING, HONG, 2011; CARVALHO et al., 2012, 2014a; ALLAMILLOS et al.,

2013; BALZARINI et al., 2014; BANKS et al., 2016; MILOVAC et al., 2016).

Planetary boundary layer schemes in the WRF model can be divided according to the order of the closure technique and into local and non-local closure regarding its turbulent fluxes parameterization (as presented in Section 2.1.1.1). In Table 2 is shown an overview of some PBL schemes and their closure type. Also, additional information can be found in Pleim (2007b) for ACM2, Bougeault and Lacarrère (1989) for Boulac, Janjic (1993) for MYJ, Nakanishi and Nino (2006) for MYNN2, Bretherton and Park (2008) for UW and in Hong and Noh (2006) for YSU.

Table 2 - Closure type of some planetary boundary layer schemes of the WRF model.

PBL Scheme	Closure type
ACM2	1.0 nonlocal scheme
BouLac	1.5 local scheme
MYJ	1.5 local scheme
MYNN2	1.5 local scheme
UW	1.5 local scheme
YSU	1.0 nonlocal scheme

Source: Banks et al., 2016.

2.2.2.1.5 Nesting

The WRF-ARW model supports the insertion of an additional smaller domain (child domain) within a larger domain (parent domain) into the simulation. This makes it possible to increase the horizontal resolution, consuming less computational time, and allows to focus the simulation on a specific region. The nesting can be performed with two different options: 1-way (unidirectional) or 2-way (bidirectional) nesting. In the first, the information is provided by the parent domain to the child domain; while in the second, the information can be exchanged between the different domains (SKAMAROCK et al., 2008).

2.2.3 Wind Power Prediction

In countries with a large wind energy penetration, wind power prediction is a fundamental information to maintain the proper functioning of the electric power grid. This forecast can be used as input data in simulation tools for energy market operations, dispatch and assessment of the network security. Thus, providing important information to ensure a safe, efficient and economical operation of the power grid (FOX et al., 2014).

Wind power prediction models developed in recent years can be subdivided into three main categories: those that use predominantly physical modeling, those that use statistical techniques and those that integrate the characteristics of both, known as hybrid models. The physical approach uses equations that physically describe the wind regime and the wind turbine power curve to estimate the production of wind power. On the other hand, the statistical approach is based on finding a relationship in the historical data of wind energy yield, which encompasses numerous models, such as artificial neural networks. The statistical method is mainly effective for prediction of up to 6 hours, while the physical approach exhibits better results for a longer prediction horizon, especially in the range of 12 to 48 hours. At last, the hybrid models present smaller prediction errors in comparison with the other two approaches; as well as, they are the most modern and advanced wind power forecast systems (WANG et al., 2011; LEI et al., 2009).

2.2.3.1 Artificial Neural Network

The artificial neural network is a parallel processing system inspired by the basic functioning structure of the human brain and by the cells of the central nervous system (KRUSE et al., 2016). They are formed by simple processing units called neurons, which are interconnected with connection strengths, called synaptic weights. These weights are responsible for storing knowledge, being the learning process the period where knowledge is acquired by the network and when the weights are adjusted (HAYKIN, 2009).

The learning ability is a fundamental feature of neural networks and there are several algorithms available for this procedure. In the learning process, the synaptic weights are optimized based on statistical parameters extracted from data provided to the network. Thus, this learning period is necessary for the network to be configured in a way to produce, through input data, the desired output (YADAV et al., 2015). Additionally, besides the learning period, predictions with neural networks involve another phase to verify and validate the ANN output (TAYLOR, 2006).

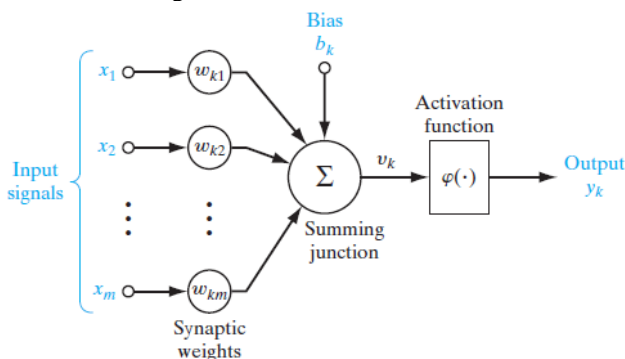
The artificial neural networks present several advantages for the solution of complex problems, when compared to other computational systems. Some of these advantages are: they are faster, using less processing time; they are simple, and have the ability to model a multivariable problem, since they can extract the nonlinear relationship between several variables (ATA, 2015). Furthermore, in the context of wind power

forecasting methodologies, the neural network can handle data that was not used to train the network (LANGE; FOCKEN, 2006).

2.2.3.1.1 Artificial neuron model

The model of the neuron, as the information processing unit of an artificial neural network, is presented in Figure 14. It is composed of three main parts: a set of synapses, an adder and an activation function. The first can also be called connecting links and these are characterized by their weights. The second performs a weighted sum of the input signals. Lastly, the third limits the amplitude of the output signal. In addition, an external Bias is shown in Figure 14, which may increase or decrease the activation function input (HAYKIN, 2009).

Figure 14 – Model of a neuron.



Source: Haykin, 2009.

2.2.3.1.2 Network architectures

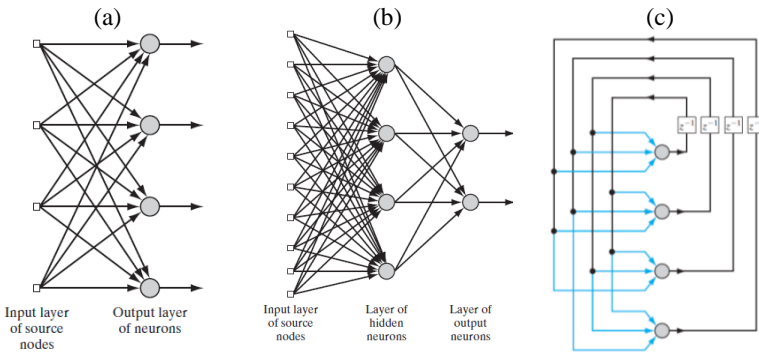
The form of organization of the neurons in the ANN is called network architecture. The best network architecture is the result of the analysis of several combinations, testing different numbers of hidden layers, of neurons in each layer and types of transfer functions (CATALÃO, 2011).

A large number of neurons in the hidden layer can deteriorate the performance of the neural network, since it will store a large amount of specific information of the training data, which is called overfitting. On the other hand, few neurons in the hidden layers are insufficient to properly adjust the synaptic weights in the learning period, which can lead

to an underfitting, resulting also in an inconsistent performance of the network (SHEKHAWAT, 2014; ZHAO et al., 2017).

In general, there are three main architecture classes of the ANN: single-layer feedforward networks, multilayer feedforward networks and recurrent networks. The single-layer feedforward network is the simplest form of a neural network. In this type, the information follows only in one direction, that is forward. This architecture presents one input layer, through which the input variables are exposed to the network, where each input element is connected to an output layer of neurons (Figure 15(a)).

Figure 15 – Single-layer feedforward network (a), multilayer feedforward network (b) and recurrent network (c).



Source: Haykin, 2008.

Just as in the single-layer feedforward network, in the multi-layer feedforward network the signal goes only forward, there is no feedback of the signal. However, this architecture can be composed of several hidden layers, in which the neurons are arranged in a way that each layer receives information from the previous layer and provides information to the next one (Figure 15(b)) (HAYKIN, 2009; YADAV et al., 2015).

At last, the recurrent network can have connections that send the signal both forward and backward and can have arbitrary connections between neurons. Also, this network uses its output data to feedback the system (Figure 15(c)), repeating this process until the network is in equilibrium and the output data does not change (HAYKIN, 2009; YADAV et al., 2015).

3 LITERATURE REVIEW

3.1 Wind prediction in coastal areas

Wind prediction in coastal areas presents several challenges, as affirmed by Barthelmie et al. (2007) on an analysis of the horizontal and vertical profile of wind speeds in a coastal area of Denmark. The study pointed out that these difficulties are a result of the high complexity of the flow, which is caused by the discontinuity in the land/sea surface, the land topography and the temperature gradient. This discontinuity in the surface roughness of land/sea may lead to a development of an internal boundary layer in the wind flow; whereas the land/sea temperature gradient may cause changes in the stability of the atmosphere and influence the occurrence of land/sea breeze (BARTHELMIE; PALUTIKOF, 1996).

Furthermore, the ocean in coastal zones has a nonequilibrium state with large differences in its roughness and in the sea surface temperature (SST) (ROGERS, 1995). These features directly impact the wind speed profile and the location where the wind profile assumes equilibrium conditions, which can cause a considerable wind speed gradient in the horizontal direction and affect the power production forecast of a coastal wind farm. Additionally, the study showed that the coastal zone usually has non-neutral stability conditions, which makes the application of the logarithmic profile not suitable for vertical extrapolations of the wind (BARTHELMIE et al., 2007).

Despite the discontinuity, topography change and the temperature differences of land/sea, there are other factors that influence the wind in coastal areas, such as: temperature gradient between air and sea, coastline orientation, prevailing wind and direction of the wind, ocean depth, location (regarding the latitude and solar radiance of the site), distance from the coastline and fetch (the surface type where the wind blows before its measurement) (BARTHELMIE, 1999). Therefore, the wind flow over coastal regions suffers influences from both sea and land features and by the sudden change between them, which makes wind predictions over these areas not an easy task for numerical atmospheric models that need to represent well these differences in mean values within grid cells.

The difficulties of predicting the wind in coastal areas were observed by Cannon et al. (2017). The authors evaluated the WRF performance to simulate gusty downslope wind events, called sundowners, at Santa Barbara County, from model predictions of 11 days of the spring of 2004 with observational data. The measured data were obtained from 26 in-situ and offshore stations spread in Southern California, while the

model (WRF-ARW v. 3.7.1) was tested with three configurations using different parameterizations. After a sensitivity test, it was found that the best set was WRF-3/A with MYNN PBL scheme and the additional use of the SST data from the Advanced Very High-Resolution Radiometer (AVHRR).

Overall, pressure, temperature and humidity at 2 m were well predicted by WRF, with correlation coefficient values of 0.94, 0.83 and 0.72, respectively. Nonetheless, Cannon et al. (2017) found variations between the correlations of pressure, temperature and humidity in stations located inland and those situated at coastal and offshore areas, which demonstrates the difficulty of mesoscale models in simulating the influence of the sea on the atmosphere. Regarding wind speed simulation, the WRF was not capable to well represent this parameter and the correlation between the model and the measured data was of 0.62. By specifically evaluating wind speed predictions at Santa Barbara Airport station, a coastal site located approximately 1.5 km from the ocean, the results displayed a big deficiency in the model. In one evening, the wind speed was overpredicted by 7 m/s, which highlights the issues encountered by the WRF to simulate coastal areas and the marine layer.

In coastal areas, mainly complex ones, the grid resolution of the forecast model plays an important role in accurately simulating the wind flow, as shown by Cambazoglu et al. (2016). In their analysis over two coastal sites (Turkish Straits and Chesapeake Bay) using the software COAMPS (Coupled Ocean Atmosphere Mesoscale Prediction System), the results showed an increase in the simulation error of the wind speed with the decrease of the model grid resolution, which poorly represents the coastline features. However, it is important to notice that this increase in resolution had a limited effect over wind simulations, for example, in both sites the 3-km resolution performed better than the 1-km, despite considerations of computational cost. In the same manner, the temporal resolution showed a direct correlation with the model accuracy. It was highlighted that the model grid resolution is region dependent, where in one site the wind velocity was overpredicted, while in the other site it was underpredicted.

The dependence of the forecast according to the region to be predicted was also observed by Giannaros et al. (2017), in a study that evaluated the wind simulations of WRF (v. 3.2.1) in the complex terrain of Greece, during the whole year of 2003. In order to evaluate the forecasts, data from ten surface synoptic weather stations were used. Almost all stations, besides one (Larissa), were installed in coastal planar areas, with wind measurements at 10 m a.g.l and 3 h averaged. However, five stations

were located at the mainland and the others five at islands. The main results of the analysis showed that, overall, wind velocity was underestimated by WRF in mainland areas; whereas in island areas, the velocity was overestimated. Nevertheless, it was observed that the positive Bias in the islands happened mostly because of an overestimation of weak winds, below 3 m/s. Thus, only considering the relevant velocities for the wind resource, between 3 to 25 m/s, it can be affirmed that WRF underestimated the wind speed over all sites, for the four seasons of the year. Table 3 presents a summary of the errors calculated between the observed and simulated wind speed to each surface station (Bias, Root Mean Square Error - RMSE and Standard Deviation of the Error – STDE), as well as the approximate distance of the station to the sea and its height above sea level (a.s.l.).

Table 3 – Characteristics and annual mean errors of the wind speed prediction of ten surface weather stations located in Greece.

Location	Station	Approximate distance to the Sea (m)	Height a.s.l (m)	Bias (m/s)	RMSE (m/s)	STDE (m/s)
Greece	Mainland area					
	Aktion	1400	1.00	-0.34	2.59	2.57
	Alexandroupoli	500	3.50	-0.15	2.39	2.38
	Athens	1450	15.00	-0.32	2.16	2.14
	Kalamata	5300	11.10	0.94	2.45	2.26
	Larissa	34400	74.00	-0.56	2.51	2.45
	Islands area					
	Heraklio	1150	25.18	0.25	2.61	2.59
	Kos	1650	27.07	0.02	1.81	1.81
	Lemmos	1070	25.23	0.05	2.01	2.01
Rhodes	640	28.08	0.49	2.88	2.84	
Skyros	1300	24.49	1.65	3.03	2.54	

Source: Data from Giannaros et al., 2017.

In a coastal area of China, at Lingyang wind farm, about 5 km from the sea, Zhao et al. (2012) applied the Kalman filtering processes in order to reduce systematic errors in the WRF wind speed predictions. The

model was configured with four domains (54, 18, 6 and 2 km), with one-way interaction, and input data from GFS. The day-ahead runs covered the year of 2009 with the application of the following main physical parameters: MYJ for planetary boundary layer, WSM5 for microphysics, RRTM and Dudhia for longwave and shortwave radiation, Eta for surface layer, Noah for land surface and KF for cumulus (only in the outer domain). The annual obtained results showed a decrease in the errors of the WRF forecasted wind when using the Kalman filter (mean error – ME, mean absolute error – MAE and RMSE), mainly in the systematic error represented by ME (equal to Bias), which can be seen in Table 4.

Table 4 – WRF wind speed prediction and improved WRF output by Kalman filter for the Lingyang wind farm.

Location	Data	Approximate distance to the Sea (m)	ME (m/s)	MAE (m/s)	RMSE (m/s)
China	WRF output	5000	1.027	1.913	2.491
	WRF output + Kalman filter	5000	4.23E-03	1.452	1.926

Source: Data from Zhao et al., 2012.

In terms of the Brazilian coastline, Jong et al. (2017) analyzed wind power forecasts of wind farms located in the Brazilian Northeast subsystem, based on WRF wind predictions and on a generic wind turbine power curve. It was found that the forecast errors for the wind farms located near the coast were higher in comparison with those inland. Similar results were observed in the work of Ramos et al. (2013), who used the WRF to forecast the wind speed at Alagoas State. The simulations were compared with measurements at six meteorological stations (three near the coast and three inland of the State), with observed wind speeds at 30 m, from August of 2007 to July of 2008. Ramos et al. (2013) found a mean square error of the predictions 37.3% higher in coastal areas, in comparison with inland regions for a rainy period, while for a dry period, this difference was of 8.7%.

Through this analysis of studies in coastal areas, it is noticeable the lack of studies in Brazil and even in the Tropical zone. Brazil has one of the biggest coastlines in the world and the majority of the presently installed wind farms in the country are situated on the northeast coast, near

the Atlantic Ocean. Furthermore, there are few studies suggesting improvements in wind predictions over coastal regions. These factors foster the importance of this work, that can be turned into a significant tool for the Brazilian wind industry in order to better forecast the wind resources and power production, and may even be a suitable idea to be implemented in other coastal studies. Also, in the future, with the further expansion of wind energy to offshore areas in Brazil, the experience obtained through the study of coastal areas could be used, since wind speeds from sea sectors in coastal areas have similar characteristics to those at offshore platforms (COELINGH et al., 1998).

3.2 Wind predictions with the WRF model

The first official version of the WRF was released in 2004 and since then numerous studies have been carried out on the numerical model, investigating its performance in several sites with different atmospheric characteristics and physical parameterizations. Thus, a review is presented here with relevant and recent studies that address the WRF in terms of its wind forecast errors and sensitivity to physical parameterizations.

Some possible reasons for forecast errors were explored by Carvalho et al. (2014b) in a studied with WRF wind simulations in Portugal. The work evaluated the WRF performance with different boundary and initial conditions from: NCEP-R2 (NCEP-Reanalysis 2), ERA-Interim (European Centre for Medium-Range Weather Forecasts Reanalysis-Interim), NASA-MERRA (National Aeronautics and Space Administration-Modern Era Retrospective-analysis for Research and Applications), NCEP-CFSR (NCEP-Climate Forecast System Reanalysis), NCEP-GFS e NCEP-FNL (NCEP-Final Operational Global Analysis). The simulations were compared with data measured at thirteen meteorological stations in Portugal, with wind measurements at 60 m, except for three stations that measured at 80 m. The WRF-ARW v.3.4.1 simulations used mainly two domains (besides simulations with NCEP-R2, that was configured with 3 domains) 27 vertical levels and grid nudging (FDDA). In addition, the main WRF physical configurations are presented in Table 5.

Two main results were found by Carvalho et al. (2014b). First, it was concluded that initial and boundary conditions provided by reanalysis data may result in different performances of the WRF model, where ERA-Interim, used as input data, presented the simulations with the smallest errors for this study. Second, the simplification of the terrain features by

the model introduces errors in the wind prediction. Overall, in the analysis, the WRF overestimated the wind velocity, a fact that the authors verified to be due to the smoothing and exaggerated simplification of the topography characteristics by the model.

Table 5 – Main WRF parameterizations used by Carvalho et al. (2014b).

Schemes/Area	Portugal
PBL	YSU
SL	MM5 similarity
LS	Noah
MP	WSM6
LWR	RRTM
SWR	Dudhia
CU	KF

Source: Data from Carvalho et al., 2014b.

Regarding the WRF sensitivity to physical parameterizations, the efficiency of the model depends on the area of study, the period of the year evaluated, the roughness and local orography, as well as on the spatial and temporal resolution of the model (GIEBEL et al., 2011; AL-LAMILLOS, 2013). Therefore, WRF numerical simulations are site specific and the parameterization role in its performance was a subject raised in numerous recent works. As presented in Section 2.2.2.1.3, the model has several physical options, which interact with each other in a non-linear and complex way. Hence, in order to identify the best configuration set, it is suggested to perform a sensitivity analysis. This procedure aims to verify the model performance under different combinations of physical parameterizations, allowing the identification of the most suitable configuration and consequently the improvement of wind simulations for the analyzed area (GIANNAROS et al., 2017).

Shing and Hong (2011) compared five planetary boundary layer schemes (Table 7) in the WRF-ARW model (v. 3.2) for one-day simulations (1200 UTC 23 October to 1200 UTC 24 October, 1999), with one parent domain and two nested domains (27, 9 and 3 km of domain resolution). The simulations covered the region of Leon, Kansas, from CASES-99 field program, using NCEP-FNL data ($1^\circ \times 1^\circ$ grid), where the forecasts were compared with local measurements. The simulated thermodynamic surface variables (surface temperature, 2-m temperature and latent and sensible heat fluxes) showed larger differences among the parameterizations used during the daytime and mean values close to the observations; whereas at nighttime, the results obtained were similar for

the five configurations but far from the measurements. On the other hand, for wind simulations (surface friction velocity and 10-m wind speed), the results were more divergent and presented higher Bias, in comparison to the observations at night. In addition, PBL schemes with 1.5 turbulent closure showed better performances than the ones with 1.0 closure type.

Allamillos et al. (2013) sought to evaluate the importance of the terrain representation and the physical parameterization choices in WRF simulations (v. 3.2). In the study, 32 configurations obtained by several combinations of PBL, MP, CU, SWR and LWR (Table 7) were analyzed; as well as different horizontal resolutions with 1 km, 3 km and 9 km of grid distance. The data simulated were compared against local measurements of wind speed and direction at 40 m a.g.l. (4 stations) in Andalusia (Southern Spain), which is a region characterized by varied topography and climate conditions. Through the obtained results, it was shown that the wind prediction is sensitive mainly to the planetary boundary layer parameterization, a result in agreement with other previous studies. The standard deviation (STD) of the simulations with YSU and MYNN PBL schemes exhibited a reduction of up to 6% in the wind speed simulation with the use of the first parameterization. Also, the wind speed Bias showed a significant dependence on the PBL choice, with differences between -15% and 10% in the results.

In terms of wind direction, Allamillos et al. (2013) found that physical parameterizations presented little influence in its estimation, while the terrain representation displayed a greater effect in the simulation of this parameter. In addition, the model's spatial resolution showed a weak influence on STD values and strong influence on the WRF wind speed Bias. Overall, for the four stations, the WRF configurations that showed the best results in the estimation of the wind speed and direction were YSU PBL, Thompson MP, Grell-3D CU, RRTMG SWR, RRTM LWR with 1 km of grid resolution.

Balzarani et al. (2014) applied the WRF model (v. 3.3.1) in the Po Valley (Northern Italy) and in the city of Milan, with a horizontal grid resolution of 5 km and ECMWF analysis as input data (0.5° grid resolution). The study evaluated five PBL schemes (Table 7) in February 2008, in which the model's output was compared with data from meteorological stations. For the 2-m temperature and 10-m wind speed simulation, all five parameterizations showed similar results, with some systematic errors in comparison to the observations. The smaller mean Biases were obtained with UW and ACM2 for the simulations of temperature, 0.2 K and 0.6 K, and wind speed, 0.92 m/s and 0.70 m/s, respectively, in the

city of Milan, which is related to both schemes showing a good performance during the morning and evening. However, at Po Valey, the lowest performances and higher Biases were displayed with UW and MYJ parameterizations in the prediction of 2-m temperature, presenting a Bias equal to 0.9 K for both schemes, and 10-m wind speed, with a Bias of 0.78 m/s and 0.77 m/s, respectively. Both parameterizations were used with Eta SL scheme, which showed greater sensible and latent heat flux values than MM5 SL model.

The wind simulation at a higher height (60 m a.g.l) was evaluated by Carvalho et al. (2012), who tested three different combinations of planetary boundary layer and surface boundary layer schemes (Table 7) in the WRF-ARW model (v. 3.0.1). WRF results were validated against 60-m wind speed and direction measurements collected from three met masts in the months of January (winter) and June (summer) of 2008. The simulations covered an area of Portugal with a parent domain with (90 km of resolution) and two nested domains (18 and 3.6 km of resolution), with NCEP-FNL ($1^\circ \times 1^\circ$ grid) as input data. For the winter month, it was observed an underestimation of the wind speed and a small deviation of the wind direction in all simulations, with YSU-MM5-Noah (PBL-SL-LS schemes) showing the lowest RMSE (3.16 m/s and 47.07°) and Bias (-2.18 m/s and -3.85°) for the wind speed and wind direction predictions.

On the other hand, in the summer month, Carvalho et al. (2012) obtained higher wind speed underestimations by the WRF model, for all simulations, and better wind direction estimations. The higher model performance in the cold season was attributed to the fact that in warm seasons there is a greater influence of small scale atmospheric processes, since large scale processes are weaker. Again, for the wind speed and wind direction predictions, YSU-MM5-Noah displayed the lowest RMSE (3.29 m/s and 39.14°) and Bias (-2.55 m/s and -4.89°). In addition, MYJ scheme was the PBL parameterization that showed higher errors in both months.

Near the tropics, in Northeastern Thailand, Surussavadee (2017) evaluated the WRF wind speed and direction simulations, at 65 m and 90 m a.g.l, employing nine different PBL schemes (Table 7). As affirmed in the study, the climate in the tropical region is predominantly dominated by local and mesoscale circulation, being susceptible to rapid changes due to convection and sea breeze. Thus, accurately simulate the wind in the tropics is a challenge for weather forecasting models.

The study of Surussavadee (2017) covered 3 months (May, August and November of 2012) and measurements of wind speed and wind direction at 65 m from twelve met masts and at 90 m from nine met masts. NCEP-FNL was used for initial and boundary conditions ($1^\circ \times 1^\circ$ grid) in

a simulation domain with 5 km of resolution, nested in a 15-km domain, in the WRF-ARW model (v. 3.7.1). At 65 m, the lowest RMSE for the wind speed prediction was obtained with UW PBL (1.87 m/s) and, at 90 m, GBM PBL showed the lowest RMSE of 1.84 m/s. In terms of wind direction simulation, also UW and GBM showed similar and good performances for both heights. In conclusion, UW-MM5-Noah was the set of PBL-SL-LS schemes that overall exhibited the best performance among all simulations in terms of predicting the wind speed and direction.

In Brazil, Silva and Fisch (2014) investigated the sensitivity of the planetary boundary layer parameterization on the WRF-ARW model (v. 3.2.1) for the wind profile prediction at Alcântara, located on the coast of Maranhão State. The analysis covered two distinct periods, one predominantly dry (September 16-26, 2008) and one predominantly rainy (March 15-25, 2010) and used NCEP-GFS forecasts as input data ($0.5^\circ \times 0.5^\circ$ grid resolution). Four PBL schemes were tested (Table 7) with two nested domains simulation (1-km resolution inner domain), where the predicted data was validated with radiosonde measurements. For the rainy season MYNN2 scheme displayed the best performance; while for the dry period, ACM2 obtained the lowest wind prediction errors. However, no significant change between the results obtained by the four parametrizations was observed. In the same manner, the performance for the rainy and dry season was similar. In addition, overall, the model overestimated the mean wind speed by up to 3 m/s.

Therefore, it is noticeable the influence of planetary boundary layer parameterization on the wind simulation by the WRF model, in which the simulation performance is sensitive to the chosen PBL scheme. However, there is no PBL model that unanimously produces better results, since this parameterization is sensitive to terrain/spatial features and local meteorological conditions (SURUSSAVADEE, 2017).

The interpolation of the WRF results between the simulation grid points, in order to coincide with the measurements location, was not a subject explored in many studies. Sile et al. (2014) compared the WRF wind speed simulation with meteorological observations of 24 stations in Latvia. The analysis evaluated the months of May and November of 2013, where the wind simulated at the nearest grid point to the met mast was compared with the interpolated results at the location of the tower. The WRF-ARW (v. 3.4) was configured with two domains (resolutions of 15 km and 3 km) and main parameterizations presented in Table 6, as well as 0.5° NCEP-GFS data was applied for initial and boundary conditions.

The results showed that the wind predicted at the nearest grid point and interpolated in the mast's location significantly differ in stations located near the coast. On the other hand, at stations located inland, almost no variations were seen between the interpolated values and the ones of the nearest point. This inland result can be explained by the fact that Latvia has a predominantly flat terrain, where there is little wind speed variation and, therefore, the wind simulated shows interpolated values very similar to those of the nearest point. Differently, in coastal areas, there is the occurrence of a horizontal wind speed gradient over the coastline, which is generally not well represented by atmospheric models (SILE et al., 2014).

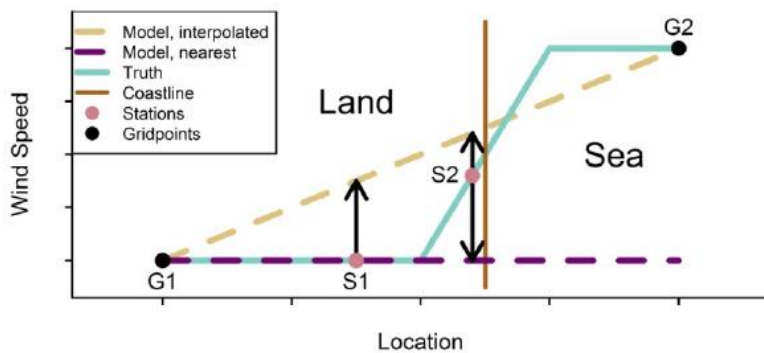
Table 6 – Main WRF parameterizations used by Sile et al. (2014).

Schemes/Area	Latvia
PBL	YSU
SL	-
LS	Noah
MP	WSM5
LWR	RRTM
SWR	Dudhia
CU	KF

Source: Data from Sile et al., 2014.

In Figure 16, presented by Sile et al. (2014), the blue line represents a hypothetical variation of the wind speed between the land and the sea. Considering the station S2, located exactly where the wind speed increases, if the simulated wind speed at S2 is obtained at the grid point G1, the value will be underestimated by the model, while if it is obtained at the grid point G2, it will be overestimated. However, if an interpolation is made between these two grid points (yellow line), a more accurate prediction will be obtained, since the interpolated wind speed is closer to the observed. Otherwise, analyzing the station S1, situated in a region with little spatial wind speed variation, the wind speed simulation at the nearest grid point will provide better results than the interpolated wind speed. Thus, Figure 16 shows a possible explanation for the differences in the wind speed simulated values in coastal areas. Nonetheless, further studies were recommended with the aim to obtain conclusive results about the performance of the WRF interpolated results (SILE et al., 2014).

Figure 16 – Schematic representation of nearest grid point and interpolated wind speeds near the coast.



Source: Sile et al., 2014.

Table 7 – Summary of main parameterizations applied in studies with WRF simulations.

Schemes/ Authors	PBL	SL	LS	MP	LWR	SWR	CU	Location
Shing and Hong (2011)	YSU	MM5	Noah	-	RRTMG	Goddard	-	Leon, Kansas
	ACM2	PX						
	MYJ	Eta						
	QNSE	QNSE						
	Boulac	MM5, PX, Eta, QNSE						
	MYJ	Eta						
	ACM2	PX	PX					
Allamillos et al. (2013)	YSU	-	-	Morisson double- moment	RRTM	Goddard	KF	Andalusia, Southern Spain
	MYNN	-	-	Thomp- son	RRTMG	RRTMG	G3	
Balzarini et al. (2014)	ACM2	MM5	Noah	Morisson double- moment	RRTM	Goddard	G3	Northern Italy
	MRF							
	YSU							
	MYJ	Eta						
	UW							
Carvalho et al. (2012)	YSU	MM5	Noah	WSM6	RRTM	Dudhia	KF	Portugal
	MYJ	Eta						
	ACM2	PX	PX					

Schemes/ Authors	PBL	SL	LS	MP	LWR	SWR	CU	Location
Surussavadee (2017)	YSU	Revised MM5	Noah	WDM6	-	-	-	Northern Thailand
	MYJ	MM5						
	QNSE	QNSE						
	MYNN3	MYNN						
	ACM2	PX	PX					
	Boulac	Revised MM5	Noah					
	UW							
	GBM							
Shin- Hong								
Silva and Fisch (2014)	ACM2	PX	PX	WSM3	RRTM	Dudhia	KF	Maranhão, Brazil
	MYJ	Eta	Noah					
	MYNN2	MYNN						
	YSU	MM5						

3.3 Application of ANN

The conversion of wind speed to wind power is an important and challenging task for the wind industry, as well as being an additional source of uncertainty in the forecast (ARCHER et al., 2014). Due to the accelerated wind energy growth and its intermittent production, concerns have been raised regarding the wind energy integration into the power system. In this context, wind power forecasting methodologies have become important tools to support this integration, since they facilitate the energy balancing between production and consumption in the electrical system (ZHAO et al., 2012).

In addition to the usual classification of wind energy forecasting models, in physical, statistical and hybrid, these can also be classified according to the use or not of NWP data. Models that do not use NWP data are based on historical series of measurements, wind speed and/or generation, to predict the future power output. On the other hand, NWP based models use NWP output as input data to feed statistical, physical, or hybrid models, providing more accurate wind power forecasts (GIORGI et al., 2011; ZHAO et al., 2012; ZHAO et al., 2016).

The integration of neural networks with the results of the WRF mesoscale model, for predicting wind energy, was evaluated by Zhao et al. (2012) in China. The WRF simulations of wind speed, wind direction, pressure, temperature and humidity were applied as input in the ANN to predict the wind energy generation in a Chinese coastal wind farm (Jiangsu), composed of 33 wind turbines (1.5 MW each). The WRF model used as input the GFS data and two approaches were applied to its output data. In the first, the WRF results were used directly in the NN. In the second, the WRF predictions were post-processed before entering the NN, through the application of a Kalman filter to reduce systematic errors. A multi-layer feedforward NN was applied in the study for each individual wind turbine of the park, with the following configurations: three layers, six neurons in the input layer, thirteen neurons in the hidden layer, Levenberg-Marquart training algorithm, hyperbolic tangent sigmoid as the hidden layer activation function and sigmoid as the output layer activation function; while the WRF configurations for this study are presented in Section 3.1.

The training period comprised data from January to December 2009, where post-processed and direct WRF results were provided as input data of the NN, while measured wind power production of each turbine was supplied as output. However, in the prediction period, only WRF

forecasts were used as input to the network, which in turn provided 24-hours wind power predictions, with 15-min time step, for the month of May 2010. The wind power forecast results showed NRMSE values equal to 16.47%, when filtered WRF data, after the Kalman Filter, were used as input of the ANN, and to 17.81%, when unfiltered WRF data were used as input (ZHAO et al., 2012).

Castellani et al. (2016), in order to estimate the energy production of a wind farm in southern Italy, also analyzed the combined use of the WRF model and ANN, where two approaches were tested. The first used WRF output directly as input of an NN to predict the wind power of the farm (ANN wind-power). The second applied WRF results in an NN to improve the wind prediction, which subsequently was used as input to a CFD model to convert wind prediction into wind power (ANN wind-wind + CFD). The wind farm had complex terrain and was divided into two sub-farms for the study, with twelve wind turbines each, totaling an installed power of 15.9 MW. Wind forecasts with the WRF covered a period from September 2015 to March 2016, with GFS as input data, 48-hours forecast horizon, 1-hour time-step and simulations with three nested domains (9, 3, and 1 km).

In the NN input layer, WRF wind speed and wind direction at 10, 100, 200, 300 and 400 m were supplied to the network. Filtered energy production and wind measurements of each turbine, from the SCADA system in 10-minute averages, were used in the ANN wind-power and in the ANN wind-wind approach, where data were divided for training and validation of the NN. In order to reduce systematic errors, the datasets were divided into weeks, one week the network was trained and the following week the network provided forecasts, and so on until the end of the seven months period. The predicted wind power by the two applied methodologies showed similar results, with mean normalized absolute errors of 20% and 16% for the sub-farms (CASTELLANI et al., 2016).

In Brazil, Machado (2014) and Shyu (2015) applied the WRF model and ANN to predict the wind power generation of wind farms located in the Brazilian Northeast. Machado et al. (2014) employed the models at the Pedra do Sal wind farm, composed of twenty wind turbines of 900 kW each. The 72-hour WRF forecasts were used to feed the NN, which provided hourly predictions of the wind farm energy production. Two distinct neural networks were evaluated, differing the number of inputs. One used only the predicted wind velocity at 100 m and the other applied wind speed simulated at five height levels (35, 100, 200, 300 and 500 m). A feedforward neural network, trained with the Levenberg-Marquart backpropagation algorithm, was used with 13 neurons in the hidden

layer, a tangent sigmoid as the hidden layer activation function and a linear transfer function in the output layer. The training comprised the period from September 2, 2013 to December 1, 2014; while the ANN validation covered 30 days, from December 2, 2013 to January 1, 2014 (ten three-days generation forecasts). The NRMSE values of the evaluated networks were 19% for the single input NN and 18% for the multivariate NN, both for 72-hour forecasts with 1-hour time-step.

Shyu (2015) evaluated the combined use of WRF and ANN to predict the wind power generation at Beberibe Wind Farm (BWF), located in Ceará-Brazil, and in PSWF also. The first consists of 32 wind turbines of 800 kW each, while the second has 20 wind turbines of 900 kW each. The 72-hour WRF wind speed predictions were used as input for both networks, which provided 120 wind power forecasts for PSWF and 80 for BWF, both with 10-min time-step. Additionally, both networks were trained with previous 30-day measurements. Two prediction approaches were applied, the model (I) used a neural network for each turbine of each park, while model (II) used only one neural network to predict the generation of the entire park. The feedforward neural networks were configured with 15 input neurons, corresponding to the WRF predictions of temperature, wind velocity and wind direction in five levels (35, 100, 200, 300, 500 m). Also, the NN was trained with the Levenberg-Marquart back-propagation algorithm, used the tangent sigmoid as the hidden layer activation function, a linear transfer function in the output layer and most of the ANN had 5 neurons in the hidden layer. Overall, the NRMSE of the 72 hours wind power forecasts was equal to 18.88% in model (I) and 20.10% in model (II) for BWF, while for PSWF it was 18.61% and 20.17%, respectively.

Therefore, artificial neural networks have been successfully applied in wind power predictions, where the integration of neural networks with numerical weather predictions exhibits a considerable increase in the forecast performance, mainly for long-term predictions (GIORGI et al., 2011). Predictions indicate that in 2020, 57% of the electricity produced in the Brazilian Northeast will come from wind power generation (JONG et al., 2017). This fact allied to the National Electrical System being divided into regional submarkets (ONS, 2017) emphasize the importance of developing accurate tools that can predict the energy produced by the wind power source, in order to increase national and regional energy security. Additionally, accurate wind power forecasts lead to greater reliability in this energy source.

4 MATERIALS AND METHODS

Coastal areas introduce additional challenges to weather forecasting models in predicting wind characteristics due to particularities in the local atmospheric circulation. Therefore, this study was carried out seeking to improve the simulation of the coastal wind at Pedra do Sal wind farm, obtained by the Weather Research and Forecasting model. Firstly, through a sensitivity analysis, the planetary boundary layer scheme that best simulated the wind features at the site was determined. Secondly, a horizontal interpolation approach of the WRF output data was tested with the aim to reduce the wind simulation errors. Thirdly, the application of this approach was also verified for the wind power forecasting, using artificial neural networks. Therefore, in order to perform these analyzes, three databases were used: anemometric and power production experimental data, atmospheric data simulated by the WRF model and wind power data predicted with an ANN.

4.1 Pedra do Sal Wind Farm

The case study covers the area of Pedra do Sal wind farm, which is located at the Northeast region of Brazil, as shown in Figure 17. PSWF (-2.822792° , -1.713890°) is situated in the coastal area of Parnaíba city, Piauí State, in a planar terrain about 400 m distant from the Atlantic Ocean, with an average height of 3 m a.s.l (Figure 18). The wind farm started its commercial operation in December of 2008, with 18 MW of installed capacity and 20 Wobben Enercon E-44 wind turbines (44 m rotor diameter, 55 m hub height and 900 kW nominal power). The annual wind velocity of the region, according to ENGIE (2017), is estimated to be 8.5 m/s at the hub height. More information regarding the wind turbine specifications can be found in Table B.1 of Annex B.

In the Piauí State lies a mountain range called Ibiapaba, with elevated heights, situated nearly 118 km from PSWF, shown in Figure 17. The predominant wind direction at Piauí State is southeast, with some east variation caused by the trade winds (LIRA et al., 2016). However, at the coastline, the wind has a northeast direction and moderate speed. In fact, in almost all Brazilian Northeast coastline, diurnal variations are observed in the wind speed and direction, caused by the overlapping effects of global and mesoscale atmospheric phenomena (BARRETO et al., 2002).

The wind farm is located in the equatorial region, near the equator line, and presents a wind regime mainly influenced by the trade winds and by the Ocean. The proximity to the Ocean causes a sea breeze influence

in the region of PSWF, that contributes to the intensification of the trade winds both in speed and in direction (LIRA et al., 2017). This happens mainly during the dry season, when the sea breeze is strengthened by the greater thermal gradient between land and sea (FISCH, 1999). In addition, the wind in PWSF is also susceptible to other atmospheric systems that act in the region, such as the Intertropical Convergence Zone, easterly wave disturbances, upper tropospheric cyclonic vortices and frontal systems (CAVALCANTI et al., 2009; GISLER et al., 2011).

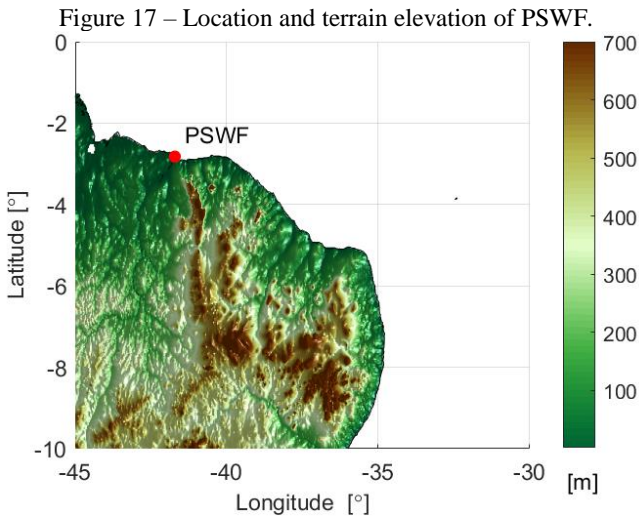
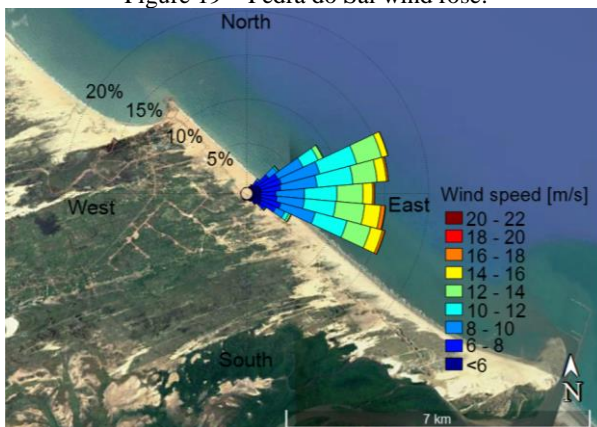


Figure 18 – Photo of PSWF.



As depicted in Pedra do Sal's wind rose of Figure 19, for one-year wind vane measurements at 96 m, the main wind direction is between 65° and 115° . Thus, regarding the wind farm position and its main wind direction, it can be concluded that the wind constantly blows from the sea to the land, which reinforces the strong sea influence in the site (SAKAGAMI et al., 2015).

Figure 19 – Pedra do Sal wind rose.



Source: Google Earth (modified), 2017.

4.2 Experimental Data

At Pedra do Sal wind farm was installed a 100-m anemometric tower with the following installed equipment: a 3D sonic anemometer, four cup anemometers, two wind vanes, two thermo hygrometers, a barometer, GPS and GSM modem. The arrangement of these equipment and its information are depicted in Table 8 and a picture of the tower is presented in Figure 20. Furthermore, the meteorological mast was designed following the recommendations of IEC 61400-12-1: Power Performance Measurements of Electricity Producing Wind Turbines (2005).

The data collection was made by the datalogger CR1000, from Campbell Scientific Instrument Company, which calculates and stores 10-min average data; as well as maximum, minimum and standard deviation of the measurements. The observed data used in this work comprehended averaged wind speed measurements, obtained by the cup anemometer at 98 m, wind direction data, from the wind vane at 96 m, and averaged air temperature data, from the thermo hygrometer at 98 m. Be-

sides the collected data of the meteorological mast, wind generation measurements of each wind turbine were also considered, which were obtained by the software SCADA (Supervisory Control and Data Acquisition), in 10-min intervals.

Table 8 – Information of the equipment installed in PSWF met mast.

Sensors	Height	Company - Model
3D sonic anemometer	100 m	R.M. Young - 81000
Cup anemometer	98 m	Thies – S1110
Thermo hygrometer	98 m	Thies – S52100
Wind Vane	96 m	Thies – S21200
Cup anemometer	80 m	Thies – S1110
Cup anemometer	60 m	Thies – S1110
Wind Vane	58 m	Thies – S21200
Cup anemometer	40 m	Thies – S1110
Thermo hygrometer	40 m	Thies – S52100
Barometer	13 m	Thies – S3100

Figure 20 – PSWF anemometric tower.



After the data collection, the anemometric and power generation databases were submitted to filtering and validation processes, aiming to

diminish inconsistency measurements. Data that exceeded the physical limits of the measuring equipment and data that changed drastically in the 10-min interval were excluded from the databases. More information on the data treatment applied in this work can be found in Fuck (2016).

In the Northeast region, the second semester of the year is characterized by less rain, increase of the solar radiation and higher wind speeds than the first semester, which favors the generation of wind energy (LIRA et al., 2011 apud de MARIA et al., 2006). Thus, as the wind regime at this region is seasonally affect by rainfall and the second half of the year is of greater importance to the wind industry, only data measured during the dry months in PSFW were used, covering the months of September, October, November and December of 2013. In addition, the year of 2013 was characterized as a neutral year, with no occurrence of strong El Niño and La Niña events that could influence the weather of the analyzed region (NOAA, 2015a).

4.3 Simulated data

4.3.1 Atmospheric simulation

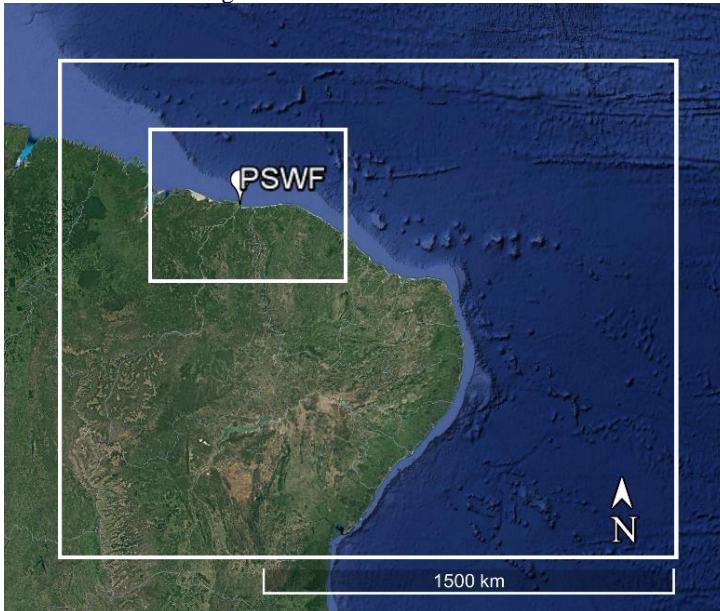
Wind and weather forecasts are usually obtained by computer models that use the same fundamental equations that describe the atmospheric physics. However, there is no defined routine to obtain an accurate forecast, since each prediction depends on the area, the variable to be predicted and the weather elements that influence the site (AGUADO; BURT, 2015). Thus, each forecast has its own peculiarities and the wind predictions obtained in this work are a result of an extensive analysis of different model configurations, with the aim to obtain the best wind speed forecast for the studied coastal wind farm.

The numerical weather prediction software used in this study was the mesoscale Weather Research and Forecasting Model with the ARW dynamic solver, version 3.6.1. The simulations covered Pedra do Sal wind farm with two domains, a parent domain centered at the Northeast area of Brazil and a child domain centered at the wind farm, in a two-way nesting, as shown in Figure 21. The outer domain was configured with a horizontal resolution of 15 km, while the inner domain with 5 km, and both with 27 vertical levels. Due to computational stability, WRF's manual advises a time step value (in seconds) of maximum six times the grid distance (in kilometers) (SKAMAROCK, et al., 2008). Therefore, for the first and second domain the time steps were 90 s and 30 s, respectively. Also, in order to allow comparisons at the same height of the simulated

data with the measurements, a linear vertical interpolation approach in the WRF output data was applied.

The mesoscale model computes the mean values of the atmospheric physical variables for specific points in each grid cell of the simulation domain. The component velocity u is evaluated in the center of the right and left grid faces, whereas the component velocity v is evaluated in the center of the upper and lower grid faces, while mass, thermodynamic, scalar and chemistry variables are evaluated in the center of the grid cell, according to Arakawa staggered C-grid. In a case study, these grid points usually do not coincide with the exact location of the measurements and, thus, a horizontal interpolation of the WRF results is generally made to extrapolate the simulated data to a desired location. In a coastal area, a small change in the interpolation point of the model's output can place this location more onshore or more offshore, which can result in a large difference in the predicted wind. Therefore, in order to analyze the variations that the interpolation location may result in the simulated data, it was investigated the onshore and offshore horizontal interpolation of the wind simulated by the WRF model at the area of PSWF.

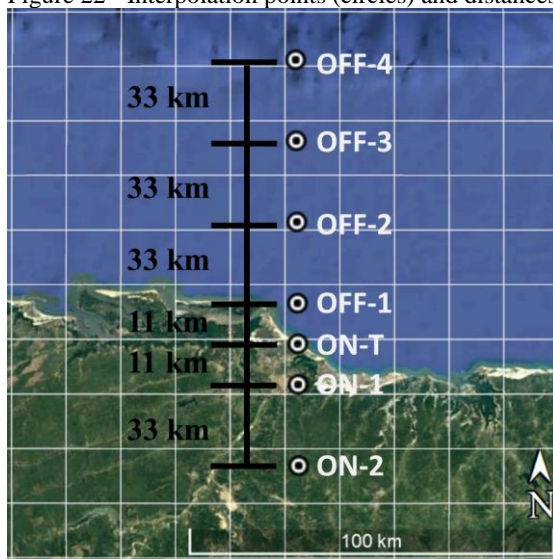
Figure 21 – Simulation domains.



Source: Google Earth (modified), 2017.

WRF output data obtained with the one domain simulation, with 15 km of horizontal resolution, were linearly interpolated in different locations along the north-south direction, crossing the shoreline and the wind farm, as shown in Figure 22 with the domain grid lines. Additionally, the coordinates of each interpolation location are presented in Table 9. The study analyzed four offshore points (OFF-1, OFF-2, OFF-3 and OFF-4), the anemometric tower's location (ON-T) and two more onshore points (ON-1 and ON-2). The analysis covered a higher number of offshore points due to the predominance of winds that come from the sea at the site.

Figure 22 - Interpolation points (circles) and distances.



Source: Google Earth (modified), 2017.

Table 9 – Geographical coordinates of the interpolation locations.

Points	Latitude (°)	Longitude (°)
OFF-4	-2.122792	-41.713890
OFF-3	-2.322792	-41.713890
OFF-2	-2.522792	-41.713890
OFF-1	-2.722792	-41.713890
ON-T	-2.822792	-41.713890
ON-1	-2.922792	-41.713890
ON-2	-3.122792	-41.713890

The main parameterization schemes used in this study were: MYNN2 for the planetary boundary layer parameterization, MYNN surface layer scheme, Unified Noah land surface, RRTM and Dudhia for the long-wave and short-wave parameterizations, WRF Double-Moment 5-class micro physics scheme and Kain-Fritsch cumulus physics scheme. However, for the sensitivity analysis of the planetary boundary layer scheme, other PBL-SL parameterizations were used: ACM2-MM5, Bou-lac-MM5, MYJ-Eta, UW-MM5 and YSU-MM5, as presented in the Results Section, in the next chapter.

The simulations covered the months of September, October, November and December of 2013, and were initialized at 0000 local time (LT) with a forecast horizon of 5 days (120 hours) plus 15 hours, that were discarded as spin-up time of the model. There is not a consensus of the ideal models' spin-up time (KLECZEK, 2014). Nevertheless, in this work, the warming up period was chosen according to the model's instructions and was confirmed by a sensitivity analysis. Thus, the fifteen excluded hours represent the 12 hours of spin-up time recommended by the model plus 3 hours of local time conversion from UTC. Furthermore, the predictions were obtained in 10 min intervals, which were later reduced by 30 min means.

Initial and boundary conditions were obtained by two different sources. First, the Reanalysis II from the National Centers for Environmental Prediction (NCEP-R2) was used to best adequate the model to the local characteristics of the site, since this is a prediction data that is corrected by measured data assimilation (NCEP, 2000). The chosen NCEP-R2 data has $2.5^{\circ} \times 2.5^{\circ}$ of spatial resolution, 6 hours of temporal resolution and were initialized at 1200 UTC. Secondly, for the wind prediction applied as input in the ANN, data was acquired from the Global Forecast System, also made by NCEP (NCEP, 2007). GFS provides daily forecast with a $0.5^{\circ} \times 0.5^{\circ}$ spatial resolution, 3 hours of temporal resolution and were initialized at 1200 UTC.

Regarding information about the terrain, the USGS (United States Geological Survey) topo data was used in the simulations, with a horizontal resolution of 2 minutes arc. In addition, sea surface temperature (SST) values, from the Optimum Interpolation Sea Surface Temperature (OISST) of the National Centers for Environmental Information (NOAA), were also inserted as input data in the WRF simulations, mainly due to the site's proximity to the Ocean. This data is weekly produced and has a spatial resolution grid of $1^{\circ} \times 1^{\circ}$ (NOAA, 2015b).

4.3.2 Wind power simulation

The wind power simulation was applied in this study with the aim to verify the performance of the interpolation approach in terms of wind power prediction, since this is a vital information for the wind industry. Wind power predictions were obtained through the application of an artificial neural network from the MATLAB software, that used as input data atmospheric and wind predictions acquired through the WRF model. On the other hand, data from the WRF model were obtained through a downscaling process of global weather predictions of the GFS, by including information of the local features, such as terrain height, land use and surface roughness. The flow chart for the wind power prediction obtained in this study is shown in Figure 23.

Prior to obtaining the wind power forecasting data, the ANN must go through a learning process with the purpose of adjusting the model. In this first stage, weather forecast information obtained by the WRF model was provided to the network, as well as information of the total power production measured in the wind farm. After the learning process, the ANN is capable of providing wind power predictions. For this stage, input data from the WRF simulations was supplied to the network and, in turn, the network provided the wind power forecast as output.

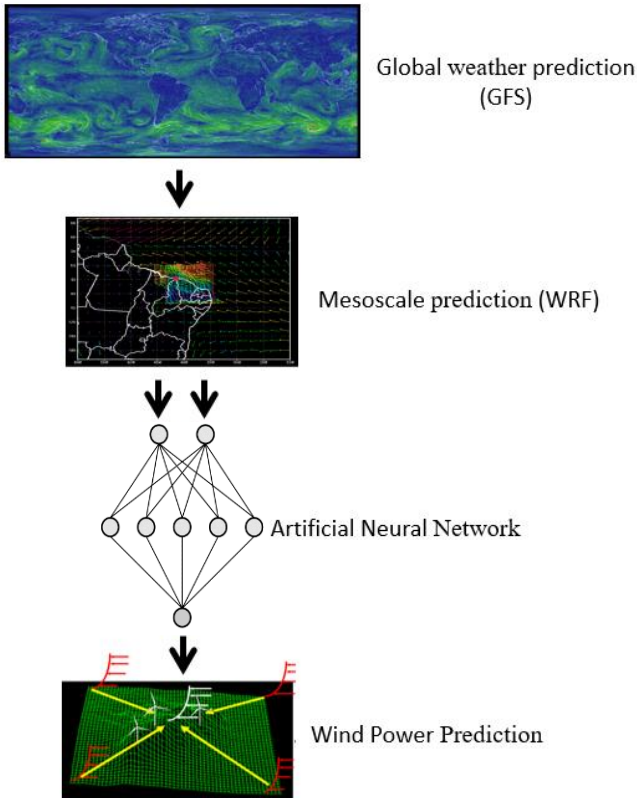
A multilayer feedforward artificial neural network was used in this study, with one input layer, one hidden layer and one output layer. The ANN was based on two previous works carried out in the same wind farm (MACHADO, 2014; SHYU, 2015), which had nine neurons in the input layer and one neuron in the output layer. The number of neurons in the input layer is equivalent to the data quantity supplied to the network, which were: wind speed at five heights (40, 60, 80, 98 and 200 m), wind direction at 60 m, air temperature, pressure and humidity (30 min averages).

There is no unanimity about the number of neurons and hidden layers in a neural network, since they depend on the type of data used, the activation function applied in the neurons and the training algorithm (KARSOLIYA, 2012). Nonetheless, it is affirmed that one hidden layer is enough to obtain good results through the neural network, as long as it contains an adequate number of neurons, which must be estimated by trial and error (CATALÃO, 2011; ZHAO e t al., 2012). Therefore, different number of neurons in the hidden layer were tested through a sensitivity analysis (1, 5, 10, 15, 20, 30, 40, 50, 60, 70, 80, 90 and 100 neurons). Regarding the network training, the backpropagation technique was applied with the Levenberg-Marquart algorithm, as well as two activation

functions were used, the tangent sigmoid in the hidden layer and the linear transfer function in the output layer.

Initially, for the training process, the network received the WRF's forecasted data of the first thirty days of the analyzed period, as well as the measured wind power production of the 20 wind turbines at PSWF. After this stage, the next five days of the WRF simulated data were used as input in the network, in order to obtain the wind power prediction for the same five days. In total, 25 cycles of thirty days of training and five days of prediction were performed, in 30-min intervals, which are presented in Table 10, covering a period from 2013/09/01 to 2014/01/02. Two extra days from January 2014 were added in this analysis with the aim to complete the last five days cycle of the prediction process.

Figure 23 – Wind power prediction flowchart.



Source: Beccario (modified), 2018.

Table 10 – Wind power forecasting cycles.

Cycles	Training		Forecasting	
	start	end	start	end
1	2013/08/01	2013/08/30	2013/08/31	2013/09/04
2	2013/08/06	2013/09/04	2013/09/05	2013/09/09
3	2013/08/11	2013/09/09	2013/09/10	2013/09/14
4	2013/08/16	2013/09/14	2013/09/15	2013/09/19
5	2013/08/21	2013/09/19	2013/09/20	2013/09/24
6	2013/08/26	2013/09/24	2013/09/25	2013/09/29
7	2013/08/31	2013/09/29	2013/09/30	2013/10/04
8	2013/09/05	2013/10/04	2013/10/05	2013/10/09
9	2013/09/10	2013/10/09	2013/10/10	2013/10/14
10	2013/09/15	2013/10/14	2013/10/15	2013/10/19
11	2013/09/20	2013/10/19	2013/10/20	2013/10/24
12	2013/09/25	2013/10/24	2013/10/25	2013/10/29
13	2013/09/30	2013/10/29	2013/10/30	2013/10/03
14	2013/10/05	2013/11/03	2013/11/04	2013/11/08
15	2013/10/10	2013/11/08	2013/11/09	2013/11/13
16	2013/10/15	2013/11/13	2013/11/14	2013/11/18
17	2013/10/20	2013/11/18	2013/11/19	2013/11/23
18	2013/10/25	2013/11/23	2013/11/24	2013/11/28
19	2013/10/30	2013/11/28	2013/11/29	2013/12/03
20	2013/11/04	2013/12/03	2013/12/04	2013/12/08
21	2013/11/09	2013/12/08	2013/12/09	2013/12/13
22	2013/11/14	2013/12/13	2013/12/14	2013/12/18
23	2013/11/19	2013/12/18	2013/12/19	2013/12/23
24	2013/11/24	2013/12/23	2013/12/24	2013/12/28
25	2013/11/29	2013/12/28	2013/12/29	2014/01/02

4.4 Forecast Verification

The accuracy of the prediction data can be analyzed by statistical methods in a process called forecast verification. This process allows a quantitative performance evaluation of the forecast model through the comparison between predicted and observed variables (WARNER, 2011). Several performance metrics have been used in the literature to evaluate wind and atmospheric forecasting and the present work sought to employ the most used ones to facilitate comparisons with published works. Thus, the following statistical metrics were used: Bias, Root Mean Square Error (RMSE) and Pearson's coefficient. Additionally, in order to compare forecast errors in wind power generation for different wind farms, it is recommended to normalize the average errors. This normali-

zation should be done with the installed power capacity of the farm, instead of the mean production, since the first is an easier information to obtain (GIEBEL et al., 2011).

The forecast error θ'_i is obtained by the difference between the predicted value at an instant i (θ_i^p) and the observed value at the same instant i (θ_i^{obs}),

$$\theta'_i = \theta_i^p - \theta_i^{obs}. \quad (4.1)$$

However, for the wind direction, which is not a linear variable, when the deviation between the predicted and the observed value exceeds 180° , the forecast error assumes the following equation (FERREIRA et al., 2008):

$$\theta'_i = \theta_i^p - \theta_i^{obs} \left[\frac{1-360}{|\theta_i^p - \theta_i^{obs}|} \right], \text{ if } |\theta_i^p - \theta_i^{obs}| > 180^\circ. \quad (4.2)$$

The Bias calculation quantifies the systematic error of a forecast. If the Bias assumes positive values, it means that the forecast overestimates the measurement; while if a negative value is presented, the forecast underestimates the measurement. Additionally, for the wind direction, a positive (negative) Bias represents a clockwise (anti-clockwise) deviation (CARVALHO et al., 2012). Its calculation is performed by the following equation:

$$Bias = \frac{1}{N} \sum_{i=1}^N \theta'_i, \quad (4.3)$$

where θ'_i is the forecast error at an instant i and N is the total number of instants i considered.

The root mean square error allows to evaluate the overall efficiency of the forecast, in which the closer to zero, the better is the forecast. This error is expressed by:

$$RMSE = \left[\frac{1}{N} \sum_{i=1}^N (\theta'_i)^2 \right]^{\frac{1}{2}}, \quad (4.4)$$

where θ'_i is the forecast error at an instant i and N is the total number of instants i considered.

The normalization of this parameter is the normalized mean square error (NRMSE), which is usually used to evaluate errors in the wind power generation prediction. The NMRSE can be calculated by:

$$NRMSE = \frac{RMSE}{C}, \quad (4.5)$$

where C is installed power capacity of the farm.

Additionally, in order to evaluate the linear correlation between the predicted and observed data, the correlation coefficient r , or the Pearson's coefficient, was used, that varies from +1 to -1. If the correlation coefficient assumes the +1 value, it means that there is a perfect linear positive correlation between the analyzed data. On the other hand, if the correlation coefficient assumes the -1 value, it represents a perfect linear negative correlation. This coefficient is represented by:

$$r = \frac{Cov(\theta^p, \theta^{obs})}{\sigma_{\theta^p} \sigma_{\theta^{obs}}}, \quad (4.6)$$

$$Cov(\theta^p, \theta^{obs}) = \frac{\sum_{i=1}^N (\theta_i^p - \bar{\theta}^p)(\theta_i^{obs} - \bar{\theta}^{obs})}{N}, \quad (4.7)$$

$$\sigma_{\theta^p} = \frac{\sqrt{\sum_{i=1}^N (\theta_i^p - \bar{\theta}^p)^2}}{N}, \quad (4.8)$$

$$\sigma_{\theta^{obs}} = \frac{\sqrt{\sum_{i=1}^N (\theta_i^{obs} - \bar{\theta}^{obs})^2}}{N}, \quad (4.9)$$

where $Cov(\theta^p, \theta^{obs})$ is the covariance between the predicted and observed data, σ_{θ^p} and $\sigma_{\theta^{obs}}$ are the standard deviation of the predicted and observed dataset, respectively.

5 RESULTS

The presentation of the results is divided into three parts, as described ahead. The first covered a sensitivity test, which consists of an analysis of how the variation of one parameter may affect the results obtained in the model. In this part, a planetary boundary layer sensitivity test was made in order to verify the configuration set that best represent the atmospheric conditions at Pedra do Sal wind farm. The second part proposed a horizontal interpolation approach of the WRF results obtained, aiming to improve the wind simulation at the site. Finally, the third part tested the performance of this approach applied in the wind power forecasting with the use of an ANN.

5.1 Sensitivity test

Sensitivity tests were made with the aim to obtain a model configuration that provides outputs similar to the atmospheric features observed at PSWF during the analyzed period. The sensitivity test presented here consists of verifying the most adequate planetary boundary layer scheme of WRF for the coastal site during dry months.

As the simulated data provided by the WRF model are obtained through calculations in specific points within the grid cell, a horizontal and vertical interpolation of the WRF forecasts was done to enable the comparison with measured data. At the horizontal direction, a linear interpolation to the meteorological tower position was made with the simulations obtained at the nearest grid points. Furthermore, at the vertical direction, a linear interpolation to the height of the highest cup anemometer in the tower (98 m) was done with the results at the nearest sigma levels.

5.1.1 Boundary layer schemes

The boundary layer parameterizations of the WRF model are divided into surface layer, land surface and planetary boundary layer schemes. The first is responsible for calculating the friction velocities and the exchange coefficients near the ground, that allow the second to calculate moisture and heat fluxes over land, in multiple layers of soil, and the third to compute the turbulent flux at the vertical atmospheric column of the model (SKAMAROCK et al., 2008; CARVALHO, 2009).

The sensitivity test regarding the boundary layer schemes focused on the planetary boundary layer parameterization, since this is a parameter of high influence in the model performance when predicting wind in

the PBL (CARVALHO et al., 2012). Additionally, the PBL in coastal regions diverges from the well-known neutral and well-mixed conditions, due to advective transport processes (ARCHER et al., 2014). Thus, improvements in the PBL parameterizations are necessary to better predict the wind over coastal areas. Therefore, the aim of this first result is to analyze some existing planetary boundary layer schemes in the WRF model at Pedra do Sal wind farm, located 400 m from the sea.

As there is a strong interaction between the boundary layer parameterizations, there are some fixed combinations among them, imposed by the model. According to the model's limitations and previous studies, six simulations (S-1, S-2, S-3, S-4, S-5 and S-6) were performed using different physical configurations for the planetary boundary layer, surface layer and land surface; which are presented in Table 11. The other parameterizations' schemes available in the WRF were kept the same for all six simulations: RRTM and Dudhia for the long-wave and short-wave parameterizations, WRF Double-Moment 5-class micro physics scheme and Kain-Fritsch cumulus physics scheme. These results were obtained with one domain WRF simulations of 15 km horizontal resolution for the month of September/2013.

Table 11 – Boundary layer physical parameterizations of the simulations.

	PBL	Surface layer	Land surface
S-1	ACM2	MM5 Similarity	Unified Noah
S-2	BouLac	MM5 Similarity	Unified Noah
S-3	MYJ	Eta Similarity	Unified Noah
S-4	MYNN2	MYNN	Unified Noah
S-5	UW	MM5 Similarity	Unified Noah
S-6	YSU	MM5 Similarity	Unified Noah

5.1.2 Wind speed simulations

The time series of the observed and simulated wind speeds are depicted in Figure 24 for different configurations of boundary layer schemes. Overall, during the simulated 720 hours, encompassing five-days cycles, it is noted that all six simulations of the wind speed by the WRF model are consistently underestimating the measured values of the 98 m cup anemometer in PSFW. The S-4 configuration (purple line), with MYNN2 PBL scheme, is the simulation that seems to present the closest wind speed curve to the observed curve (black line).

The mean observed wind velocity on September/2013 was 12.16 m/s at 98 m in PSFW. Among all simulated configurations, S-1 was the

one that, on average, most underpredicted the wind speed, in about 23.8%; while S-4 showed the lowest underestimation of the monthly mean wind velocity, which was of 11.3%, as shown in Table 12. In terms of the statistical metrics, comparing S-1 with S-4, the latter presented a RMSE almost 32.5% lower than the first and a decrease in the Bias of about 53%, which highlights the importance of sensitivity analysis for the reduction of the forecast errors. In addition, the S-6 simulation was the setup with the second the best results (2.95 m/s RMSE and -2.67 m/s Bias); whereas S-2, S-3 and S-5 showed similar mean error values, with RMSE equal to 3.05, 2.98 and 3.07 m/s and Bias of -2.83, -2.65 and -2.77 m/s, respectively.

Figure 24 – Wind speed time series at 98 m for observed and simulated data with different boundary layer schemes.

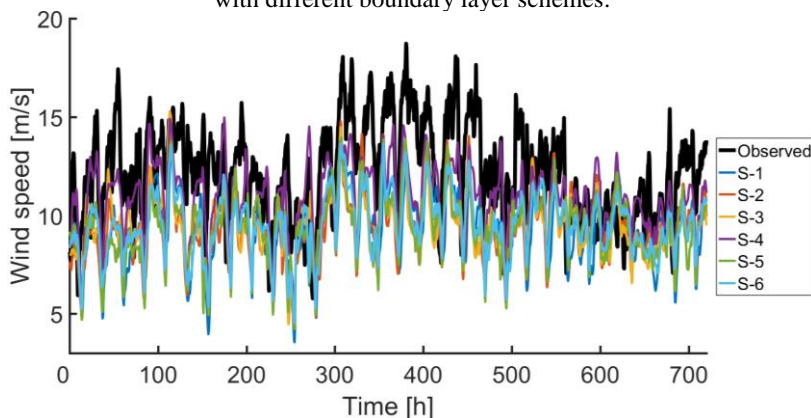


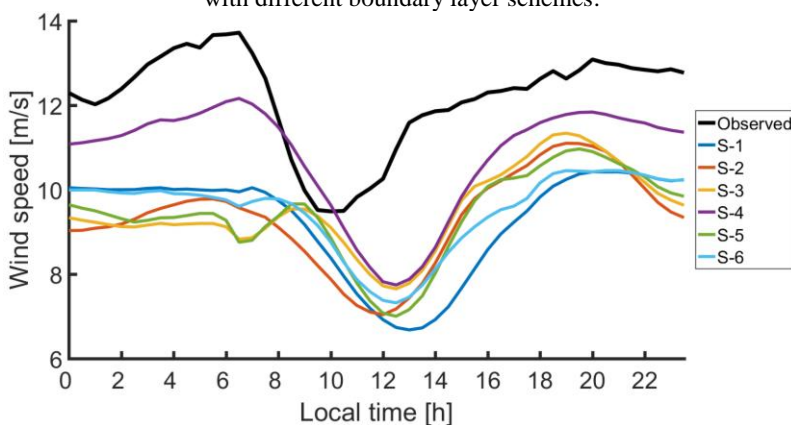
Table 12 – Statistical metrics for the wind speed simulations (RMSE and Bias) and predicted average wind velocities (Vel.).

Simulations	RMSE [m/s]	Bias [m/s]	Vel. [m/s]
S-1	3.14	-2.89	9.27
S-2	3.05	-2.83	9.33
S-3	2.98	-2.65	9.51
S-4	2.12	-1.37	10.79
S-5	3.07	-2.77	9.39
S-6	2.95	-2.67	9.50

Regarding the representation of the wind speed diurnal cycle at 98 m (Figure 25), it is shown that, in general, the WRF model underestimates

the wind speed throughout the whole day and for all simulations. Furthermore, for the six physical configurations tested, a delay is observed in the simulation of the day minimum wind speed velocity, which happened around 10 a.m. LT. Through a behavior analysis of the curves, it can be noted that S-4 and S-1 simulations are those that present a diurnal wind speed cycle more similar to the one observed in Pedra do Sal, with the first presenting better results.

Figure 25 – Wind speed diurnal cycle at 98 m for observed and simulated data with different boundary layer schemes.



5.1.3 Weibull simulations

The Weibull Probability Density Function (PDF) for the six simulations with different PBL schemes is plotted against the observed Weibull PDF in Figure 26. Analyzing the wind speed axis (x), there is a shift to the left side in all simulated PDFs, when compared to the measured PDF. This represents that the WRF model simulates a higher frequency of lower wind speeds than the ones measured in PSWF, regardless of the PBL parameterization used. Likewise, there is a frequency underestimation of strong winds by the model, which, overall, causes an underestimation tendency of the wind speed, as seen in the previous results.

In Table 13, the Weibull scale (A) and shape (k) parameters are presented along with the most probable wind speed (Vel_{prob}) for the six simulations and for the observed data (Obs.) at PSWF. The lowest deviation from the measured PDF scale parameter was obtained in simulation S-4 (12.19%), while for the shape parameter, the simulation S-2 showed almost no deviation. In terms of the most probable wind speed, the highest

frequency wind speed during the month of September 2013, S-4 was again the simulation with the lowest deviation (11.03%). Additionally, from S-1 to S-3 and S-5 to S-6, a similar value of Vel_{prob} was observed, around 9.80 m/s. This means that although all simulated PDFs are located to the left of the measured PDF, S-4 curve is the closest to the measured.

Figure 26 – Weibull probability density function for observed and simulated data with different boundary layer schemes.

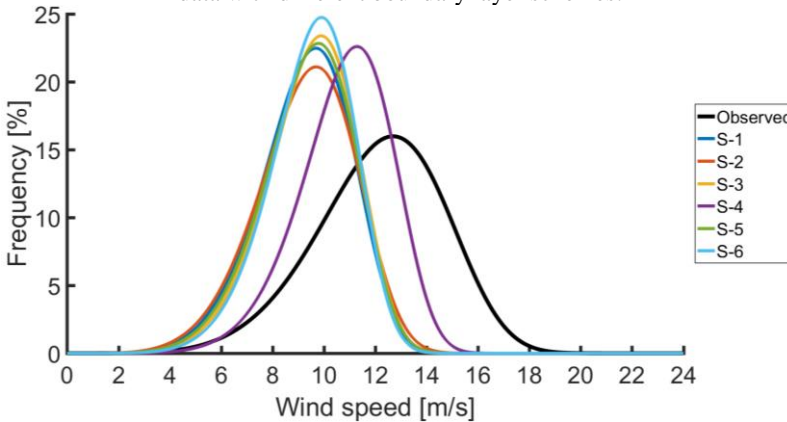


Table 13 – Weibull parameters and most probable wind speed for simulated and observed Weibull PDFs.

Data	A [m/s]	k	Vel_{prob} [m/s]
S-1	9.99	6.01	9.69
S-2	10.04	5.66	9.70
S-3	10.16	6.38	9.89
S-4	11.54	7.01	11.29
S-5	10.08	6.17	9.79
S-6	10.15	6.75	9.91
Obs.	13.13	5.61	12.69

5.1.4 Wind direction simulations

The wind direction time series simulated with the six physical configurations are presented in Figure 27, together with the wind direction measured at PSWF. According to Figure 27, it is not possible to observe a great distinction between the six different simulations, where all of them were able to predict with a certain accuracy the direction of the local wind. However, the simulated wind directions presented smoother curves compared to the observed curve.

Figure 27 – Wind direction time series for observed and simulated data with different boundary layer schemes.

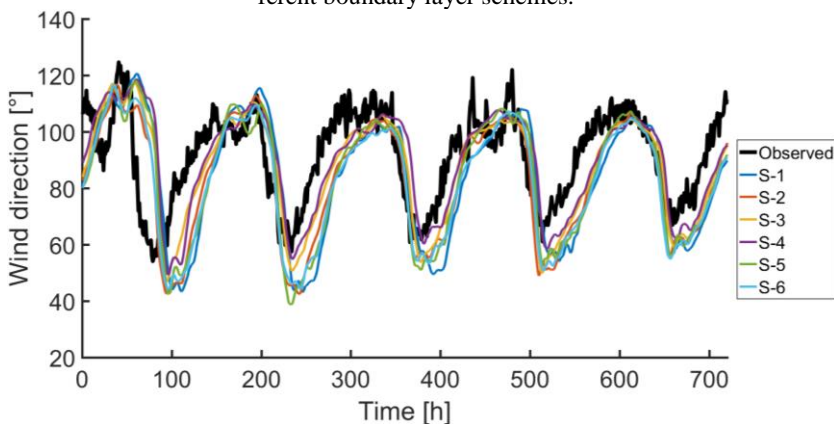


Table 14 presents the statistical metrics (RMSE and Bias) of the wind direction simulations, calculated with the wind direction measured at 96 m a.g.l. in the anemometric tower. Despite the graphical similarity of the simulated wind direction curves, there is a small difference of up to 4.5° in RMSE and 5.0° in Bias between the simulations with the highest and the lowest errors. The lowest values of RMSE and Bias were presented by the S-4 simulation, with 12.21° and -3.04° , respectively; while the highest RMSE was observed in the S-1 simulation (16.69°) and the highest Bias, in the S-6 (-8.03°). Furthermore, all simulations exhibited a counterclockwise deviation in the characterization of the wind direction at PSWF, represented by the negative Bias.

Table 14 - Statistical metrics for the wind direction simulations.

Simulations	RMSE [°]	Bias [°]
S-1	16.69	-6.42
S-2	13.98	-6.80
S-3	12.92	-4.79
S-4	12.21	-3.04
S-5	15.19	-6.62
S-6	14.90	-8.03

5.1.5 Conclusions

For the studied period, S-4 (MYNN2-NYNN-Noah) was the set of boundary layer parameterizations that provided the best results for wind

speed simulations at PSWF, as well as showing the closest Weibull PDF to the measured function. The wind speed simulation errors obtained by the MYNN2-MYNN-Noah schemes were equal to 2.12 m/s of RMSE and -1.37 m/s of Bias, for a forecast horizon of 120 hours (30 min means). This result is in agreement with other studies that successfully applied the MYNN2 PBL parameterization in wind simulations at Northeast Brazil (SILVA; FISCH, 2014; PINTO, 2017; SANTOS et al., 2018).

The six configurations tested have underestimated the measured wind speed at 98 m. Also, in the representation of the diurnal wind speed cycle, all simulations exhibited a delay in the representation of the day minimum velocity, of about 2 hours on average.

Regarding the wind direction prediction, all combinations of parameterizations showed similar performance, as well as smoother curves, when comparing to the observed data. Again, S-4 simulation presented the smallest errors, 12.21° of RMSE and -3.04° of Bias. Thus, the chosen WRF parameterizations applied in the next analysis were: MYNN2 as the planetary boundary layer scheme, MYNN for the surface layer parameterization and Unified Noah as the land surface scheme.

5.2 Horizontal interpolation approach

In this section, it is investigated the onshore and offshore interpolation of the atmospheric conditions simulated by the WRF model, mainly the wind features and the air temperature. The obtained WRF simulations covered the area of Pedra do Sal wind farm and the month of September of 2013; first with a one domain simulation (15 km of horizontal resolution) and later adding a nested domain to the simulation (5 km of horizontal resolution). In addition, the model was configured with the parameterizations described in the Methodology Section, adjusted through the sensitivity analysis.

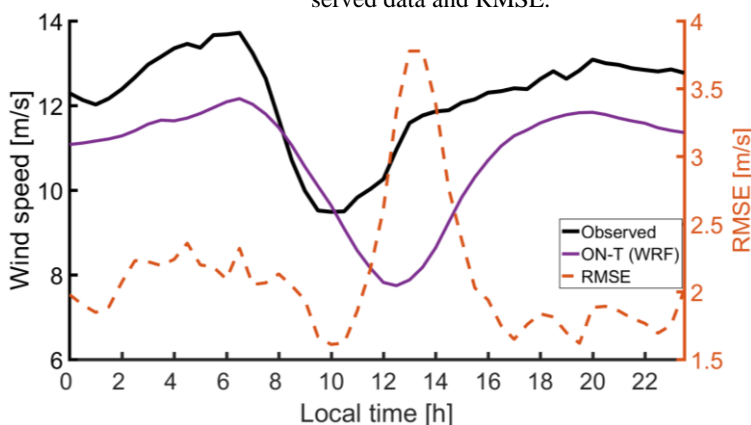
The WRF results were compared with wind speed measurements of the met mast's cup anemometer at 98 m, wind direction of the wind vane at 96 m and air temperature of the thermo hygrometer at 40 m a.g.l., where a linear vertical interpolation was applied in the WRF output of the nearest sigma levels. Regarding the horizontal interpolation, only the one domain simulated data were interpolated in seven different locations (Figure 22 and Table 9). The one domain analysis evaluated four offshore interpolation locations, named OFF-1, OFF-2, OFF-3 and OFF-4, the location of the anemometric tower (ON-T) and two more onshore locations, named ON-1 and ON-2. The nested domain data were interpolated only

in the position of the meteorological mast (ON-T-2D) and were used to investigate the performance of the interpolation approach.

5.2.1 WRF wind speed simulation

The wind speed simulation obtained by interpolating the one-domain WRF results (15 km) in the met mast position (ON-T) is depicted in Figure 28, along with the observed wind speed at 98 m. The two curves are presented as diurnal cycle; likewise, the 30-min error of the simulated wind speed, in terms of RMSE, is also shown. According to Figure 28, the WRF model can reproduce with certain accuracy the mean diurnal cycle of the wind speed at PSWF. However, two main differences between the simulated and observed curve are noticed.

Figure 28 – Wind speed diurnal cycle at 98 m for WRF simulation (ON-T), observed data and RMSE.



First, the simulated wind speed interpolated in the tower's location (ON-T) underestimates the measured velocity. The monthly mean wind speed at PSWF is 12.16 m/s for the analyzed month. However, the average ON-T simulated speed was 10.79 m/s for the same period, which represents an underprediction of the wind speed of 11.3% by the model. Additionally, this underprediction is not constant during the day, in which the simulated and observed curves of Figure 28 show a larger difference between 12 h to 15 h LT, where the ON-T velocity is, on average, 24.7% lower than the observed for this period.

Second, the WRF results show a delay in the simulation of the day minimum velocity. The measured mean diurnal wind speed cycle shows

higher velocities in the early morning and at night, as well as a reduction of the wind speed between 07 h to 13 h LT, with a minimum speed peak near 10 a.m. It is noted that the model can predict the speed decay through the day, and a later recovery at night. Nevertheless, this simulated deceleration is delayed in about two hours by the model. This causes a peak in the RMSE curve, with a maximum value of 3.78 m/s around 13 h LT.

Giebel et al. (2011) state that there are two types of errors in weather forecasting: the level error and the phase error. Taking a storm as an example, the level error makes the simulation fail to predict the severity of the storm, while the phase error causes a misprediction of the time of the storm greater intensity. In this way, by analyzing Figure 28, both errors can be observed in the simulation of the wind speed by the WRF model. The model misrepresents the smallest wind velocity during the day (level error) and the time that it happens (phase error).

5.2.2 WRF interpolations with one domain

The WRF simulations with one domain, centered at the Northeast region of Brazil, were interpolated in seven different locations and compared to the wind speed diurnal cycle of the measured data. As displayed in Figure 29, the WRF result obtained by the offshore interpolation OFF-2 showed a simulated wind speed curve closer to the observed velocity, in comparison with the other interpolation locations.

Looking only at the onshore interpolations (ON-T, ON-1 and ON-2), graphically it is shown that the more onshore the interpolation point is located, the greater is the underestimation and the delay between the observed and simulated wind velocities. Analyzing the wind speed statistical metrics of these points in Table 15, it is highlighted that the Bias increases as the interpolation point moves to a more onshore location, going from -1.37 m/s at ON-T to -2.52 m/s at ON-2. In the same manner, the RMSE also displays higher values on the location ON-2 (3.25 m/s) than in the position ON-T (2.12 m/s).

On the other hand, looking only at the offshore interpolations (OFF-1, OFF-2, OFF-3 and OFF-4), there is not a visible increase on the delay between the offshore curves and the observed wind speed, which results in similar RMSE values for the four locations. The maximum RMSE was observed in the point OFF-1 with 1.79 m/s, while the minimum was in OFF-2 with 1.69 m/s.

In terms of the Bias, the results obtained in the first two offshore points behave differently from those acquired in the last two. OFF-1 and OFF-2 displayed negative Bias values (-0.67 and -0.10), which means that

their wind speed simulations underestimated the observed velocity. On the other hand, the Bias at OFF-3 and OFF-4 were positive (0.12 and 0.17), thus, the wind speed interpolated in these locations was overestimated by the model, in comparison to the observed velocity.

In conclusion, regarding the wind speed curves and the statistical metrics, the WRF results interpolated in the location OFF-2 obtained the lowest RMSE (1.69 m/s) and Bias (-0.10 m/s) between all the analyzed points. An improvement in the wind speed simulated by the WRF model is observed when interpolated at the location OFF-2 in comparison with the result obtained at the tower's position (ON-T), which is a common interpolation point. This improvement in the simulation resulted in a reduction of 20.2% of the RMSE and 92.7% of the Bias.

Figure 29 – Wind speed diurnal cycle at 98 m for the observed data and WRF results in different interpolation points.

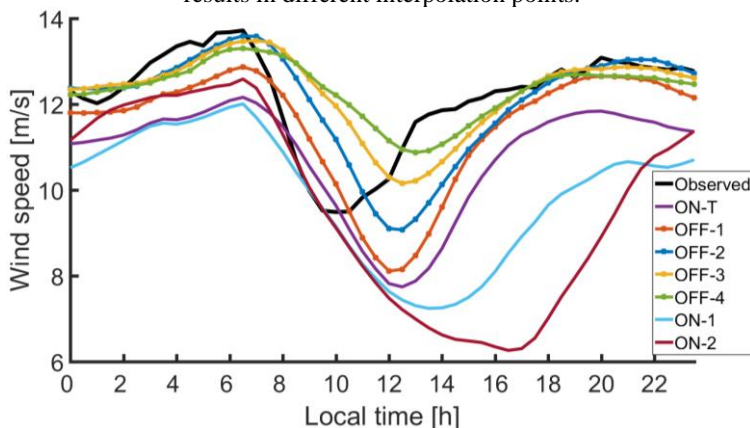


Table 15 – Wind speed statistical metrics for the onshore and offshore interpolations.

Points	RMSE [m/s]	Bias [m/s]
ON-T	2.12	-1.37
OFF-1	1.79	-0.67
OFF-2	1.69	-0.10
OFF-3	1.70	0.12
OFF-4	1.74	0.17
ON-1	2.80	-2.25
ON-2	3.25	-2.52

Additionally, recalling the level and phase errors defined by Giebel et al. (2011), the phase error was still present in the results obtained at OFF-2. However, there was a decrease in the level error. The smallest wind velocity during the day was 9.07 m/s at OFF-2, 7.74 m/s at ON-T and 9.49 m/s for the measurements. Therefore, the WRF results interpolated in the location OFF-2 misrepresented the minimum velocity of the day by 4.26%, while in ON-T the underestimation was 18.44%.

5.2.3 WRF interpolation with one domain and nested simulations

WRF simulations obtained with one domain were interpolated in two points, the tower's position (ON-T) and the offshore position OFF-2, as the latter was the location that presented the best results previously. Wind speed, wind direction and air temperature of the one domain simulations were compared with simulation with a nested domain, interpolated in the location of the tower (ON-T-2D), with the aim to investigate the performance of the interpolation approach.

5.2.3.1 Wind speed

The diurnal cycle of the simulated wind speed with one domain (ON-T and OFF-2) and for a nested domain (ON-T-2D) are shown in Figure 30, along with the wind speed measurements at 98 m. Graphically, it is possible to observe that the results obtained with the nested simulation (ON-T-2D) are closer to the measured curve than those acquired with the one domain simulation (ON-T). This improvement was observed quantitatively through the calculation of the RMSE and Bias (Table 16), where both were reduced, by 7.7% and 13.3%, respectively.

Despite the small improvement observed in the wind speed simulation with a nested domain, this result was not better than the one acquired with a single domain simulation interpolated offshore. Again, the wind speed simulated and interpolated in the position OFF-2 presented the lowest errors, with a 1.69 m/s RMSE and -0.10 m/s Bias; whereas at ON-T-2D the RMSE was 1.95 m/s and the Bias -1.19 m/s.

As affirmed by Carvalho et al. (2012), one of the main sources of errors in weather forecasting is due to the misrepresentation of the terrain by the models. This can be the result of low-quality terrain input data or simulations with inadequate spatial resolution. Therefore, the simulation with a nested domain was obtained in order to verify if the increase of the grid resolution, from 15 km to 5 km, would lead to a significant improvement in the simulation. However, as presented, the improvement in the

wind speed simulation was small and still not better than the results obtained through the offshore interpolation approach.

Figure 30 – Diurnal wind speed cycle at 98 m for observed data and WRF results in offshore interpolation with one domain (OFF-2) and onshore interpolation with a nested domain (ON-T-2D).

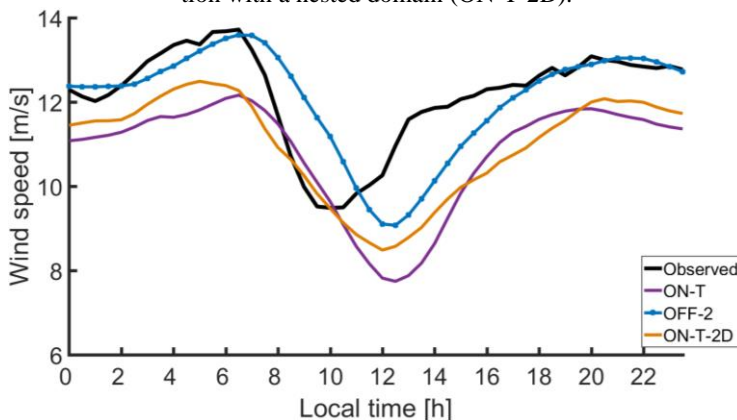


Table 16 – Wind speed statistical metrics for one domain simulations (ON-T and OFF-2) and for the nested domain simulation (ON-T-2D).

Points	RMSE [m/s]	Bias [m/s]
ON-T	2.12	-1.37
OFF-2	1.69	-0.10
ON-T-2D	1.95	-1.18

5.2.3.2 Weibull Probability Density Function

Wind speed data from the nested (ON-T-2D) and one domain simulations, interpolated at the tower's location (ON-T) and at an offshore point (OFF-2), are presented as simulated Weibull probability density function together with the measured Weibull PDF in Figure 31. Both simulations interpolated at the tower's position, ON-T and ON-T-2D, overestimate the frequency of low wind speeds and underestimate the frequency of high speeds. This causes both curves to be offset and positioned to the left of the measured PDF. In the same way, the most probable wind speed, the one with highest frequency, is underestimated in ON-T and ON-T-2D simulations, as shown in Table 17. The deviations of the simulated Vel_{prob} in ON-T and ON-T-2D were 11.03% and 9.61%, when compared to the measured data.

In Table 17, the Weibull PDF parameters are presented for the one and nested domain simulations, as well as the parameters obtained from the wind speed measurements. For both parameters, the lowest deviations from the observed values are exhibited in the OFF-2 dataset, where A is underestimated by 1.90% and k is overestimated by 22.64%. On the other hand, the highest deviations are presented by ON-T simulation, being 12.18% lower than the observed A and 24.96% higher than the observed k . Additionally, OFF-2 Weibull PDF is the closest curve to the observed. The most probable wind speed is very similar, OFF-2 misrepresents the observed Vel_{prob} by 0.71%, however, the simulated curve shows a lower wind speed distribution than the measured PDF, represented by the lower scale parameter value of OFF-2.

Figure 31 - Weibull probability density function for one domain simulations (ON-T and OFF-2) and for nested domain simulation (ON-T-2D).

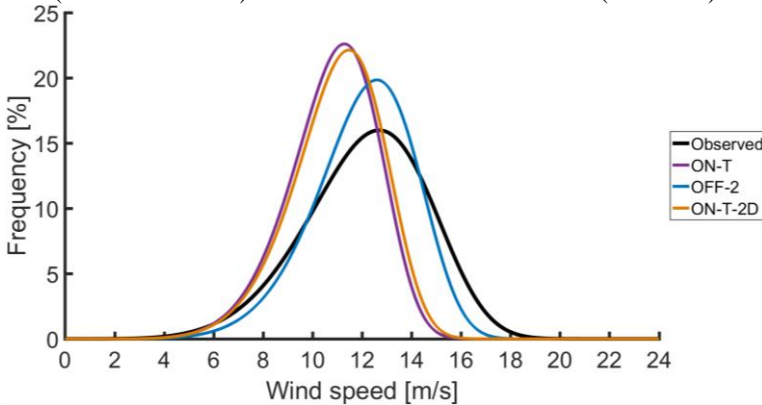


Table 17 – Weibull parameters and most probable wind speed for simulated and observed Weibull PDFs.

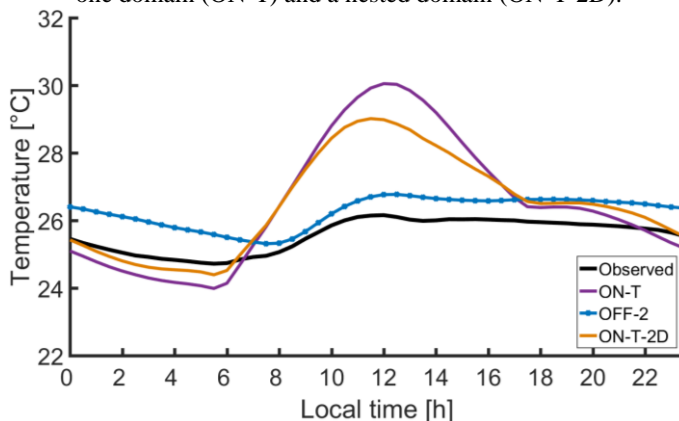
Data	A [m/s]	k	Vel_{prob} [m/s]
ON-T	11.54	7.01	11.29
OFF-2	12.89	6.88	12.60
ON-T-2D	11.72	6.97	11.47
Obs.	13.14	5.61	12.69

5.2.3.3 Temperature

The diurnal cycle of the air temperature at PSWF is depicted in Figure 32, where the mean measured and simulated temperatures are compared. Due to being located in a coastal region of northeastern Brazil, the

daily and annual temperature variations are small at the site. For the average observed diurnal cycle of the analyzed months, the minimum mean temperature was 24.7°C around 05 h and the maximum was 26.1°C at 12 h LT, representing a difference of 1.4°C throughout the day.

Figure 32 – Diurnal temperature cycle for observed data and WRF results in offshore interpolation with one domain (OFF-2) and onshore interpolation with one domain (ON-T) and a nested domain (ON-T-2D).



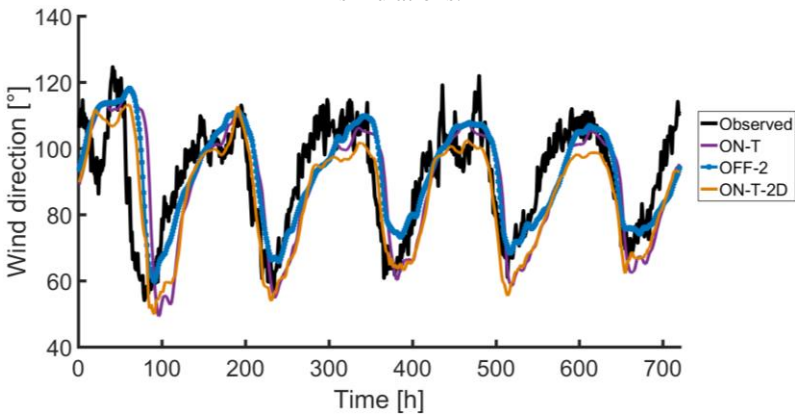
It is shown that both simulations interpolated in the tower's position (ON-T and ON-T-2D) predicted a greater thermal amplitude than that observed in Pedra do Sal. For the ON-T results, the thermal amplitude was overestimated, the predicted temperature difference was 6.1°C and the observed, 1.4°C. Likewise, the ON-T-2D simulation data showed a difference around three times higher than the measured one. Regarding the WRF one domain simulation interpolated at the offshore point OFF-2, it is noted that the simulated curve is very similar to the observed average temperature curve, but with a small overestimation, which occurs almost constantly along the day. On average, the temperature simulated at OFF-2 was 2.7% higher than the observed.

The RMSE and Bias between the measured and simulated data were: 1.43°C and 0.95 °C at ON-T, 1.19°C and 0.92°C at ON-T-2D, and 0.75°C and 0.69°C at OFF-2, respectively. Therefore, the simulation obtained in the location OFF-2 for the air temperature showed the most accurate results among all simulations.

5.2.3.4 Wind direction

The wind direction time series of the observed and simulated data (ON-T, OFF-2 and ON-T-2D) are depicted in Figure 33. Graphically, all simulated curves seem to reproduce well the characteristics of the observed wind direction in PSWF. However, as seen in the sensitivity analysis, the simulated data displayed smoother wind direction curves than the measured ones.

Figure 33 – Wind direction time series for observed, nested and one domain simulations.



Through the analysis of the statistical metrics (RMSE and Bias) of the one domain and nested simulations displayed in Table 18, it is possible to observe a small distinction between them. The lowest RMSE (9.50°) and Bias (0.37°) values were obtained with the one domain simulation interpolated in OFF-2; while worst performances, in terms of the wind direction simulation, were obtained with the WRF results interpolated at the tower's position, ON-T and ON-T-2D.

Table 18 - Wind direction statistical metrics for one domain simulations (ON-T and OFF-2) and for the nested domain simulation (ON-T-2D).

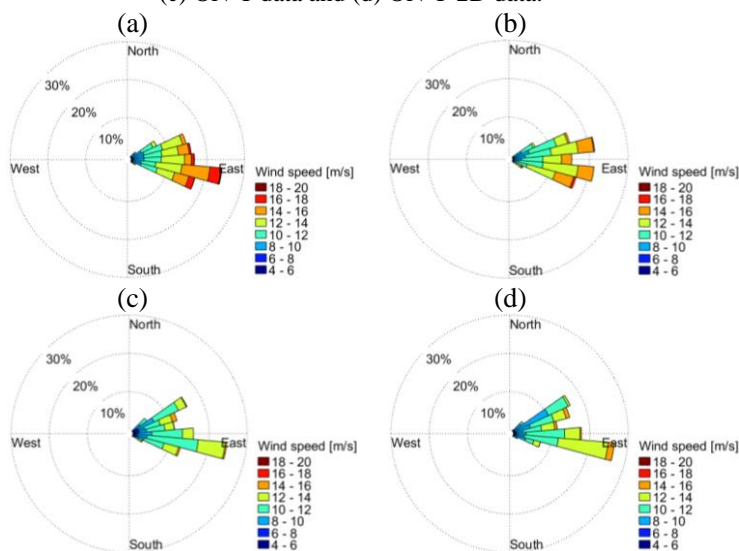
Points	RMSE [$^\circ$]	Bias [$^\circ$]
ON-T	12.21	-3.04
OFF-2	9.50	0.37
ON-T-2D	10.83	-5.08

The results obtained with the nested simulation showed the highest Bias among the wind direction simulations, equal to -5.08° , and the highest RMSE was obtained in the ON-T simulation (12.21°). Additionally, both simulated wind directions interpolated at the tower's location, ON-T and ON-T-2D, exhibited a counterclockwise deviation (negative Bias), whereas the simulated data interpolated in the offshore location (OFF-2) displayed a clockwise deviation (positive Bias).

5.2.3.5 Wind roses

The variation of the wind direction in PSWF, as well as the wind velocity and its frequency, are presented in the wind roses of the observed and simulated data of Figure 34, where the wind roses have an increment of 10° in each sector. It can be seen from Figure 34(a) that the wind direction, measured at 96 m a.g.l., presents little variation, being situated between the northeast and southeast directions in the analyzed period. In addition, regarding the wind farm's position (Figure 17), the main wind direction at PSWF is from the ocean to the land, which means that the wind is mostly free from terrain effects (TAKEYAMA et al., 2013).

Figure 34 – Wind roses of (a) observed data, (b) WRF interpolation OFF-2 data, (c) ON-T data and (d) ON-T-2D data.



The WRF output data interpolated at the tower's position (ON-T and ON-T-2D, Figure 34 (c) and (d), respectively) presented a main wind direction in their wind roses (consistent with that observed in PSWF (Figure 34 (a))). However, some inconsistencies were found in the other directions. In the 80° sector, both simulations underpredicted the wind frequency; also, ON-T and ON-T-2D overpredicted the wind frequency in the 60° sector. For the data interpolated at OFF-2, its wind rose showed two main directions, which, according to the observed data, did not happen in Pedra do Sal.

By only analyzing the main wind direction at the site (around 100° sector), the data that showed the most accurate simulation of the frequency was ON-T, with a small overestimation of about 2%. The results acquired at OFF-2 underestimated the frequency of the main wind direction by 11%, while at ON-T-2D, it was overestimated by 9%. Therefore, unlike the previous results, the one domain simulation data interpolated in the location of the tower obtained the best representation of the main wind direction at PSWF.

5.2.4 Conclusions

The wind speed simulation obtained by the interpolation of the one domain WRF results in the met mast position (ON-T), which is a common interpolation point, showed two main differences in comparison with the wind speed measurements: an underestimation of 11.3% and a delay in the simulation of the day minimum velocity in about 2 hours. As level and phase errors were observed in the simulated ON-T wind speed data, it was analyzed how the change in the interpolation location of the WRF output can affect the data obtained with a single domain simulation.

It was observed that the more onshore the interpolation point was located, the greater was the underestimation and delay between the observed and simulated wind velocities, where the Bias and RMSE went from -1.37 m/s and 2.12 m/s at ON-T to -2.52 m/s and 3.25 m/s at ON-2, respectively. Thus, due to the strong offshore wind conditions at PSWF, the offshore interpolations showed better results, in terms of lower RMSE and Bias, than the onshore interpolations.

The offshore interpolation that obtained the lowest errors for the simulated wind speed was OFF-2, with a RMSE of 1.69 m/s and a Bias of -0.1 m/s. This resulted in a reduction of 20.2% of the RMSE and 92.7% of the Bias when comparing the simulations interpolated in OFF-2 and in the tower's position (ON-T). In addition, regarding the level and phase

errors, the OFF-2 results showed a smaller level error than the ON-T data, despite similar phase errors.

Furthermore, with the aim to investigate the performance of the interpolation approach, a nested domain simulation was performed. This data was interpolated only on the tower's location (ON-T-2D) and showed slightly more accurate wind speed results than those obtained in the simulation ON-T, with a reduction of 7.7% in the RMSE and 13.3% in the Bias. However, the data obtained in ON-T-2D was not better than the one acquired with a single domain simulation interpolated offshore (OFF-2).

Regarding the air temperature simulation at PSWF, the OFF-2 data presented a simulated curve very similar to the observed one, with a small overestimation of 2.7% and low errors, RMSE of 0.75°C and Bias of 0.69°C. For the simulation of the wind direction, the WRF results interpolated at the tower's position, ON-T and ON-T-2D, showed higher RMSE and Bias (in absolute values) than the ones obtained with the one domain simulation interpolated in OFF-2 (RMSE of 9.50° and Bias of 0.37°). Furthermore, ON-T and ON-T-2D exhibited a counterclockwise deviation (negative Bias), while OFF-2 data displayed a clockwise deviation (positive Bias).

Controversially, in terms of wind rose, the results interpolated in the location OFF-2 did not present a good simulation of the main wind direction, where the frequency of the main wind direction was underestimated by 11%; while the ON-T simulation obtained the best performance, with a small overestimation of about 2%. This means that despite the good performance of the OFF-2 wind direction time series estimation, with lowest RMSE and Bias among all simulation, the data interpolated in the offshore point underestimated the frequency of wind direction in the 100° sector (main direction).

In conclusion, the offshore interpolation approach applied in the WRF's output data proved to be effective when applied to Pedra do Sal wind farm, which is a site located inland but presents strong offshore conditions that prevail over the onshore ones. This technique, when applied in a one domain simulation, uses less computational time than a nested simulation and obtained better results for the simulation of the wind speed and air temperature of PSWF by the WRF model.

Despite the significant improvement of the results obtained through the offshore interpolation approach, there is still a poor representation of the day minimum wind speed. It is believed that at daytime, due to solar radiation, the boundary layer becomes turbulent, which causes a decrease in the mean flow speed. However, there is a delay presented by

the model in simulating this effect. The reason for this delay has not yet been found and further studies are recommended to investigate its occurrence.

5.3 Horizontal interpolation approach applied in the wind power prediction

This section of the results intends to investigate if the offshore interpolation approach, described in Section 5.2, also obtains better results for the wind power prediction, when used as an input variable of an artificial neural network. The forecasts obtained using the WRF model used a single simulation domain with 15 km of grid resolution. In the previous results, NCEP-R2 reanalysis data were used in the WRF model to establish the initial and boundary conditions of the simulations, in order to adjust the model's configurations. However, for this result, NCEP-GFS ($0.5^\circ \times 0.5^\circ$ resolution) was applied as WRF input data, with the aim of obtaining atmospheric forecasts that, through the application of NN, will become forecasts of the wind power generation.

The model was set with the parameterizations described in the Methodology Section. After the downscaling process, the WRF's output data were interpolated in the OFF-2 offshore location and on the tower's position ON-T (Section 5.2). Each dataset was used to feed a neural network, thus, two NN were evaluated in the study, named NN-OFF-2 and NN-ON-T, to compare the performance of the interpolation approach.

The wind power produced by the 20 wind turbines installed at Pedra do Sal wind farm was used both for the training period and for the evaluation of the forecasts acquired through the ANN. Therefore, this measured data was divided into two databases, to separate the training and the validation data. Twenty-five cycles of training and prediction were performed, with a moving training length of 30 days and a prediction length of five days (120 hours), as described in Table 10.

The results showed here comprise the wind power prediction values obtained through a previously trained neural network, using as input atmospheric predictions from the WRF model, with 30 min time step for all datasets. Two three-layer feedforward neural networks were used, with 9 neurons in the input layer (wind speed at 40, 60, 80, 98 and 200 m, wind direction at 60 m, air temperature, pressure and humidity) and 1 neuron in the output layer (forecast of total energy production of the park); while in the hidden layer, different numbers of neurons were tested and their performances are presented in Table 19, Figure 35, Figure 36 and Figure 37.

Table 19 displays the mean errors of the wind power prediction, 25 cycles of 5 days, in terms of RMSE and Bias, which were also normalized according to the installed power capacity of the wind farm (GIEBEL et al., 2011), NRMSE and NBias, as well as the Person's coefficient (r) between measured and predicted wind power. Both neural networks, NN-ON-T and NN-OFF-2, were tested with different number of neurons in the hidden layer, from 1 to 100. Additionally, the Figure 35, Figure 36 and Figure 37 graphically showed the evolution of RMSE, Bias and Pearson's coefficient with the increase of the neurons number in the hidden layer of the NN.

Table 19 - Statistical metrics of wind power prediction with onshore and offshore interpolations.

Input data	N° of neurons	RMSE (MW)	NRMSE (%)	Bias (MW)	NBias (%)	r
ON-T	1	3.03	16.86	-0.26	1.43	0.61
	5	2.56	14.21	-0.17	0.94	0.74
	10	2.37	13.17	-0.12	0.68	0.78
	15	2.16	12.01	-0.08	0.45	0.82
	20	2.00	11.12	-0.06	0.35	0.85
	30	1.79	9.92	-0.04	0.21	0.88
	40	1.56	8.65	-0.02	0.09	0.91
	50	1.39	7.71	-0.02	0.12	0.93
	60	1.24	6.91	-0.02	0.09	0.95
	70	1.11	6.14	-0.01	0.07	0.96
	80	1.03	5.74	-0.01	0.04	0.96
90	1.06	5.87	-0.02	0.09	0.96	
100	1.15	6.39	-0.01	0.04	0.95	
OFF-2	1	2.91	16.15	-0.10	0.58	0.65
	5	2.50	13.91	-0.14	0.76	0.76
	10	2.26	12.58	-0.10	0.54	0.81
	15	2.11	11.75	-0.08	0.43	0.83
	20	2.00	11.12	-0.07	0.38	0.85
	30	1.70	9.44	-0.04	0.22	0.90
	40	1.51	8.41	-0.01	0.08	0.92
	50	1.34	7.44	-0.01	0.03	0.94
	60	1.16	6.43	0.01	0.04	0.95
	70	1.10	6.13	-0.03	0.18	0.96
	80	0.95	5.29	-0.01	0.04	0.97
90	1.03	5.73	-0.01	0.08	0.96	
100	1.03	5.73	-0.01	0.05	0.96	

The ANN that used the offshore interpolated database presented the best results in all tested configurations, in terms of RMSE and Bias. The lowest RMSE of the NN-OFF-2 predictions was 0.95 MW, corresponding to a NRMSE of 5.29%, and the lowest Bias was -0.01 MW, 0.04% NBias, both with the 80-neurons NN. Likewise, for the forecasts with ON-T dataset, the lowest RMSE and Bias were also obtained with a neural network with 80 neurons in the hidden layer, 1.03 MW RMSE and NRMSE of 5.74%, as well as -0.01 MW Bias and NBias of 0.04%.

Both neural networks displayed a majority of negative Bias in their predictions. The 60-neurons NN-OFF-2 was the only configuration to exhibit a positive Bias, equals to 0.01 MW (0.04% NBias), while all other networks underestimated the wind energy production of the wind farm regardless the number of neurons in the hidden layer. In addition, the simulations with the OFF-2 dataset started with lower Bias values than those obtained from the ON-T predictions. This result was already expected, since the WRF output data interpolated offshore (OFF-2 location) presented lower systematic errors than the onshore interpolated results (ON-T position). Also, the largest difference between the Bias of NN-ON-T and NN-OFF-2 occurred in the prediction with 1 neuron in the hidden layer, with NN-OFF-2 presenting a Bias 59% lower than the value obtained in NN-ON-T.

As the number of neurons increased in the hidden layers, the RMSE of both predictions decreased, until the 80-neurons configurations. The two analyzed neural network RMSE curves exhibited an inflection point with 80 neurons, Figure 35, and with a higher number of neurons the RMSE value started to grow again. Likewise, the Pearson's coefficient also had its values increased with higher neuron numbers, up to 80-neurons in the hidden layer (Figure 37). However, for the Bias, such trend was not completely observed, and an oscillation of its values was displayed, as seen in Figure 36.

The Pearson's correlation coefficient between the wind power predictions and the measured energy production of PSWF are displayed in Table 19 and in Figure 37. The NN-ON-T wind power predictions presented lower correlation values (r) than the results obtained by NN-OFF-2. If a strong correlation occurs with r values greater than 0.8, this is obtained for the simulation with fifteen neurons in the NN-ON-T and for ten neurons in NN-OFF-2. Additionally, among the performed simulations, the highest linear correlations were obtained with the 80-neurons neural networks, with r values of 0.96 for the NN-ON-T predictions and 0.97 for NN-OFF-2.

Figure 35 – RMSE of wind power predictions obtained with ANN with different neurons numbers

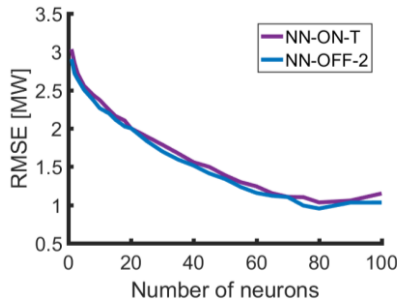


Figure 36 - Bias of wind power predictions obtained with ANN with different neurons numbers

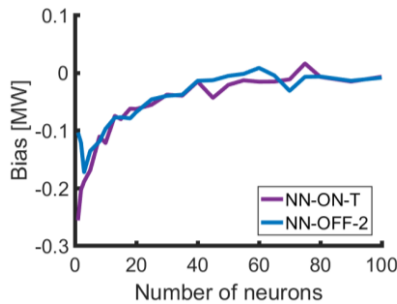
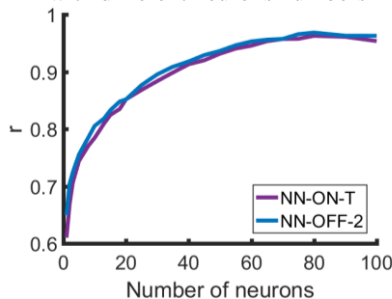


Figure 37 - Person's coefficient of wind power predictions obtained with ANN with different neurons numbers



In Figure 38, it is shown the relationship, in scatter plots, between measured and predicted power using 1, 20 and 80 neurons in the hidden layer for the two different input data from the WRF model. In both 1-neuron neural networks, there is no prediction of wind power values below 5 MW and above 18 MW (Figure 38 (a) and (b)). However, from 20

neurons in the hidden layer, low and high values of energy production start to be predicted by both neural networks, Figure 38(c) for NN-ON-T and Figure 38(d) for NN-OFF-2. Also, the highest and most uniform correlation throughout the range of produced wind energy was presented by the NN forecasts with 80 neurons (Figure 38 (e) and (f)). Therefore, the more neurons in the hidden layer (up to the overfitting limit), the greater is the neural network's ability to predict the peaks and valleys of wind power production fluctuations, as can also be seen in Figure 39 and Figure 40.

Figure 38 – Correlation between predicted and measured wind power for NN simulations with (a) ON-T data and 1 hidden neuron, (b) OFF-2 data and 1 hidden neuron (c) ON-T data and 13 hidden neurons, (d) OFF-2 data and 20 hidden neurons (e) ON-T data and 20 hidden neurons and (f) OFF-2 data and 80 hidden neurons.

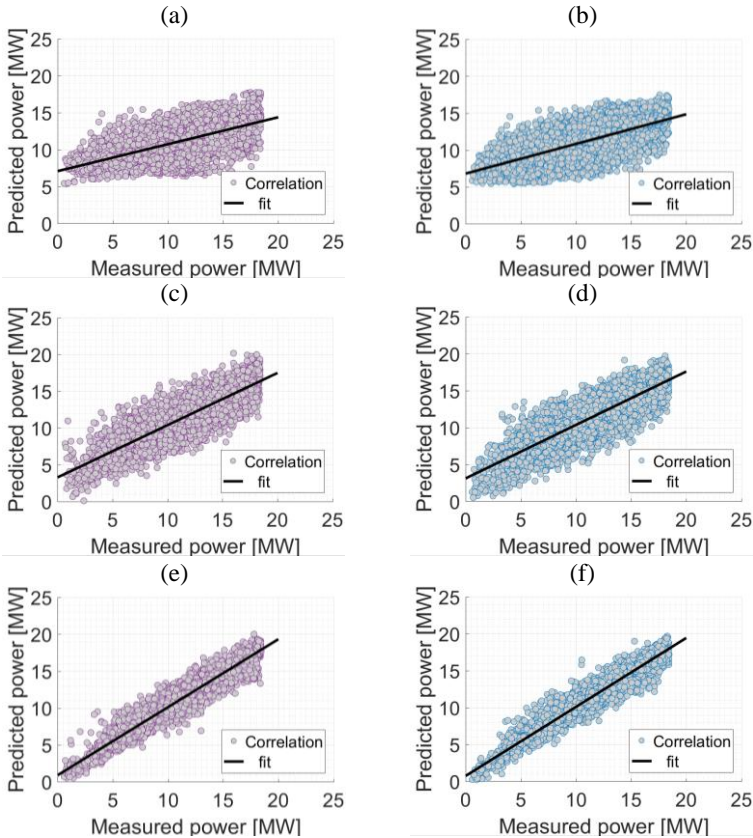


Figure 39 - Wind power time series for measured and simulation data with one, twenty and eighty neurons in the hidden layer using OFF-2 WRF results.

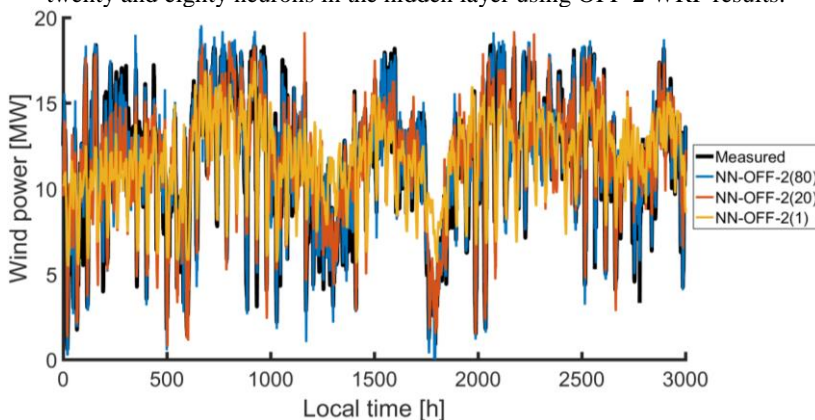
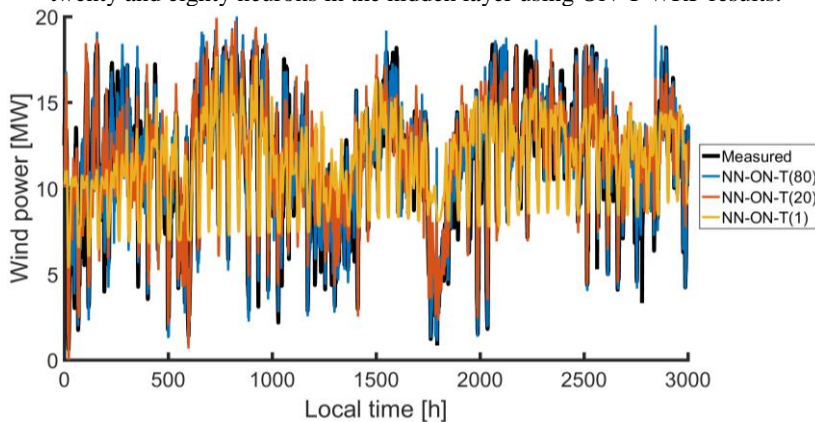


Figure 40 - Wind power time series for measured and simulation data with one, twenty and eighty neurons in the hidden layer using ON-T WRF results.



The mean diurnal cycles of the predicted wind power by different configurations of NN-ON-T and NN-OFF-2 are shown in Figure 41, Figure 42 and Figure 43 along with the averaged energy production of PSWF. As observed in the diurnal cycle of the simulated wind speed, the predictions obtained with the 1-neuron neural networks also presented a phase error (GIEBEL et al., 2011), with a delay in the prediction of the day minimum wind energy production (Figure 41). However, this error was corrected with the use of at least 10 neurons in the hidden layer, for both NN, as can be observed in Figure 42.

Figure 41 – Wind power diurnal cycle for measured and predicted data with 1 neuron.

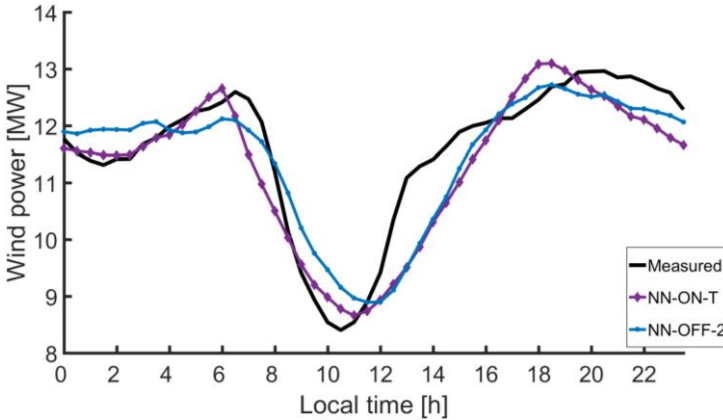
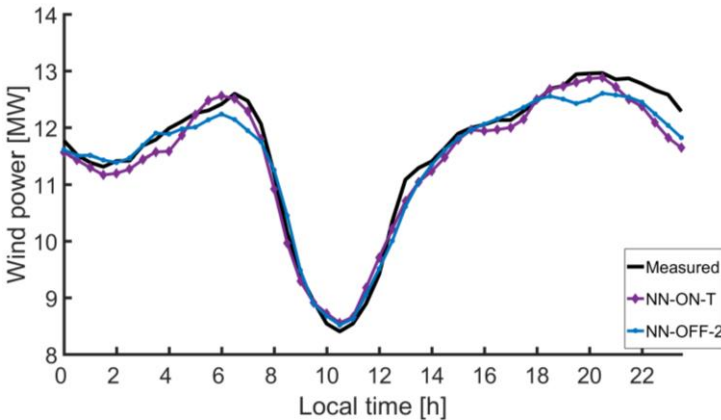
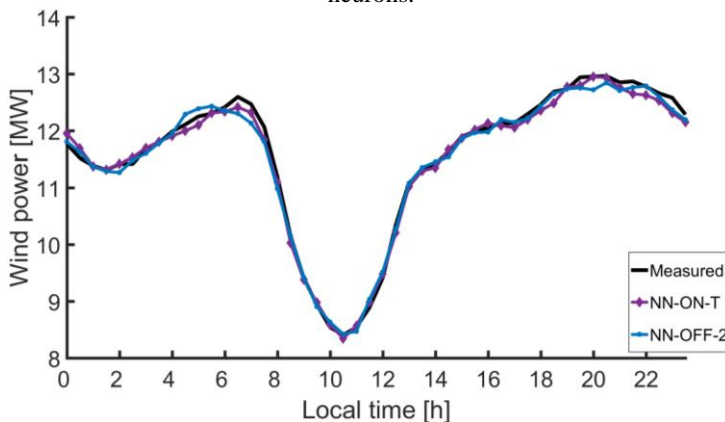


Figure 42 – Wind power diurnal cycle for measured and predicted data with 10 neurons.



The 10-neurons NN were able to predict the time of the day of lower wind energy production, but still misrepresented the wind power at night and earlier in the morning. The best simulations of the wind power diurnal cycle were obtained with the 80-neurons neural networks presented in Figure 43, where small deviations from the measured curve are observed and there are no occurrence of phase and level errors in the representation of the lowest energy production of the day.

Figure 43 - Wind power diurnal cycle for measured and predicted data with 80 neurons.



5.3.1 Conclusions

The sensitivity analysis of the neural network forecasts, in relation to the number of neurons in the hidden layer, showed that, for both input data sources, the NN with 80 neurons presented accurate wind power results. The 120-hour predictions, with 30 min means, obtained from the onshore interpolated WRF data (ON-T) displayed a NRMSE equal to 5.74% and NBias of 0.04%, for the 80-neurons neural network. On the other hand, predictions using OFF-2 data as input obtained a NRMSE of 5.29% and a NBias of 0.04%, for the same network architecture. However, regardless of the neurons number and the input data, the majority of wind power forecasts underestimated the measured energy production. In addition, it was concluded that with the increase in the number of neurons, the greater the network capacity to predict fluctuations in the wind energy generation. Likewise, for the prediction of the wind power diurnal cycle, the 80-neurons neural networks did not show level and phase errors in the representation of the minimum wind energy production of day.

Regarding the application of the interpolation approach in the wind power forecast, it was observed that the predictions made from the interpolated offshore data presented smaller systematic errors (28.6% lower on average for all tests), which is due to OFF-2 wind speed input showing lower Bias than ON-T data. In addition, NN-OFF-2 showed a linear correlation with the measured wind energy production higher than NN-ON-T forecasts.

All these results lead to the assumption that the more neurons in the hidden layer (up to the limit of overfitting), the lower the influence of the input data on the neural network prediction. Nonetheless, with more neurons, greater is the computational cost. Therefore, the interpolation approach becomes attractive to wind power prediction with NN, since better results can be acquired using fewer neurons when the input data is interpolated offshore.

6 FINAL CONSIDERATIONS

Coastal regions have specific characteristics that are important for realistic atmospheric prediction and, at the same time, are difficult to incorporate into a forecasting model. In order to provide wind predictions, numerical models divide a defined domain within grid cells, where inside each of these cells, calculations are made using mean properties. Therefore, in a coastal region where part of the grid cell is water and part is land, the calculated average parameters are not suitable for an accurate representation of coastal features. At these areas, there is an abrupt change in the surface roughness, a temperature gradient between land and sea and humidity differences that affect the spatial and temporal variability of the wind (BARTHELMIE, 1999).

In Pedra do Sal wind farm, the wind blows predominantly from the ocean to the land. Thus, when the wind flow is over the water, it encounters few resistances due to the low surface roughness of the sea. However, when reaching land, the wind is suddenly over a region of higher surface roughness and susceptible to a higher drag coefficient, which reduces its velocity. Consequently, a horizontal wind speed gradient occurs between the onshore and offshore region. As there is just one meteorological mast at the site, measuring the horizontal wind speed change was not possible. Nevertheless, analyzing observational data from this mast, located about 400 m from the shoreline, a strong influence of the ocean on the wind was observed.

With the current wind energy penetration in the Brazilian energy matrix, as well as the growth perspective of this energy, the importance of developing accurate wind speed and wind power prediction is evident. However, as forecasting models provide the spatial mean of the wind speed for each grid cell and meteorological measurements are punctual, and influenced by atmospheric phenomena in their vicinity, there is the doubt whether it is better to use forecast results of the nearest grid point or to interpolate these results (SILE et al., 2014).

Atmospheric simulations of the WRF model were evaluated in this study, where several tests were conducted aiming to increase the performance of its simulations and, thus, reduce wind prediction errors. Firstly, a sensitivity analysis was carried out regarding the planetary boundary layer parameterization, due to its great influence on the modeling of near-surface winds. Differences obtained in the WRF simulations were investigated through the variation of this parameter, as well as it was sought to identify the PBL scheme that best represented the local wind features at PSWF.

In the sensitivity analysis, six different PBL parameterizations were applied in the WRF model, combined with surface layer and land surface schemes. Overall, all six simulations consistently underestimated the wind speed measured at 98 m a.g.l. MYNN2-MYNN-Noah was the set of PBL-SL-LS schemes that displayed the highest performance in simulating the wind and the air-temperature. Through this analysis, the wind speed simulation errors were reduced by 32.5% of RMSE and 52.6% of Bias, when comparing the worst parameterization set (S-1) and the best (S-4); while, when comparing with the default configuration of the WRF model (S-6), the reduction of RMSE and Bias were equal to 28.1% and 48.7%, respectively.

Secondly, after finding the best PBL scheme for PSWF, a horizontal interpolation approach of the results obtained by the WRF model was tested. The one-domain WRF simulations were linearly interpolated in four offshore locations, in the met mast's position and in two more onshore locations, which crossed the shoreline and the wind farm in the north-south direction. Additionally, the results obtained in a nested-domain simulation, interpolated only in the position of the anemometric tower, were used to assess the interpolation approach performance.

For the data interpolation analysis, the offshore locations displayed lower errors in the wind speed prediction than the onshore interpolation points, with a 36% lower RMSE and 94% lower Bias, on average, which reinforces the strong offshore condition at the onshore wind farm. The WRF results interpolated in the location OFF-2 showed the highest simulation performance between all the analyzed points. Comparing the wind speed interpolated in the OFF-2 location with the obtained in the tower's position (ON-T), which is a usual interpolation point, there was a reduction of the simulation error by 20.2% in the RMSE and 92.7% in the Bias. In addition, despite the improvement in the wind speed results obtained in the simulation with the nested domain, the ON-T-2D simulation did not display smaller errors than those obtained in OFF-2.

Thirdly, the offshore interpolation approach was applied in the wind power prediction using ANN. The ON-T and OFF-2 WRF simulations were employed as input of neural networks to investigate the performance of the interpolation approach and the combined use of WRF and ANN models for predicting the wind energy production of PSWF. Two three-layers feedforward neural networks (NN-ON-T and NN-OFF-2), with 9 neurons in the input layer, were tested with different numbers of neurons in the hidden layer.

In the neural network analysis, both networks displayed accurate wind power predictions using 80 neurons in the hidden layer. The NN-

OFF-2 results showed a RMSE 7.7% lower than the NN-ON-T predictions, as well as a Bias 7.4% lower, for the same 80-neurons architectures. In addition, it was observed that with more neurons in the hidden layer, the greater is the network's ability to predict wind power fluctuations. Likewise, with the increase in the number of neurons (up to the limit of overfitting), lower is the influence of the data interpolation on the NN performance, however, higher is the computational cost.

In conclusion, according to the results, the offshore interpolation of the atmospheric simulations obtained by the WRF model proved to be a feasible approach to be implemented in the wind speed and power predictions at the coastal Pedra do Sal wind farm, which uses less computational time, achieves higher performance and lower prediction errors when compared to simulations with nested domains.

6.1 FURTHER STUDIES

Suggestions to future works are:

- Evaluate the application of the observational data assimilation method in the WRF model, to improve the simulation results;
- Investigate the WRF atmospheric simulations on the rainy season, as the wind features at Pedra do Sal wind farm diverge between the dry and rainy months;
- Analyze the application of the interpolation approach in another coastal wind farm, preferably located at the Brazilian Northeast;
- Investigate the delay of the WRF model in predicting the minimum wind speed condition in the diurnal cycle;
- Compare the results obtained with the combined use of NWP predictions and NN with the use of only NN and wind power time series;
- Test the neural network using a set of WRF predictions as input data (several parameterizations, domains and interpolations);
- Further improvements in the ANN to reduce forecasting errors of wind power, regarding analysis of the network architecture, activation functions and training algorithm;
- Analyze the evolution of the prediction error with the increase of the forecast time-horizon of wind speed and power predictions.

REFERENCES

AGUADO, E.; BURT, J. E. **Understanding weather and climate**. 7th ed. Glenview: Pearson, 2015.

ALLAMILLOS, F. J. S.; VÁSQUEZ, D. P.; ARIAS, J. A. R.; FANEGO, V. L.; PESCADOR, J. T. Analysis of WRF model wind estimate sensitivity to physics parameterization choice and terrain representation in Andalusia (southern Spain). **Journal of Applied Meteorology and Climatology**, v. 52, p. 1592-1609, feb. 2013.

ANEEL. **BIG – Banco de Informações de Geração**. Capacidade de geração do Brasil. 2018. Available in: <<http://www2.aneel.gov.br/aplicacoes/capacidadebrasil/capacidadebrasil.cfm>>. Accessed in: apr. 2018.

ARCHER, C.L.; COLLE, B.A.; MONACHE, L. D.; DVORAK, M.J.; LUNDQUIST, J.; BAILEY, B. H.; BEAUCAGE, P.; CHURCHFIELD, M. J.; FITCH, A. C.; KOSOVIC, B.; LEE, S. Meteorology for coastal/off-shore wind energy in the United States: recommendations and research needs for the next 10 years. **Bulletin of the American Meteorological Society**, v. 95, n. 4, p. 515-519, apr. 2014.

ARYA, P. S. **Introduction to micrometeorology**. 2nd ed. London: Academic Press, 2011.

ATA, R. Artificial neural networks applications in wind energy systems: a review. **Renewable and Sustainable Energy Reviews**, v. 49, p. 534-562, set. 2015.

BALZARINI, A.; ANGELINI, F.; FERRERO, L.; MOSCATEKKI, M.; PERRONE, M. G.; PIROVANO, G.; RIVA, G. M.; SANGIORGI, G.; TOPETTI, A. M.; GOBBI, G. P.; BOLZACHINNI, E. Sensitivity analysis of PBL schemes by comparing WRF model and experimental data. **Geoscientific Model Development Discussions**, v. 7, p. 6133-6171, sept. 2014.

BANKS, R. F.; TIANA-ALSINA, J.; BALDASANO, J. M.; ROCA-DENBOSCH, F.; PAPAYANNIS, AL.; SOLOMOS, S.; TZANIS C. G. Sensitivity of boundary-layer variables of PBL schemes in the WRF

model based on surface meteorological observations, lidar and radiosondes during the HygraA-CD campaign. **Atmospheric Research**, v. 176-177, p. 185-201, aug. 2016.

BARRETO, A. B.; ARAGÃO, M. R. S.; BRAGA, C. C. Estudo do ciclo diário do vento à superfície no nordeste do Brasil. **XII Congresso Brasileiro de Meteorologia**, 2002.

BARTHELMIE, R. J.; BADGER, J.; PRYOR, S. C.; HASAGER, C. B.; CHRISTIANSEN, M. B.; JØRGENSEN, B. H. Offshore coastal wind speed gradients: Issues for the design and development of large offshore windfarms. **Wind Engineering**, v. 31, n. 6, p. 369-382, 2007.

BARTHELMIE, R. J. The effects of atmospheric stability on coastal wind climates. **Meteorological Applications**, v. 6, n.1, p. 39-47, 1999.

BARTHELMIE, R. J.; PALUTIKOF, J. P. Coastal wind speed modelling for wind energy applications. **Journal of Wind Engineering and Industrial Aerodynamics**, v. 62, p. 212-236, 1996.

BECCARIO, C. **Earth**. Available in: <earth.nullschol.net>. Accessed in: apr. 2018.

BOUGEAULT, P.; LACARRÈRE, P. Parameterization of orography-induced turbulence in a mesobeta-scale model. **Monthly Weather Review**, v. 117, p. 1872-1890, mar. 1989.

BRETHERTON, C. S.; PARK, S. A new moist turbulence parameterization in the community atmosphere model. **Journal of Climate**, v. 22, p. 3422-3448, oct. 2008.

BURTON, T; JENKINS, N.; SHARPE, D.; BOSSANYI, E. **Wind energy handbook**. 2nd ed. Chichester: Wiley, 2011.

CAMBAZOGLU, M. K.; BLAIN, C. H.; SMITH, T. A.; LINZELL, R. S. Relationships between wind predictions and model resolution over coastal regions. **Ocean Engineering**, v. 112, p. 97-116, jan. 2016.

CANNON, F.; CARVALHO, L. M. V.; JONES, C.; HALL, T.; GOMBERG, D.; SUMAS, J.; JACKSON, M. WRF simulation of downslope

events in coastal Santa Barbara County. **Atmospheric Research**, v. 191, p. 57-73, 2017

CARVALHO, D. J. S.; ROCHA, A.; GESTEIRA, M. G.; SANTOS, C. S. Sensitivity of the WRF model wind simulation and wind energy production estimates to planetary boundary layer parameterizations for on-shore and offshore areas in the Iberian Peninsula. **Applied Energy**, v. 135, p. 234-246, dec. 2014a.

CARVALHO, D. J. S.; ROCHA, A.; GESTEIRA, M. G.; SANTOS, C. S. WRF wind simulation and wind energy production estimates forced by different reanalysis: Comparison with observed data for Portugal. **Applied Energy**, v. 117, p. 116-126, mar. 2014b.

CARVALHO, D.; ROCHA, A.; GÓMES-ESTEIRCA, M.; SANTOS, C. A sensitivity study of the WRF model in wind simulation for an area of high wind energy. **Environmental Modelling & Software**, v. 33, p. 23-34, mar. 2012.

CARVALHO, D. J. S. **Optimização do modelo numérico de previsão do tempo WRF no contexto de previsão e produção de energia eólica**. Dissertation (Master in Meteorology and Physical Oceanography) - Universidade de Aveiro, Portugal, 2009.

CASTELLANI, F.; ASTOLFI, D.; MANA, M.; BURLANDO, M.; MEIBNER, C.; PICCIONI, E. Wind power forecasting techniques in complex terrain: ANN vs. ANN-CFD hybrid approach. **Journal of Physics: Conference Series**, v. 753, n. 8, p. 082002. IOP Publishing, 2016.

CATALÃO, J.; POSUINHO, H.; MENDES, V. Short-term wind power forecasting in Portugal by neural networks and wavelet transform. **Renewable Energy**, v. 36, n. 4, p. 1245-1251, apr. 2011.

CAVALCANTI, I. F. A.; FERREIRA, N. J.; SILVA, M. G.A.J.; DIAS, M. A. F. S. **Tempo e clima no Brasil**. São Paulo: Oficina de Textos, 2009.

CCEE. **Leilões**. Available in: < <https://goo.gl/QbLZVL>>. Accessed in: apr. 2018.

COELINGH, J. P.; VAN WIJK, A. J. M.; HOLTSLAG, A. A. M. Analysis of wind speed observations on the North Sea coast. **Journal of Wind Engineering and Industrial Aerodynamics**, v. 73, n. 2, p. 125-144, 1998.

COIFFIER, J. **Fundamentals of numerical weather prediction**. Cambridge: Cambridge University Press, 2011.

DAMAS, L. B. **Análise de geração e aplicação do método MCP em dois parques eólicos em operação no Brasil**. Dissertation (Master in Mechanical Engineering) - Universidade Federal de Santa Catarina, Florianópolis, 2013.

DRAXL, C. **On the predictability of hub height winds**. Thesis (Wind Energy PhD) – Denmark Technical University, Denmark, 2012.

DUDHIA, J. A history of mesoscale model development. **Asia-Pacific Journal of Atmospheric Sciences**, v. 50, n. 1, p. 121-131, jan. 2014.

EIA. **Annual energy outlook 2017**. 2017. Available in: <[https://www.eia.gov/outlooks/aeo/pdf/0383\(2017\).pdf](https://www.eia.gov/outlooks/aeo/pdf/0383(2017).pdf)>. Accessed in: jul. 2017.

EMEIS, S. **Wind energy meteorology**. Atmospheric physics for wind power generation. Berlin: Springer, 2013.

ENGIE. **Central eólica Pedra do Sal**. Available in: <<http://www.engieenergia.com.br/wps/portal/internet/parque-gerador/usinas-complementares/central-eolica-pedra-do-sal>>. Accessed in: set. 2017.

EPE. **Balanco energético nacional 2017**. Relatório síntese – ano base 2016. 2017. Available in: <https://ben.epe.gov.br/downloads/S%c3%adntese%20do%20Relat%c3%b3rio%20Final_2017_Web.pdf>. Accessed in: jul. 2017.

EPE. **O compromisso do Brasil no combate às mudanças climáticas: Produção e uso de energia**. 2016. Available in: <<http://www.epe.gov.br/mercado/Documents/NT%20COP21%20iNDC.pdf>>. Accessed in: mar. 2017.

FERREIRA, A. P.; CASTANHEIRA, J. M.; ROCHA, A.; FERREIRA, J. Estudo de sensibilidade das previsões de superfície em Portugal pelo WRF face à variação das parametrizações físicas. **XXX Jornadas Científicas de la Asociación Meteorológica Española**, Zaragoza, 2008.

FISCH, G. Características do perfil vertical do vento no Centro de Lançamento de Foguetes de Alcântara (CLA). **Revista Brasileira de Meteorologia**, v. 14, n. 1, p. 11-21, 1999.

FOKEN, T. **Micro-meteorology**. Berlin: Springer, 2008.

FOX, B.; BRYANS L., FLYNN, D.; JENKINS, N.; MILBORROW, D.; O'MALLEY, M.; WATSON, R.; ANAYA-LARA, R. **Wind power integration**. Connection and system operational aspects. 2nd edition. London: The Institute of Engineering and Technology, 2014.

FUCK, V. R. **Tratamento de dados eólicos e avaliação da velocidade do vento com uso de perfilador LIDAR**. Dissertation (Undergraduation in Mechanical Engineering) – Universidade Federal de Santa Catarina, Florianópolis, 2016.

GIANNAROS, T. M.; MELAS, D.; ZIOMAS, I. Performance evaluation of the Weather Research and Forecasting (WRF) model for assessing wind resource in Greece. **Renewable Energy**, v. 102, p. 190-198, 2017.

GIEBEL, G.; BROWNSWORD, R.; KARINIOTAKIS, G.; DENHARD, M.; DRAXL, C. **The state-of-the-art in short-term prediction of wind power: A literature overview**. ANEMOS.plus, jan. 2011.

GIORGI, M. G.; FICARELLA, A.; TARANTINO, M. Assessment of the benefits of numerical weather predictions in wind power forecasting based on statistical methods. **Energy**, v. 36, p. 3968-3978, jun. 2011.

GISLER, C. A. F.; FISCH, G.; CORREA, C. S. Análise estatística do perfil de vento na camada limite superficial no centro de lançamento de Alcântara. **Journal of Aerospace Technology and Management**, v. 3, n. 2, p. 193-202, 2011.

GWEC. **Global wind report 2017**. 2018. Available in: <<http://files.gwec.net/files/GWR2017.pdf>>. Accessed in: apr. 2018.

GWEC. **Global wind report 2016**. 2017. Available in: <<http://files.gwec.net/files/GWR2016.pdf>>. Accessed in: jul. 2017.

GWEC. **Global wind report 2015**. Annual market update. 2016a. Available in: <http://www.gwec.net/wp-content/uploads/vip/GWEC-Global-Wind-2015-Report_April-2016_22_04.pdf>. Accessed in: jun. 2016.

GWEC. **Wind power leads all new power generation**. Big markets dominate in 2015. 2016b. Available in: <<http://campaign.r20.constantcontact.com/render?ca=9e80e097-d8fb-4e7a-a49d-b6348dd4d007&preview=true&m=1102949362881&id=preview>>. Accessed in: jun. 2016.

HAU, E. **Wind turbines**. Fundamentals, technologies, application, economics. 3rd ed. Berlin: Springer, 2013.

HAYKIN, S. **Neural networks and learning machines**. 3rd ed. New Jersey: Pearson, 2009.

HONG, S-Y; NOH, Y. A new vertical diffusion package with an explicit treatment of entrainment processes. **Monthly Weather Review**, v. 134, pp 2318 – 2341, sept. 2006.

HSU. **Coastal meteorology**. San Diego: Academic Press, 1988.

INTERNATIONAL ELECTROTECHNICAL COMMISSION. **IEC 61400-12-1: Power performance measurements of electricity producing wind turbines**. Geneva, 2005.

IRENA. **Featured Dashboard – Capacity and Generation**. 2018. Available in: <<http://resourceirena.irena.org/gateway/dashboard/?topic=4&subTopic=16>>. Accessed in: apr. 2018.

IRENA. **REthinking energy 2017**. 2017. Available in: <http://www.irena.org/DocumentDownloads/Publications/IRENA_RE-thinking_Energy_2017.pdf>. Accessed in: mar. 2017.

IRENA. **The power to change: Solar and wind cost reduction potential to 2025**. 2016. Available in: <http://www.irena.org/DocumentDownloads/Publications/IRENA_Power_to_Change_2016.pdf>. Accessed in: mar. 2017.

JAIN, P. **Wind energy engineering**. New York: Mc Graw Hill, 2010.

JANJIC, Z. I. The step-mountain Eta coordinate model: Further developments of the convection, viscous sublayer, and turbulence closure schemes. **Monthly Weather Review**, v. 122, p. 927-945, may 1994.

JONG, P.; DARGAVILLE, R.; SILVER, J.; UTEMBE, S.; KIPERSTOCK, A.; TORRES, E. A. Forecasting high proportions of wind energy supplying the Brazilian Northeast electricity grid. **Applied Energy**, v. 195, p. 538-555, jun. 2017.

KALNAY, E. **Atmospheric modeling, data assimilation and predictability**. Cambridge: Cambridge University Press, 2003.

KARSOLIYA, S. Approximating number of hidden layer neurons in multiple hidden layer BPNN architecture. **International Journal of Engineering Trends and Technology**, v. 3, n. 6, p. 714-717, 2012.

KLECZEK, M. A.; STEENEVELD, G. J.; HOLTSLAG, A. A. Evaluation of the weather research and forecasting mesoscale model for GABLS3: impact of boundary-layer schemes, boundary conditions and spin-up. **Boundary-layer Meteorology**, v. 152, n. 2, p. 213-243, 2014.

KRUSE, R.; BORGELT, C.; BRAUNEM C.; MOSTAGHIM, S.; STEINBRECHER, M. **Computational intelligence**. A methodological introduction. 2nd ed. London: Springer, 2016.

LANDBERG, L. **Meteorology for wind energy**. An introduction. Chichester: Wiley, 2016.

LANGE, M.; FOCKEN, U. **Physical approach to short-term wind power prediction**. Berlin: Springer Science & Business Media, 2006.

LEI, M.; SHIYAN, L.; CHUANWEN, J.; HONGLING, L.; YAN, Z. A review on the forecasting of wind speed and generated power. **Renewable and Sustainable Energy Reviews**, v. 13, issue 4, p. 915-920, may 2009.

LIRA, M. A. T.; NETO, J. M. M.; LOIOLA, J. V. L.; SILVA, E. M.; ALVES, J. M. B. Caracterização do regime de ventos no Piauí para o aproveitamento de energia eólica. **Revista Brasileira de Meteorologia**, v. 32, n. 1, p. 77-88, 2017.

LIRA, M. A. T.; NETO, J. M. M.; SILVA, E. M.; SOMBRA, B. P. quantificação dos recursos eólicos no estado do Piauí através de simulações computacionais. **Ciência e Natura**, v. 38, p. 245 – 251, 2016.

LIRA, M. A. T.; SILVA, E. M.; ALVES, J. M. B. Estimativa dos recursos eólicos no litoral cearense usando a teoria da regressão linear. **Revista Brasileira de Meteorologia**, v. 26, n. 3, p. 349-366, 2011.

LUTGENS, F. K.; TARBUCK, E. J. **The Atmosphere**. An introduction to meteorology. 12th ed. Boston: Pearson, 2012.

LUTGENS, F. K.; TARBUCK, E. J. **The Atmosphere**. An introduction to meteorology. 11th ed. Boston: Pearson, 2010.

LYNCH, P. The origins of computer weather prediction and climate modeling. **Journal of Computational Physics**, v. 227, n. 7, p. 3431-3444, mar. 2008.

MACHADO, V. S. **Previsão da geração eólica utilizando a técnica de redes neurais artificiais: estudo de caso do Parque Eólico de Pedra do Sal – PI**. Dissertation (Undergraduation in Mechanical Engineering) – Universidade Federal de Santa Catarina, Florianópolis, 2014.

MANWELL, J. F.; MCGOWAN, J. G.; ROGERS, A. L. **Wind energy explained**. Theory, design and application. 2nd ed. West Sussex: Wiley, 2009.

MELO, E. **Brasil um potencial de produção de energia eólica**. Available in: <<http://www.abeeolica.org.br/pdf/artigos/Artigo-UOL.pdf>>. Accessed in: mar. 2015.

MILOVAC, J.; WARRACH-SAGI, K.; BEHRENDT, A.; SPÄTH, F.; INGWERSEN, J.; WULFMEYER, V. Investigation of PBL schemes combining the WRF model simulations with scanning water vapor differential absorption lidar measurements. **Journal of Geophysical Research: Atmospheres**, v. 121, p. 624-649, 2016.

MONTEIRO, C.; BESSA, R.; MIRANDA, V.; BOTTERUD, A.; WANG, J.; CONZELMANN, G. **Wind power forecasting: state-of-the-art 2009**. Chicago: Argonne National Laboratory, 2009.

NAKANISHI, M.; NIINO, H. An improved Mellor-Yamada level-3 model: Its numerical stability and application to a regional prediction of advection fog. **Boundary Layer Meteorology**, col. 119, p. 397-407, mar. 2006.

NATIONAL CENTER FOR ATMOSPHERIC RESEARCH (NCAR). **Weather Research and Forecasting ARW**. Version 3 modeling system user's guide. Jul. 2016.

NATIONAL CENTER FOR ATMOSPHERIC RESEARCH (NCAR). **ARW version 3 modelling system user's guide**. Jan. 2015.

NCEP. **Global Forecast System (GFS)**. 2007. Available in: <<https://www.ncdc.noaa.gov/data-access/model-data/model-datasets/global-forecast-system-gfs>>. Accessed in: dec. 2016.

NCEP. **NCEP/DOE Reanalysis 2 (R2)**. 2000. Available in: <<https://www.esrl.noaa.gov/psd/data/gridded/data.ncep.reanalysis2.html>>. Accessed in: dec. 2016.

NELSON, V. **Wind energy**. Renewable energy and the environment. Boca Raton: CRC Press, 2009.

NOAA. **2-minute Gridded Global Relief Data (ETOPO2) v2**. 2017. Available in: <<https://data.nodc.noaa.gov/cgi-bin/iso?id=gov.noaa.ngdc.mgg.dem:301>>. Accessed in: apr. 2018.

NOAA. **Global Forecast System**. 2016. Available in: <<https://www.ncdc.noaa.gov/data-access/model-data/model-datasets/global-forecast-system-gfs>>. Accessed in: jun. 2016.

NOAA. **Historical El Nino/ La Nina episodes (1950-present)**. 2015a. Available in: <http://www.cpc.ncep.noaa.gov/products/analysis_monitoring/ensostuff/ensoyears2011.shtml>. Accessed in: dec. 2015.

NOAA. **NOAA Optimum Interpolation Sea Surface Temperature Analysis**. 2015b. Available in: <http://www.emc.ncep.noaa.gov/research/cmb/sst_analysis/>. Accessed in: dec. 2015.

ONS. **Plano da operação elétrica 2017/2018**. 2017. Available in: <http://www.ons.org.br/AcervoDigitalDocumentosEPublicacoes/PEL2017-2018_Sumario_Executivo.pdf>. Accessed in: jan. 2017.

ONS. **Submódulo 8.1**. Programação diária da operação eletroenergética. 2016. Available in: <[http://extranet.ons.org.br/operacao/prdocme.nsf/identificadorlogico/E63F5CC041DD653A83258098005FECAF/\\$file/Su%20B3dulo%208.1.pdf?openelement](http://extranet.ons.org.br/operacao/prdocme.nsf/identificadorlogico/E63F5CC041DD653A83258098005FECAF/$file/Su%20B3dulo%208.1.pdf?openelement)>. Accessed in: mar. 2017.

PIDWIRNY, M. **Understanding physical geography**. 1st ed. Kelowna: Our Planet Earth Publishing, 2014.

PIELKE, R. A. **Mesoscale meteorological modeling**. 3rd ed. Waltham: Academic Press, 2013.

PINTO, L. I. C. **Avaliação do modelo WRF para aplicação e previsão de recursos eólicos no Nordeste brasileiro**. Thesis (Earth System Science PhD) – Instituto Nacional de Pesquisas Espaciais, São José dos Campos, 2017.

PLEIM, J. E. A combined local and nonlocal closure model for the atmospheric boundary layer. Part II: Application and evaluation in a mesoscale meteorological model. **Journal of Applied Meteorology and Climatology**, v. 46, p. 1396-1409, sept. 2007a.

PLEIM, J. E. A combined local and nonlocal closure model for the atmospheric boundary layer. Part I: Model description and testing. **Journal of Applied Meteorology and Climatology**, v. 46, p. 1383-1395, sept. 2007b.

RAMOS, D. N. S.; LYRA, R. F. F.; SILVA JÚNIOR, R. S. Previsão do vento utilizando o modelo atmosférico WRF para o estado de Alagoas. **Revista Brasileira de Meteorologia**, v. 28, n.2, 2013.

ROGERS, D. P. Coastal meteorology. **Reviews of Geophysics**, v. 33, n. 2, p. 889-895, 1995.

ROSGAARD, M. H. **Limited area forecasting and statistical modeling for wind energy scheduling**. Thesis (Wind Energy PhD) - Technical University of Denmark, Denmark, 2015.

ROTUNNO, R. CURRY, J.A.; FAIRALL, C. W.; FRIEHE, C. A.; OVERLAND, J. E.; PIELKE, R. A.; ROGERS, D. P.; STAGE S. A. **Coastal meteorology**. A review of the state of the science. Washington: National Academy Press, 1992.

SAKAGAMI, Y.; SANTOS, P. A. HAAS, R.; PASSOS J. C.; TAVES, F.F. Effects of turbulence wind shear wind veer and atmospheric stability on power performance: a case study in Brazil. **Proceeding EWEA Conference**. Paris, 2015.

SANTOS, D. G.; LIRA, C. C. S.; LEAL JÚNIOR, J. B. V. Avaliação do potencial eólico da região do Vale do Jaguaribe no semiárido cearense utilizando modelagem numérica regional. **Journal of Environmental Analysis and Progress**, v. 3, n. 1, p. 69 – 74, jan. 2018.

SHEKHAWAT, A. S. Wind power forecasting using artificial neural networks. **International Journal of Engineering Research and Technology**, v. 3, issue 4, p. 993-998, apr. 2014.

SHIN, H. H.; HONG, S.-Y. Intercomparison of planetary boundary-layer parametrization sin the WRF model for a single day from CASES-99. **Boundary-Layer Meteorology**, v. 139, n. 2, p. 261-281, may 2011.

SHYU, A. S. **Aplicação de modelo híbrido de previsão de geração eólica nos parques eólicos de Pedra do Sal e Beberibe**. Dissertation (Undergradation in Mechanical Engineering) – Universidade Federal de Santa Catarina, Florianópolis, 2015.

SILE, T.; BEKERE, L; CEPITE-FRISFELDE, D.; SENNIKOV, J.; BETHERS, U. Verification of numerical weather prediction model results for energy application in Latvia. **Energy Procedia**, v. 59, p. 213-220, dec. 2014.

SILVA, A. F. G.; FISCH, G. Avaliação do modelo WRF para a previsão do perfil do vento no centro de lançamento de Alcântara. **Revista Brasileira de Meteorologia**, v. 29, n. 2, p. 259 – 270, jun. 2014.

SKAMAROCK, W. C.; KLEMP, J.B.; DUDHIA, J.; GIL, D.O., BARKER, D.M.; DUDA, M.G.; HUANG, X. Y.; WNAG, W.; POWERS, J. G. **A description of the Advanced Research WRF version 3**. NCAR Tech. Note, 2008.

SMITH, R. B. The influence of mountains on the atmosphere. **Advances in Geophysics**, v. 21, p. 87-230, 1979.

STENSRUD, D. J. **Parameterization schemes: keys to understanding numerical weather prediction models**. Oklahoma: Cambridge University Press, 2007.

STULL, R. B. **Meteorology for scientists and engineers**. 3rd ed. Vancouver: UBC, 2015.

STULL, R. B. **An introduction to boundary layer meteorology**. Dordrecht: Kluwer Academic Publishers, 1988.

SURUSSAVADEE, C. Evaluation of WRF near-surface wind simulations in Tropics employing different planetary boundary layer schemes. **The 8th International Renewable Energy Congress**, 2017.

TAKEYAMA, Y.; OHSAWA, T.; KOZAI, K.; HASAGER, C. B.; BADGER, M. Effectiveness of WRF wind direction for retrieving coastal sea surface wind from synthetic aperture radar. **Wind Energy**, v. 16, p. 865-878, 2013.

TAMPIERI, F. **Turbulence and dispersion in the planetary boundary layer**. Switzerland: Springer, 2017.

TAYLOR, B. J. **Methods and procedures for the verification and validation of Artificial Neural Networks**. New York: Springer Science & Business Media, 2006.

UCAR. **WRF model users' page**. 2016. Available in: <<http://www2.mmm.ucar.edu/wrf/users/>>. Accessed in: jul. 2016.

WALLACE, J; HOBBS, P. **Atmospheric science**. An introductory survey. 2nd ed. Amsterdam: Academic Press, 2006.

WANG, X.; GUO, P.; HUANG, X. A review of wind power forecasting models. **Energy Procedia**, v. 12, p. 770-778, 2011.

WARNER, T. **Numerical weather and climate prediction**. Cambridge: Cambridge University Press, 2011.

WEC. **World energy resources 2016**. 2016. Available in: <<https://www.worldenergy.org/wp-content/uploads/2016/10/World-Energy-Resources-Full-report-2016.10.03.pdf>>. Accessed in: mar. 2017.

WOBLEN. **E-44/900 kW**. Available in: <<http://www.woblen.com.br/produtos/importados/e-44-900-kw/>>. Accessed in: dec. 2017.

YADAV, N.; YADAV, A.; KUMAR, M. **An introduction to neural network methods for differential equations**. Warsaw: Springer, 2015.

YORKE, S. **Weather forecasting**. Made simple. Newbury: Countryside Books, 2010.

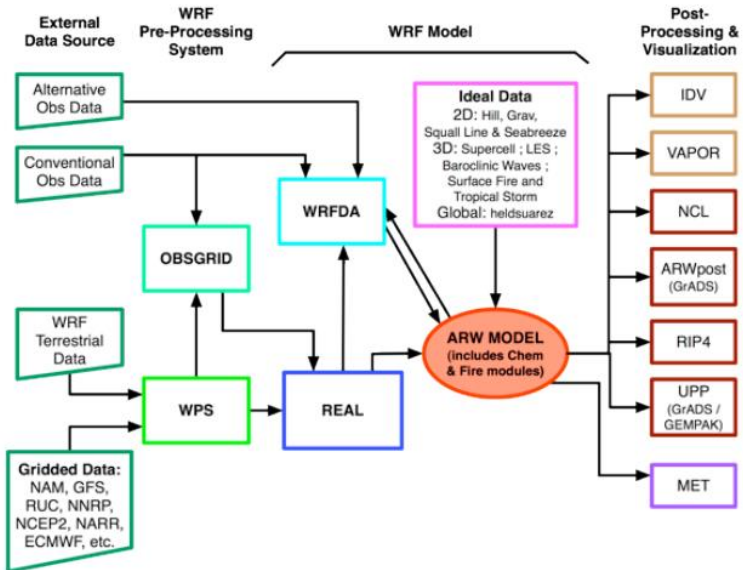
ZHAO, F.; HANG, T.; ZENG, Y.; XU, B. Towards a brain-inspired developmental neural network by adaptive synaptic pruning. **International Conference on Neural Information Processing**, p. 182-191. Springer, Cham, 2017.

ZHAO, Y.; YE, L.; LI, Z.; SONG, X.; LANG, Y.; SU, J. A novel bidirectional mechanism based on time series model for wind power forecasting. **Applied Energy**, v. 177, p.793-803, jun. 2016.

ZHAO, P.; WANG, J.; XIA, J.; DAI, Y.; SHENG, Y.; YUE, J. Performance evaluation and accuracy enhancement of a day-ahead wind power forecasting system in China. **Renewable Energy**, v. 43, p. 234-241, dec. 2012.

ANNEX A

Figure A.1 – WRF system flow chart.



Source: National Center for Atmospheric Research, 2016.

ANNEX B

Table B.1 – Technical specifications of the wind turbines in PSWF.

Company	WOBBEN Windpower
Model	Enercon E-44
Rated power	900 kW
Rotor diameter	44 m
Hub height	55 m
Wind class	IEC/EN IA
WEC concept	Gearless, variable speed, single blade adjustment
Rotor type	Upwind rotor with active pitch control system
Rotor rotation	Clockwise
Number of blades	3
Rotor wind speed	16 – 34.5 rpm
Cut-in wind speed	3 m/s
Cut-out wind speed	28 – 34 m/s

Source: Data from WOBBEN, 2017.